

Phenotypic landscape of intestinal organoid development

Inauguraldissertation

zur

Erlangung der Würde eines Doktors der Philosophie

vorgelegt der

Philosophisch-Naturwissenschaftlichen Fakultät

der Universität Basel

von

Ilya Lukonin

aus Deutschland

Basel, 2021

Originaldokument gespeichert auf dem Dokumentenserver der Universität Basel

edoc.unibas.ch

Genehmigt von der Philosophisch-Naturwissenschaftlichen Fakultät

auf Antrag von

Prof. Dr. Prisca Liberali

Fakultätsverantwortliche und Dissertationsleiterin

Prof. Dr. Matthias Lütolf

Korreferent

Basel, den 15.10.2019

Prof. Dr. Martin Spiess

Dekan

SUMMARY

Intestinal organoids are an ex vivo culture system of the intestinal epithelium that recapitulate many key aspects of the parent tissue: cell type diversity, spatial organization, but also the ability to regenerate and return to homeostatic conditions following damage. Intestinal organoids can develop from single cells, forming an emergent and self-organizing system undergoing temporally controlled cell fate transitions and spatial rearrangements. This complicated process is orchestrated by crosstalk of many pathways that together form a complex network of functional interactions. Although some components of this densely interconnected network have been resolved and described in detail, a systematic approach to mapping all of the involved players and their interdependence has not been attempted.

To address this complex question, I developed an image-based screen in intestinal organoids cultured from single cells using an annotated compound library. I designed a novel approach generating multivariate feature profiles for hundreds of thousands of individual organoids to quantitatively describe phenotypes observed in each of the screened conditions. These were used to identify stable phenotypic outcomes of intestinal organoid development in a data-driven manner. The relative abundance of each of the detected phenotypes produced a unique phenotypic fingerprint for every screened condition, quantitatively describing the phenotypic landscape of organoid development. I used the generated phenotypic fingerprints to find conditions with significant and reproducible effects, identifying 230 target genes. Subsequently, I used this multivariate dataset to infer the functional genetic interactions of identified genes generating the first map of interactions that govern intestinal organoid formation. This allowed me to discover modules of genes that regulate cell identity transitions and maintain the balance between regeneration and homeostasis. With network analysis I confirmed known players involved in key steps of organoid development but also revealed several novel potential upstream regulators.

In the second part of this study, I focused on conditions identified by the screen to enrich for a regenerative phenotype characterized by absence of differentiated cells of both absorptive and

secretory lineage. Abundance of this phenotype marked conditions that potentially improved the regeneration potential of the intestinal epithelium. Among these I discovered two key components of the retinoic acid signaling pathway: RXR and RAR. Follow-up studies allowed me to describe novel roles for nuclear retinoic acid receptors and retinol metabolism in intestinal damage response and homeostasis. By combining quantitative imaging with RNA sequencing I confirmed the role of endogenous retinoic acid signaling and metabolism for initiating transcriptional programs that guide intestinal epithelium cell fate transitions. I also observed that RXR inhibition not only suppressed differentiation, but induced a regenerative fetal-like transcriptional identity. To validate the physiological relevance of this finding, together with our collaborators we designed an *in vivo* study using a mouse model of cycling cell ablation to induce acute damage in the intestine, treating mice with the compound over the course of recovery. The mouse assay corroborated the findings from the organoid studies, showing that a small molecule inhibitor of RXR identified in the organoid screen improved intestinal regeneration *in vivo*.

Taken together, this study presents a novel approach for data-driven phenotypic discovery suitable for large image-based screens. This approach can be used on any other arrayed screen with single object resolution offering means to robustly identify phenotypic effects also in a complicated landscape characterized by pleiotropic phenotypes. Furthermore, it establishes a novel paradigm in genetic interaction screening applied to an emergent self-organized system that was ultimately instrumental to identify a small molecule that improved regeneration of the intestinal epithelium *in vivo*.

TABLE OF CONTENTS

SUMMARY.....	I
TABLE OF CONTENTS.....	III
LIST OF FIGURES.....	V
ABBREVIATIONS.....	VI
INTRODUCTION.....	1
1. Advent of the organoid systems.....	1
1.1 Historical perspective.....	1
1.2 Adult and pluripotent stem cell-derived organoids.....	2
1.3 Self-organization in organoids.....	5
2. Development and regeneration of the intestine.....	7
2.1 Embryonic and postnatal development.....	7
2.2 Adult intestinal tissue: homeostasis.....	8
2.3 Regeneration and cell type plasticity.....	8
2.4 Intestinal organoids as a paradigm for tissue regeneration.....	8
3. Signaling pathways governing intestinal organoid development and homeostasis.....	10
3.1 Wnt, Notch and Hippo.....	10
4. Functional genetic interactions.....	16
4.1 Inferring functional genetic interactions.....	16
4.2 Application of organoid systems for screening.....	17
5. Aim of this thesis.....	19

RESULTS.....	21
1. Using phenotypic fingerprints to study functional genetic interactions in the intestinal organoid system.....	21
DISCUSSION.....	24
1. Inferring the symmetry breaking event from the phenotypic space	27
2. Retinoic acid signaling.....	32
2.1 Nuclear retinoic acid receptors RXR and RAR	32
2.2 Metabolic control through RA availability.....	35
3. Loss of intestinal identity is linked to Cdx2.....	36
3.1 Cdx2 expression is necessary for establishing intestinal identity	37
3.1 Cdx2 expression depends on RA signaling activity.....	39
4. RXR α treatment improves intestinal regeneration <i>in vivo</i>	42
5. Concluding remarks	44
ACKNOWLEDGEMENTS.....	45
REFERENCES	47
APPENDIX.....	55

LIST OF FIGURES

Figure 1: generation of ASC- and PSC-derived organoids.....	2
Figure 2: generation of PSC-derived organoids recapitulates developmental steps	3
Figure 3: canonical Wnt signaling in intestinal stem cells	11
Figure 4: Notch signaling in cell type specification.....	12
Figure 5: Wnt-Notch-Hippo crosstalk in the intestinal epithelium.....	14
Figure 6: Model of organoid development and symmetry breaking.	15
Figure 7: From phenotypic screen to functional genetic interactions	25
Figure 8: Inferring the symmetry breaking event from the HIS interaction landscape	28
Figure 9: PAGA partitioning of the organoid phenotypic space	30
Figure 10: RXR antagonist treatment-induced transcriptional changes	34
Figure 11: Vitamin A is necessary for enterocyte differentiation	35
Figure 12: RXR antagonist treatment resembles Cdx2-null transcriptional signature	38
Figure 13: Cdx2 expression relies on RXR activity	39
Figure 14: RXRi treatment improves intestinal epithelium regeneration	43

ABBREVIATIONS

ALDH1A1	Aldehyde dehydrogenase 1 family member A1
Alpi	Alkaline phosphatase
ASC	Adult stem cell
atRA	all-trans retinoic acid
BMP	Bone morphogenic protein
Cdx1	Claudal type homeobox 1
Cdx2	Claudal type homeobox 2
CSL	CBF-1, Su(H), and Lag2
Dll1	Delta-like 1
DNA	Deoxyribonucleic acid
ECM	Extracellular matrix
EGF	Epidermal growth factor
EGFR	Epidermal growth factor receptor
ESC	Embryonic stem cell
Fz	Frizzled
HES1	Hairy and enhancer of split-1
HIS	Hierarchical interaction score
iPSC	Induced pluripotent stem cell
Isx	Intestine-specific homeobox
Jag	Jagged

Phenotypic landscape of intestinal organoid development
ABBREVIATIONS

Jak	Janus kinase
KO	Knockout
LATS	Large tumour suppressor kinase
LGR5	Leucine-rich repeat-containing G-protein coupled receptor 5
LRP	Lipoprotein receptor-related protein
MAML	Mastermind-like protein
MATH1	Helix-loop-helix protein mATH-1
MOB1	Mob1 homologue
MST	Mammalian ste20-like kinase
MTOR	Mechanistic target of Rapamycin
NICD	Notch intracellular domain
OLFM4	Olfactomedin 4
RA	Retinoic acid
RAR	Retinoic acid receptor
RARE	Retinoic acid response element
RNA	Ribonucleic acid
RNF43	Ring finger protein 43
RSPO	Rspondin 1
RXR	Retinoid X receptor
SAV1	Salvador family WW domain-containing protein 1
Shh	Sonic hedgehog

STAT	Signal transducer and activator of transcription
TCF	T-cell factor;
TEAD	TEA domain family member
TGF β	Transforming growth factor β
tSNE	t-distributed stochastic neighbor embedding
Wnt10A	Wingless and Int-1
Wnt3A	Wingless and Int-1
YAP1	Yes-associated protein 1
ZNRF3	Zinc and ring finger 3

INTRODUCTION

1. Advent of the organoid systems

Culturing tissues *in vitro* to understand their morphology and function has been a recurrent topic in biological research for over 100 years. As early as 1907, excised neurites were reported to be cultured for extended periods of time *ex vivo*, providing a platform for microscopic observations (Harrison et al., 1907). Over the course of the next century, the ground work for cell culture has been laid down with more and more sophisticated culture techniques evolving over decades, allowing studies of increasingly complex systems. Last decade has seen a boom of 3D organotypic systems, collectively termed organoids, developed to recapitulate a wide selection of tissues (Clevers, 2016) and used for diverse applications. Current definition of organoids stands for complex three-dimensional structures that recapitulate the architecture and function of *in vivo* organs and tissues, developed from stem cells or organ-specific progenitors through a self-organization process (Clevers, 2016; Fatehullah et al., 2016; Lancaster and Knoblich, 2014; Rossi et al., 2018).

1.1 Historical perspective

History of the organoid systems can be dated back to the 1970s, with introduction of first cultures of squamous epithelial colonies cultured from single cells. These colonies resembled human epidermis featuring keratinization in the upper layers and cell proliferation in the bottom layers (Rheinwald and Green, 1975). However, this system, cultured on a flat rigid surface and lacking the three-dimensional organization, was limited in its ability to mimic the parent tissue. Development of more physiologically relevant models required being able to recreate the three-dimensional environment that these tissues reside in. Due to this, further progress in organoid culture was only made possible with introduction of artificial ECM (Orkin et al., 1977) which enabled first three-dimensional *in vitro* cultures derived from mammary glands (Barcellos-Hoff

et al., 1989). Since then, a wide selection of tissues have been recapitulated *in vitro* with help of organoid systems, with the list ever growing. However, as diverse as they are, these systems share a single unifying feature: they originate from progenitor cells that develop *in vitro* giving rise to a complex structure with emergent properties.

1.2 Adult and pluripotent stem cell-derived organoids

Organoids can be divided into two categories depending on the cells used to generate them: iPSC- or ESC-derived, that can be colloquially referred to as PSC-derived, and ASC-derived (**Figure 1**). PSC-derived include thyroid (Kurmann et al., 2015), kidney (Takasato et al., 2014), optic cup (Eiraku et al., 2011), retinal (Shirai et al., 2016) and cerebral (Lancaster et al., 2013) organoids, whereas adult stem cell-derived include mammary (Olabi et al., 2018) and salivary gland, lung (Butler et al., 2016), pancreatic (Loomans et al., 2018), colon (Yui et al., 2012) and small intestinal (Sato et al., 2009) organoids.

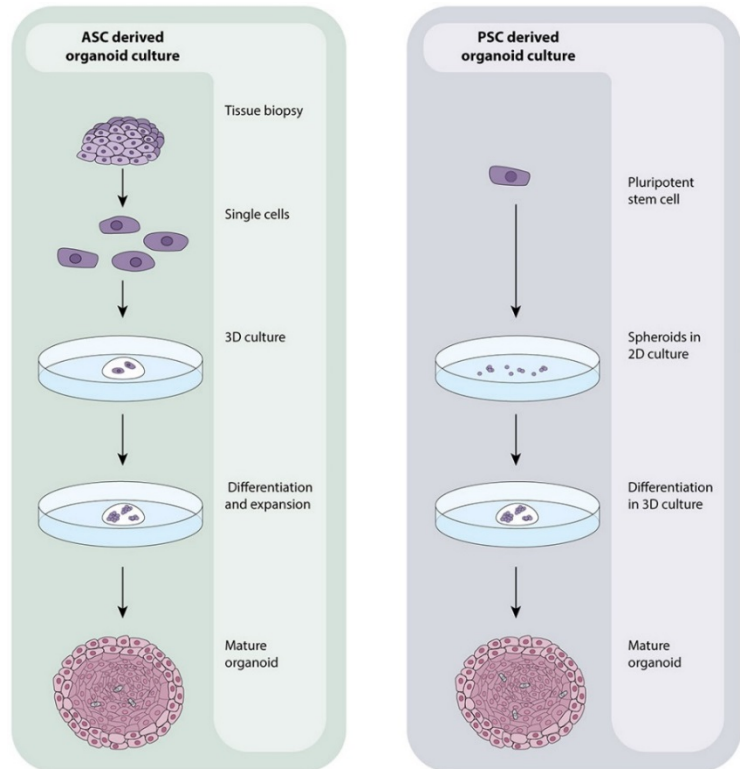


Figure 1: generation of ASC- and PSC-derived organoids

ASC-derived organoids are produced by dissociating biopsies of parent tissues and subsequent culture in artificial ECM. PSC-derived organoids are made from individual stem cells that first give rise to spheroids in suspension culture and are later transferred to 3D culture while treated with morphogens. Adapted from Iakobachvili and Peters (2017)

General strategy for development of PSC-derived organoids involves a regiment of morphogens, that, when used in a defined sequence, allow the patterning of a certain tissue type (**Figure 2**).

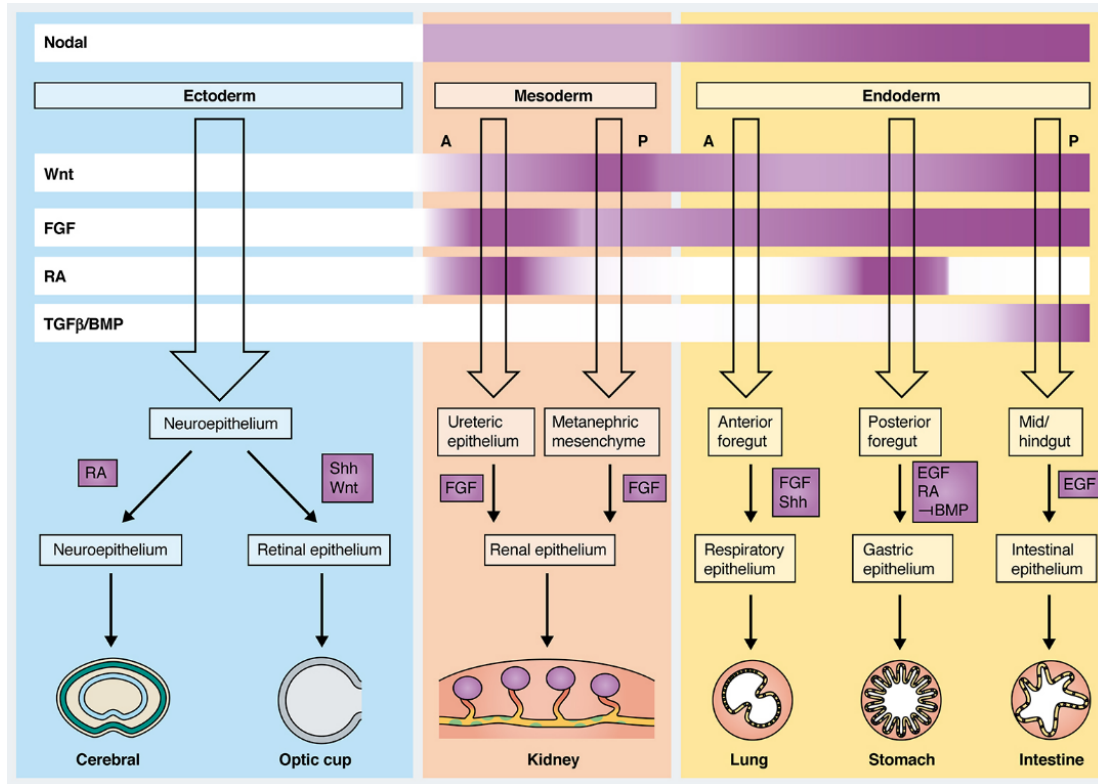


Figure 2: generation of PSC-derived organoids recapitulates developmental steps

Exposing PSCs to specific combinations and concentrations of morphogens, recapitulating the sequence of events during embryo development allows patterning of germ layer identity and subsequent formation of organoids mimicking a wide array of tissues. Adapted from McCauley and Wells (2017)

This regiment follows the sequence of events taking place during embryo development, starting from the germ layer specification. Establishment of the three germ layers results in separation of the mesoderm and endoderm from the ectoderm, this step occurs *in vivo* when during gastrulation epiblast cells migrate through the primitive streak (Ciruna and Rossant, 2001). Germ layer identity of PSCs largely depends on the Nodal and Wnt input that promote endoderm and mesoderm fate (Gadue et al., 2006). Absence of inductive signals at this step results in neural induction, during which, if cultured under morphogen-deprived conditions, PSCs will default to

neuroepithelial fate (Eiraku et al., 2008). Re-introducing tissue-specific inductive signals after the neuroepithelial program has been established can then be used to generate either cerebral (RA stimulation, (Lancaster et al., 2013)) or optic cup (Shh and Wnt stimulation, (Nakano et al., 2012)) organoids.

Similarly to the neuroepithelium, development of mesoderm- and endoderm-derived organoids can also be achieved using tissue-specific factors. Endoderm and mesoderm are patterned along the anterior-posterior axis by spatial and temporal gradients of Wnt, FGF, RA and TGF β /BMP (Kubo et al., 2004). Correctly timed activation of Wnt and then FGF results in anterior and posterior mesoderm and subsequent modulation of RA input allows patterning of ureteric epithelial and metanephric mesenchyme identities (Taguchi et al., 2014; Takasato et al., 2014). Subsequently, prolonged exposure of mesodermal lineages to Wnt and FGF can be used to generate kidney organoids (Taguchi et al., 2014).

The more posterior endoderm is patterned by Wnt and FGF signaling, that, when activated, promote the expression of posteriorizing transcription factor Cdx2 and commitment to mid/hindgut fate (Spence et al., 2011). Repression of Cdx2 expression achieved by inhibition of BMP signaling gives rise to foregut endoderm (Fausett et al., 2014; McCracken et al., 2014) that in turn is patterned along the anterior-posterior axis. Inhibition of BMP and RA signaling promotes anterior endoderm fate that can give rise to lung organoids (Dye et al., 2015), whereas stimulation with RA will result in posterior foregut fate that can be used to generate gastric organoids (McCracken et al., 2014). The most posterior endodermal identity is achieved through BMP stimulation, and will give rise to intestinal organoids (Spence et al., 2011). Taken together, this shows how recapitulation of key steps in embryo development drives the directed differentiation of PSCs and allows generation of complex organoid systems. Although PSC-derived organoids hold great potential and can be used to generate a wide array of tissues and allow doing so in a patient-specific context, the resulting organoids more closely resemble embryonic rather than adult tissues (Eiraku et al., 2011; McCracken et al., 2014; Rossi et al., 2018).

In contrast, ASC-derived organoids do not recapitulate developmental steps, rather, this system utilizes the regenerative capacity of parent tissues. Consistently, growth conditions for ASC-derived organoids typically include factors controlling tissue repair or homeostasis and resulting structures are more reminiscent of the adult tissues (Clevers, 2016).

To-date the view of ASC-derived organoids as recapitulating tissue regeneration is not yet dominant, however several recent findings speak in favor of this concept. Firstly, many ASC-derived organoid systems mimic tissues that either have high cell turnover rate or that are capable of regeneration, such as the small intestine, stomach and lung. Furthermore, recent studies show that both in the liver and in the lung, regenerative response following acute damage involves induction of cells capable of generating organoids. In the liver acute damage induces cells expressing the stem cell marker *Lgr5* (Huch et al., 2013) that have the capacity not only to regenerate hepatocytes and bile ducts but also to give rise to hepatic organoids. Similarly, in the lung, a tissue characterized by very low proliferation under normal conditions, acute damage leads to an increase in number of cycling cells (Pardo-Saganta et al., 2015) that can give rise to organoids in culture (Tadokoro et al., 2014).

Although different in their origin, both PSC- and ASC-derived organoids are emergent structures, in which the complexity of the resulting system cannot be explained by the sum of its parts. Formation of organoids is driven by the intrinsic capacity of stem cells to self-organize into 3D structures that mimic many aspects of the parent tissue, making the common feature of self-organization a defining aspect of the organoid systems.

1.3 Self-organization in organoids

In the context of organoids, self-organization can be defined as the spatial rearrangement of an initially homogenous group of cells exposed to a uniform signaling environment that results in formation of an asymmetric higher ordered structure in a system-autonomous manner. There is ongoing debate, whether organoids undergo true self organization or if they rather demonstrate genetically-encoded self-assembly, a phenomenon described as emergence of localized signaling

sources that, when stabilized, act as references for patterning (Turner et al., 2016). Many organoid systems in fact require stimulation with exogenous growth factors to trigger the process of organoid formation, as these are not present in the initial cells used to generate organoids.

For instance, in intestinal organoids growth the exogenous stimulation with Wnt ligands is required in the initial steps, subsequently triggering a downstream cascade of self-organizing events such as cell type emergence and spatial reorganization that later proceed also after Wnt stimulation is withdrawn. Although in the strict definition of the term, intestinal organoids thus differ from canonic self-organized structures defined in physics or chemistry, such as dissipative structure formation or self-sustained oscillations, in the context of this thesis I refer to development of intestinal organoids from single cells as a self-organized behavior. This is due to two key observations: firstly, intestinal organoids undergo symmetry breaking without external differentiation cues, hinting that the order in this system is, in fact, emergent (Serra et al., 2019). Secondly, once the developing intestinal organoids have reached an asymmetric state, they undergo self-patterning and self-sorting ultimately achieving equilibrium at homeostatic conditions. It must be noted that this equilibrium state is largely dependent on boundary conditions, e.g. when cultured for prolonged periods of time, intestinal organoids give rise to large and highly branched structures that seem to increase in cell mass near-indefinitely. Recent studies however show that restricting boundary conditions by culturing intestinal epithelium on spatially restricted surfaces (Wang et al., 2017) will finally result in stable structures that maintain a finite cell number through turnover.

2. Development and regeneration of the intestine

To provide context on how the intestinal tissue is formed and patterned and how it reaches, maintains and restores the homeostatic state, in this section I discuss key steps in the development and regeneration of the murine intestinal epithelium.

2.1 Embryonic and postnatal development

The transition from endoderm to an intestinal-type epithelium described above relies on temporally and spatially controlled expression of *Cdx2* that is first expressed in all three germ layers and then gets restricted to the intestinal epithelium by the time of midgestation (Beck et al., 1995). This molecular patterning precedes the changes at the cellular and tissue level: progressing from the proximal to the distal intestine, stratified endodermal epithelium transforms into a simple columnar epithelium with the formation of nascent villi accompanied by differentiation. This process sees emergence of absorptive enterocytes, goblet and enteroendocrine cells.

Emerging villi are separated by stretches of intervillus epithelium that will give rise to the crypt compartment during postnatal development (Gordon and Hermiston, 1994). Intestinal crypts that emerge from intervillus epithelium host the stem cell niche which provides the environment supporting self-renewal and preventing differentiation. Formation and maintenance of the stem cell niche depends on the Paneth cells that unlike the other intestinal epithelial cell types emerge concomitantly with crypts after the villi have already been formed (Kim et al., 2012). Emergence of crypts hence marks the establishment of the mature epithelium phenotype that will robustly maintain homeostasis throughout life.

2.2 Adult intestinal tissue: homeostasis

The homeostatic state of intestinal epithelium is characterized by an uninterrupted directional movement of cells along the crypt-villus axis accompanied by cell fate transitions (Bjerknes and Cheng, 1999). Intestinal cells are born as progeny of perpetually self-renewing Lgr5⁺ stem cells at the bottom of the crypt (Snippert et al., 2010). Subsequently Lgr5⁺ daughter cells exit the crypt base to enter the transit amplifying (TA) zone, where they divide rapidly before continuing their movement towards the villus (Marshman et al., 2002). As cells exit from the stem and TA zone, they give rise to all post-mitotic cell types required to fulfill the physiological functions of the intestine. Cells that reach the villus tip undergo apoptosis and are shed into the intestinal lumen (Bullen et al., 2006) thus maintaining the homeostatic cell turnover.

2.3 Regeneration and cell type plasticity

Intestinal epithelium fulfils two functions most crucial to the survival: nutrient absorption and providing a barrier between the organism and the content of the intestinal lumen. To be able to robustly carry out these functions, the intestinal epithelium has a remarkable ability to regenerate in response to a variety of challenges and subsequently return to homeostasis.

This regenerative response can be triggered by acute damage and is mediated by the broad plasticity of intestinal epithelial cells allowing them to dedifferentiate and replenish the pool of cycling cells. Cell types shown to undergo such dedifferentiation include Dll1⁺ secretory progenitors (van Es et al., 2012), label-retaining cells (Buczacki et al., 2013), Alpi expressing enterocyte precursors (Tetteh et al., 2016), enteroendocrine (Jadhav et al., 2017) and, more recently, Paneth cells (Schmitt et al., 2018).

2.4 Intestinal organoids as a paradigm for tissue regeneration

An ASC-derived intestinal organoid can develop from a single cell forming an emergent, self-organized structure undergoing spatially and temporally controlled cell fate transitions (Sato et

al., 2009; Serra et al., 2019). Recent findings highlight that the original cells do not necessarily have to be the Lgr5⁺ stem cells of the intestinal crypt, illustrating how organoid formation relies on the plasticity of intestinal epithelial cells (Serra et al., 2019).

In the first step of organoid development, single cells undergo several rounds of division maintaining nuclear localization of YAP1 that has been shown to depend on the mechanical properties of the surrounding matrix. Stiff matrix promotes YAP1 nuclear translocation whereas matrix softening at this initial early step results in YAP1 cytoplasmic translocation and is detrimental to organoid growth (Gjorevski et al., 2016). If the extracellular matrix requirement is fulfilled, single cells will form a symmetric cyst-like structure with all cells composing the cyst characterized by nuclear localization of YAP1 and lacking expression of genes characteristic for intestine-specific lineages (Serra et al., 2019). In fact, also the stem cell marker Lgr5 is lost during the first days of organoid development and only reacquired after the stem cell niche is established in the emergent organoids (Serra et al., 2019). Loss of Lgr5 expression suggests that early organoids consist of cells undergoing a regenerative response, distinct in their identity from the stem cells of the adult intestine (Gregorieff et al., 2015). Subsequently this symmetry is broken, resulting in the formation of secretory Paneth cells that become the local source of Wnt ligands. Whereas *in vivo* the Wnt secreting function of Paneth cells can be taken over by the mesenchyme (Farin et al., 2012), Paneth cells are an indispensable Wnt source for maintaining the stem cell niche in organoids (Sato et al., 2011). Nascent Paneth cells nucleate the crypt-like compartment in the intestinal organoids by forming local Wnt-rich environments that support Lgr5⁺ stem cell maintenance. Once the crypt region is established, cells distal from the crypt begin to differentiate to absorptive enterocytes that make up the villi of the intestinal epithelium (Sato et al., 2009) re-establishing the division-driven cell flux.

Thus, development of intestinal organoids from a single cell recapitulates the regeneration of the intestinal epithelium and the re-establishment of homeostasis (Chacon-Martinez et al., 2018; Qi et al., 2017). This complex process involves numerous players and is orchestrated by crosstalk and coordinated action of several signaling pathways.

3. Signaling pathways governing intestinal organoid development and homeostasis

As discussed above, formation of intestinal organoids is a highly complex process underlying regulation by multiple signaling pathways. In this section I discuss the main contributing factors described in the system to-date and the crosstalk between signaling cascades that is crucial for orchestrating organoid formation and homeostasis.

3.1 Wnt, Notch and Hippo

The perhaps best described pathway in the context of intestinal epithelium is the canonical Wnt signaling. In fact, the bona fide marker of intestinal stem cells, *Lgr5*, is an important component of the canonical Wnt signaling (**Figure 3**). In the intestinal crypt, Wnt input maintains the self-renewal capacity of ISCs by driving expression of genes involved in positive regulation of cell cycle and suppressing differentiation (Korinek et al., 1998). As Paneth cells are the only source of Wnt in the intestinal organoid system, their position at the bottom of the crypt and the limited diffusion of the membrane-tethered Wnt ligands mediated by cell division explains how the gradient of Wnt is restricted spatially (Farin et al., 2016). Consistently, deletion of β -catenin as well as overexpression of *Dkk1*, a diffusible Wnt inhibitor, results in loss of intestinal crypts (Kuhnert et al., 2004; Pinto et al., 2003). Furthermore, modulation of Wnt by RSPO allows cell-type-specific potentiation of Wnt signaling (Kim et al., 2005), whereby cell type specificity is achieved through binding of RSPO to the *Lgr5* on the surface of intestinal stem cells (**Figure 3**). RSPO stimulation results in potentiation of the Wnt signaling activity (Ruffner et al., 2012), directly influencing the extent of the Wnt gradient (Farin et al., 2016) and abundance of stem and Paneth cells. Thus, Wnt signal range and amplitude control the size of the stem cell niche and dictate the morphology of the intestinal crypts (Farin et al., 2012).

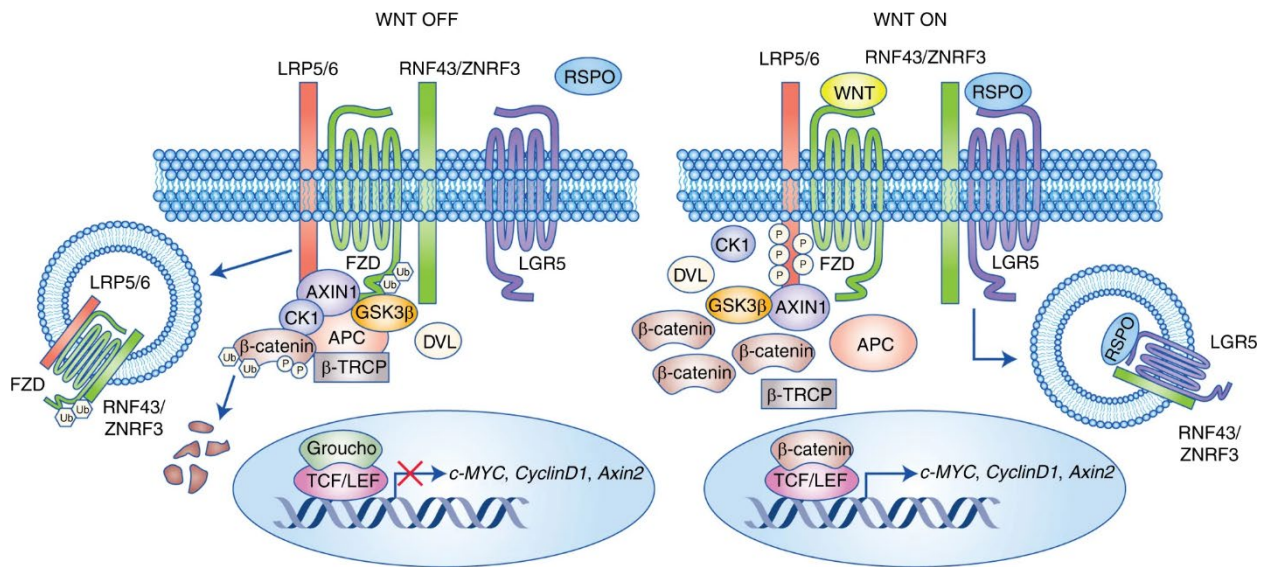


Figure 3: canonical Wnt signaling in intestinal stem cells

Lgr5 acts as a promotor of Wnt/ β -catenin signaling through regulation of transmembrane E3 ligases RNF43/ZNRF3. In ligand (RSPO)-unbound state, LGR5 is inactive and Wnt signaling is suppressed by RNF43/ZNRF3, which internalize and degrade the Wnt receptors Frizzled and LRP5/6 resulting in β -catenin degradation and repression of Wnt target genes. Binding of RSPO to LGR5 sustains Wnt signaling by cell membrane clearance of the RNF43/ZNF3 ligases, leading to unhindered activation of Wnt signaling and stabilized β -catenin and downstream activation of Wnt targets. Adapted from Morgan et al. (2018)

However, Wnt signaling at the same time also promotes Paneth cell differentiation through induction of transcription factors such as SOX9 and Math1 (Bastide et al., 2007). To explain these functionally diverse responses to a single stimulus, one needs to consider that Wnt signaling acts in concert with other signaling pathways.

One of its major interacting pathways is Notch, a highly conserved juxtacrine signaling network (**Figure 4**) in which signaling is initiated by contact-based ligand binding events at the cell surface of two or more adjacent cells (Baron, 2003). Mammalian Notch family comprises four transmembrane Notch receptors (Notch1–4) and five transmembrane ligands (Jag1 and 2 and Dll1, 3 and 4). Binding of a Notch ligand to its cognate receptor initiates several proteolytic steps resulting in γ -secretase-mediated cleavage and intracellular release of the NICD (Schroeter et al., 1998). NICD then translocates to the nucleus and binds the transcription factor CSL, that in

absence of ligand represses target gene expression (Krejci and Bray, 2007). NICD binding thus results in transcriptional activation and drives expression of Notch target genes (**Figure 4**).

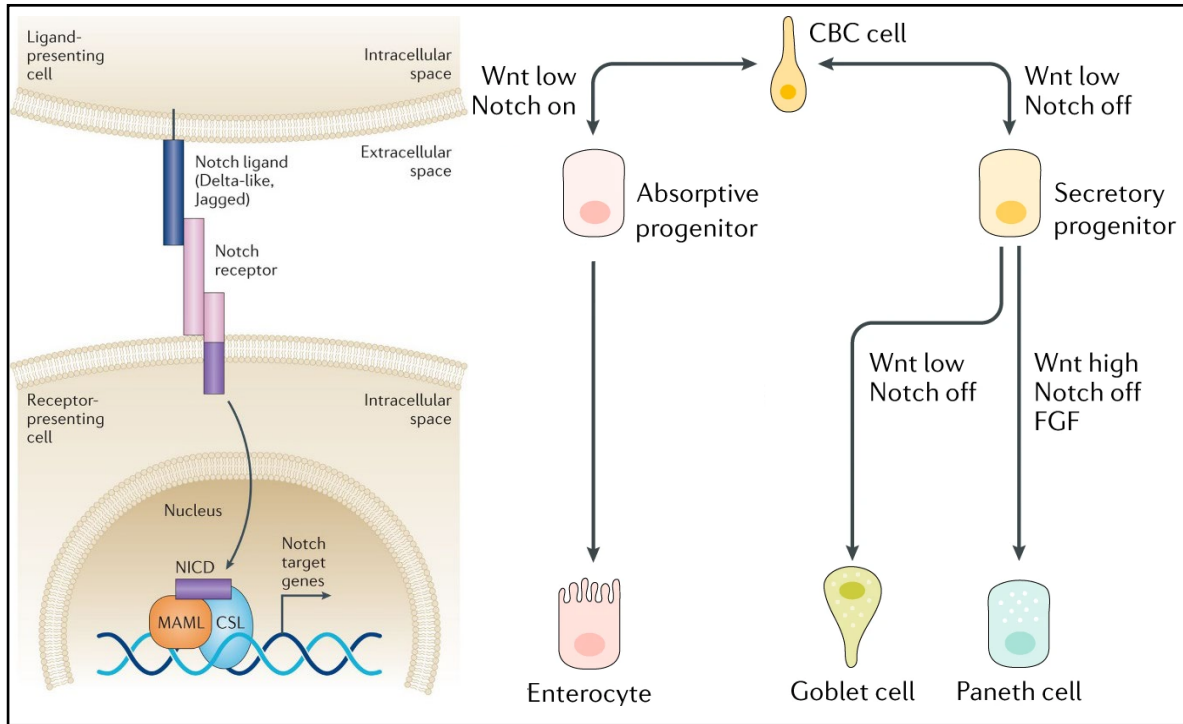


Figure 4: Notch signaling in cell type specification

Notch signaling pathway relies on a mechanism in which ligand on the surface of the sending cell induces a series of proteolytic cleavage events in a Notch receptor on a contacting receiving cell releasing the Notch intracellular domain (NICD), which translocates to the nucleus to activate the transcription of Notch target genes together with cofactors (CSL and MAML) (left), adapted from Andersson and Lendahl (2014). Interplay of Wnt and Notch inputs defines the fate of secretory and absorptive progenitors and resulting cell lineages (right). Modified from Gehart and Clevers (2019)

In the context of intestinal epithelium, Notch pathway is an important factor regulating the fate of stem cell progeny: Notch target gene *Hes1* antagonizes the transcription factor *Math1* (Suzuki et al., 2005), a Wnt target gene promoting secretory cell fate (van Es et al., 2005). This shows how Notch signaling can modulate response to Wnt signaling, playing a deciding role in secretory lineage commitment (**Figure 4**).

Furthermore, owing to its juxtacrine signaling mechanism, Notch is associated with generation of alternating cellular patterns that define the spatial organization of intestinal cell types. Notch inhibition leads to increased secretory cell differentiation whereas intestine-specific NICD overexpression blocks commitment to secretory lineage (Fre et al., 2005). In the intestinal crypt, ISCs are characterized by high Notch receptor expression (Fre et al., 2005), whereas neighboring Paneth cells present the Notch ligands Dll1 and Dll4 on their surface (Serra et al., 2019; Shimizu et al., 2014), maintaining Notch activity in stem cells while simultaneously suppressing ligand expression. This lateral inhibition allows maintenance of the stem cell pool by providing the combined signaling input required for maintenance and activity of the ISCs. The interplay between Wnt and Notch (**Figure 4**) is thus crucial for maintaining the ratios of progenitors and differentiated cell types in homeostasis.

However, Notch also plays an important role in the symmetry breaking event during early organoid development: as the organoid develop from single cells, they undergo several rounds of synchronous cell division until at 16 to 32 cell stage this symmetry is broken and initial Paneth cells begin to appear. At the molecular level, Dll1⁺ ligand-presenting cells promote Notch activity in neighboring cells and due to the negative feedback loop suppress expression of membrane-bound Notch ligands, thus establishing the pattern described above (Serra et al., 2019).

Although Wnt-Notch crosstalk is sufficient to explain how the ratio between secretory and absorptive progenitors is maintained during the homeostatic self-renewal of the intestine, it does not fully explain the emergence of cell types during intestinal organoid development from single cells. In this context, there is another important factor upstream of Notch: Yap, an effector of the Hippo pathway that responds to a plethora of extrinsic inputs.

Hippo pathway in mammalian cells relies on MST1- and MST2-mediated activation of LATS kinases (Chan et al., 2005) which in turn can phosphorylate YAP1 resulting in its cytoplasmic retention (Meng et al., 2016). Thus, in Hippo-ON state the Yap transcriptional targets remain suppressed whereas deactivation of Hippo results in dephosphorylated YAP1 nuclear translocation (**Figure 5**), binding to TEAD transcription factors and expression of target genes (Li

et al., 2010). Interestingly, the activity of the Hippo pathway does not rely on dedicated receptors and ligands but is rather regulated by a network of upstream components involved in cell adhesion (Kim and Gumbiner, 2015), morphology (Dupont, 2016) and polarity (Chen et al., 2010), enabling Hippo to act as a sensor for tissue integrity and cellular stresses.

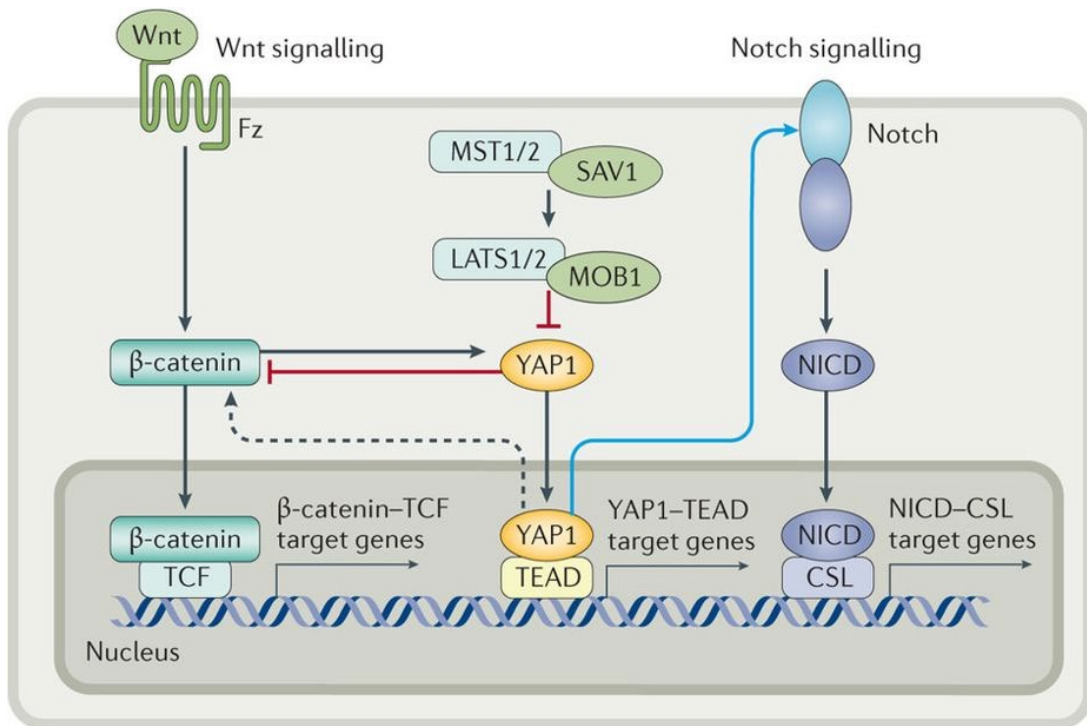


Figure 5: Wnt-Notch-Hippo crosstalk in the intestinal epithelium

Activation of the Hippo pathway results in cytosolic retention of YAP1 which sequesters β -catenin. Inactivation of the Hippo pathway drives nuclear translocation of YAP1 that upregulates Wnt and Notch signaling, resulting in upregulated expression of Notch receptors and subsequent translocation of the NICD to the nucleus. Black arrows indicate direct activation, blue arrows indicate transcriptional regulation, dotted lines indicate processes supported by experimental evidence but without a known mechanism (top), adapted from Hong et al. (2016).

Due to its mechanosensing properties, Yap has a crucial function in initiating damage response in the intestine: dynamic regulation of YAP1 subcellular localization allows cells to upregulate target genes involved in regeneration as a response to damage (Cai et al., 2010). Yap activation results in expansion of the pool of undifferentiated progenitors in the intestinal epithelium

(Camargo et al., 2007). Similarly, in the intestinal organoid system nuclear Yap activity is necessary for initiating the first steps of organoid development: during this early phase of exponential growth, cells composing the early organoid have high nuclear YAP1 levels, making YAP1 nuclear activity a hallmark of the regenerative state.

However, the function of Yap seems to be much more versatile than just promoting self-renewal and extends to shaping cell fate identities. Emergent asymmetry in YAP1 levels leads to symmetry breaking by establishing variance in Notch ligand expression (**Figure 6**). Dll1, a reported Yap target gene (Slemmons et al., 2017), is higher expressed in cells with high levels of nuclear YAP1 and asymmetry in YAP1 nuclear translocation precedes Notch lateral inhibition establishment (Serra et al., 2019). As discussed above, Notch-mediated patterning has been shown to be a prerequisite for differentiation of initial Paneth cells. Consistently, preventing the cell-to-cell asymmetry in YAP1 subcellular localization results in loss of Paneth cells via a Notch-dependent mechanism and resulting organoids fail to establish a crypt compartment (**Figure 6**).

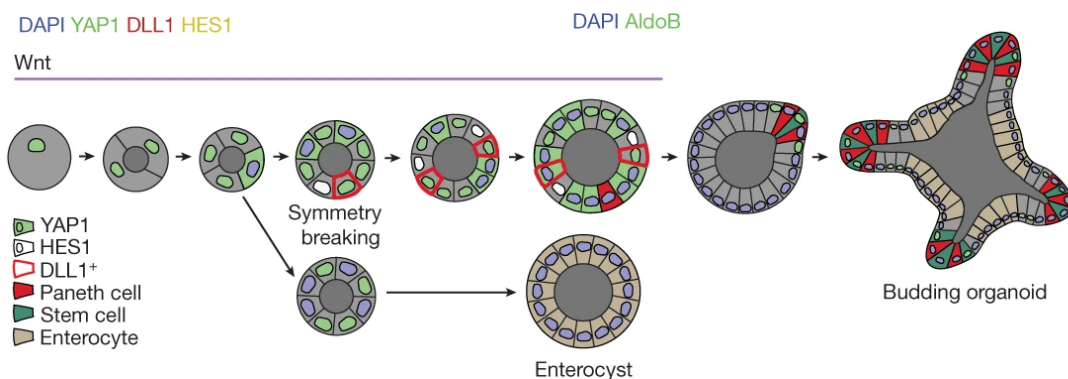


Figure 6: Model of organoid development and symmetry breaking.

Schematic of the organoid development from a single cell and accompanying emergence of differentiated cells of secretory and absorptive lineage, adapted from Serra et al. (2019).

While the pathways discussed above explain some of the fundamental factors in establishing and maintaining the homeostasis in the intestinal epithelium tissue, there are many others that contribute to this process. *In vivo*, one important factor for patterning of the intestinal tissue is

BMP signaling, with BMP ligands forming a gradient in opposite direction to Wnt, going from the villus tip to the crypt bottom (He et al., 2004). Interestingly, the intestinal organoid system is insulated from BMP receptor stimulation due to the presence of Noggin that sequesters BMP ligands, however it still robustly achieves patterning of crypt and villus-like domains also in absence of BMP input.

There are many more signaling pathways reported to influence intestinal regeneration and homeostasis, such as EGFR (Alferez et al., 2008), PI3K (He et al., 2007), Jak/STAT (Gilbert et al., 2015) and others, together forming a densely interconnected network (Spit et al., 2018). Such complex relationships cannot be explained by the action of individual pathways, but rather require an understanding of the functional interactions between all of the involved players.

4. Functional genetic interactions

An observation that mutation of two genes can result in a phenotype distinct from that produced by mutations of the individual genes gave rise to the concept of genetic interactions. Genetic interactions thus describe the interdependence between genes, showing how function of one gene depends on the presence of a second gene, allowing identification of functional modules and pathways (Costanzo et al., 2016). Such information can be inferred from large scale experiments and used to describe regulatory pathways and identify functions of genes (Costanzo et al., 2016; Shen et al., 2017).

4.1 Inferring functional genetic interactions

One classical approach to map genetic interactions are double gene knockout screens in which gene knockout effect is measured over a number of epistatic backgrounds with the goal of revealing whether the two genes co-function in the same pathway (Costanzo et al., 2016; Tong et al., 2004). Historically performed in yeast, such screens have been recently extended to other organisms, such as *E. coli* and even mammalian cell lines (Shen et al., 2017). These studies allow

de-novo mapping of vast numbers of functional interaction but typically rely on a single readout, colony fitness, both in arrayed (yeast) and pooled (CRISPR-Cas9 edited mammalian cells) screens. Owing to their readout, such screens lack in sensitivity for pathways non-crucial to cell viability and do not provide phenotypic resolution. An alternative approach are arrayed screens that allow image-based phenotyping of cell populations in which specific genes are perturbed (Liberali et al., 2014). Due to exponential rise in combinations for epistatic backgrounds making double gene perturbations impractical, in arrayed image-based screens the information content is instead gained by performing multiple arrayed single-gene perturbations in parallel with multivariate readouts describing every condition (Liberali et al., 2014, 2015; Snijder et al., 2013).

Data obtained from genetic interaction screens can then be used to cluster genes by the similarity of interaction profiles revealing hierarchical relationships. Due to the nature of regulatory interactions, perturbing an upstream effector of a pathway, for instance a kinase that phosphorylates multiple substrates, might result in a measured effect on a broad set of readouts, whereas perturbing a downstream actor would only affect a subset of those. As a consequence, correlation-based measurements would show low similarity for the two perturbations. Methods developed to account for such nested effects include the hierarchical interaction score (HIS), a statistical method capable of identifying hierarchical relationships for pairs of conditions based on effect strength and presence in multivariate readouts (Liberali et al., 2014; Snijder et al., 2013).

4.2 Application of organoid systems for screening

Advances in the ex vivo cell culture field allow recapitulation of increasingly complex tissues through organoid models that display phenotypes not observable in 2D culture systems. The 3D organization of organoids and their ability to mimic tissue context enables studies of tissue-specific gene functions and their impact on cellular communities. This advantage of organoid models has been recently applied to biobank and analyze patient-derived breast cancer organoids that were subsequently used to screen patient-dependent differences in

chemotherapy drug responses (Sachs et al., 2018). Furthermore, organoids can be used for phenotypic profiling of gene knockout effects, allowing mapping of tissue-specific regulatory networks (Gao et al., 2015). These examples illustrate the importance of phenotypic resolution offered by organoid systems in their high content screening application. Although technically challenging, this approach is greatly rewarding for addressing complex biological questions such as mapping functional genetic interactions.

5. Aim of this thesis

As outlined above, formation of intestinal organoids from single cells relies on the regenerative capacity of the intestinal epithelium and recapitulates damage response and return to homeostasis. Orchestrated by a plethora of pathways, this complex process shows astonishing robustness: single cells, when placed into growth-promoting culture conditions, reproducibly initiate cyst-like structures that then develop into highly complex branched organoids. However, which pathways contribute to this process and how they are interconnected is not yet well understood, leading to the main questions I address in this thesis, firstly:

- **Which functional interactions determine the phenotypic outcome of organoid self-organization?**

To answer this question, I use phenotypic image-based screening as a tool providing information not only on fitness of cells to initiate organoid formation in a given perturbation, but also delivering phenotypic resolution. For the phenotypic discovery at end time point I evaluated the size and shape of the organoids, but also extracted information on their cell type composition. From previous studies it was known that after four days in culture organoids contain both secretory Paneth cells and absorptive enterocytes. These two cell fates are mutually exclusive and their spatial segregation along the crypt-villus axis can be used to describe the organoid spatial organization, therefore I used antibody staining for markers of these cell types as robust cell fate readouts.

In order to perturb a high number of pathways in an arrayed assay I chose chemical genetics approach using an annotated compound library of almost 3000 well-described compounds. Although intuitive in essence, the phenotypic screen of this scale in a complex three-dimensional model is challenging to facilitate. Specific technical questions that I aim to address with my PhD project are thus:

- How to ensure robust and reproducible results for an organoid-based phenotypic screening assay?

- How to describe the emergent complex phenotypic landscape in a quantitative way?
- How to factor phenotypic heterogeneity for the analysis of the screen results?

Beside the technical considerations however, I wanted to show the biological relevance of mapped functional interactions, leading to the second broader question:

- **What are the biological insights that can be gained from the identified interactions?**

RESULTS

1. Using phenotypic fingerprints to study functional genetic interactions in the intestinal organoid system

Regenerative landscape of intestinal organoids

Ilya Lukonin, Denise Serra, Katrin Volkmann, Janine Baaten, Rui Zhao, Shelly Meeusen, Francisca Maurer, Michael B. Stadler, Jeremy Jenkins, Prisca Liberali

Nature, in revision

The entire unpublished manuscript can be found in the Appendix 1.

Summary

Intestinal epithelium is a tissue characterized not only by high cell turnover but also an unmatched capability to regenerate that is mediated by plasticity of intestinal cell types. As an *ex vivo* culture of the intestinal epithelium, intestinal organoids mimic the homeostatic state of their *in vivo* counterpart in both cell type composition and spatial organization. However, development of intestinal organoids from single cells also recapitulates the remarkable regenerative capacity of intestinal epithelium that enables this tissue to regenerate and return to homeostatic conditions following damage. When intestinal organoids develop from a single cell, they give rise to an emergent, self-organized structure undergoing spatially and temporally controlled cell fate transitions orchestrated by coordinated and interdependent signaling events. Although function of several key players in this process has been explored, it is was not clear which other pathways potentially contribute to this emergent order and how they are interconnected.

To unravel molecular mechanisms orchestrating organoid formation and regeneration of intestinal tissue, I developed a high-content image-based screening assay culturing organoids

from single cells in thousands of arrayed conditions. With quantitative imaging, I generated multivariate feature profiles for hundreds of thousands of individual organoids to quantitatively describe the phenotypic landscape of organoid development. My analysis revealed 15 stable phenotypic outcomes that were used to generate unique phenotypic fingerprints describing every condition. The resulting phenotypic fingerprints were then used to identify and describe 230 genes that reproducibly alter organoid phenotypes and to infer regulatory genetic interactions between these genes. This analysis yielded the first large-scale map of functional interactions governing intestinal organoid formation.

From the results of the screen I identified conditions showing an enrichment in a regenerative phenotype characterized by absence of both absorptive and secretory lineage. The highest penetrance of this phenotype was observed in conditions perturbing RXR and RAR, the core machinery of the retinoic acid signaling pathway. In the follow up studies I describe novel roles for nuclear retinoic acid receptors in intestinal regeneration and show how RA signaling is controlled through retinol metabolism in homeostasis. I went on to investigate the effect of retinoic acid signaling modulation on the transcriptional identity of intestinal cells, showing not only suppressed differentiation, but an induction of a regenerative fetal-like transcriptional profile. To understand whether this would translate into improved regeneration of the intestine, together with our collaborators we performed an *in vivo* study using a mouse model of cycling cell ablation to induce acute damage in the intestine. Treating mice with the compound over the course of recovery resulted in improved regeneration of functional intestinal tissue, manifesting in reduced body weight loss, recovery of the barrier function and regeneration of villi. Thus, our *in vivo* study confirmed the effect of RXR antagonist treatment observed in the organoid system, suggesting RXR antagonists as potential therapeutic agents for improving intestinal regeneration after acute damage.

Taken together, this work shows how genetic interactions can be inferred from a single image-based screen in an emergent system and used to detect and describe novel functions for a signaling pathway ultimately delivering a candidate drug for improving tissue regeneration *in vivo*.

My contribution

As this study constitutes my main project during the PhD, most experiments were planned, performed and analyzed by me. Furthermore, it includes the results of a fruitful collaboration with the group of Rui Zhao from the Genomics Institute of the Novartis Research Foundation who conducted a mouse study using irradiation-induced colitis model corroborating the results obtained from the work in intestinal organoids.

DISCUSSION

As exemplified in the Introduction, culturing intestinal organoids from single cells allows screening for pathways that impact both the regenerative capacity and cell type balance in the intestinal epithelium. These changes are best described by multivariate phenotypes, which can only be accurately profiled in an image-based arrayed screen. This question was however hard to address, in part due to lack of a reliable assay with a quantitative approach that would allow sufficient throughput to screen a high coverage library.

I faced two major challenges in the assay development: firstly, there was no state-of-the-art approach to intestinal organoid culture automation. To address this, I developed a heavily automated cell culture protocol for generation of ECM-embedded organoids. For this, single cells isolated from organoid pre-cultures were added to well plates containing pre-plated Matrigel and brought into the matrix phase by centrifugation. This proved to be instrumental in miniaturizing the assay to 384 well plate format, thus making the screen at the desired scale possible. Liquid handling automation was used in every step of the organoid culture from plating and treating organoid cultures to fixing and performing immunofluorescence staining, greatly improving reproducibility and decreasing handling time.

Second major challenge was related to high-magnification imaging of intestinal organoids at the end time point of the screen. Intestinal organoids represent a sparse sample in terms of imaging with objects occupying less than 50% of the well area accessible to imaging (**Figure 7a**). Working together with the microscope vendor, we developed the software tools for an iterative imaging workflow: each well of the multiwall plates was first acquired with 2x magnification, processed and segmented on the fly to extract coordinates of individual organoids. Wells were then subdivided into a grid mosaic, corresponding to adjacent placement of 40x magnification fields of view. Subsequently every non-empty field was acquired at high resolution, producing multichannel confocal z-stacks (**Figure 7a**, also see **Appendix 1**). This imaging approach allowed to decrease the acquisition time and the generated data volume more than two-fold, which was necessary for making imaging at the desired resolution technically feasible. Furthermore, the grid

pattern approach allowed to avoid imaging redundancy as compared to previously existing targeted imaging pipelines, thereby further increasing imaging efficacy. This assay provides technical means to run large screens in virtually any other three-dimensional cell culture system, for instance various organoid types or tumor spheroids.

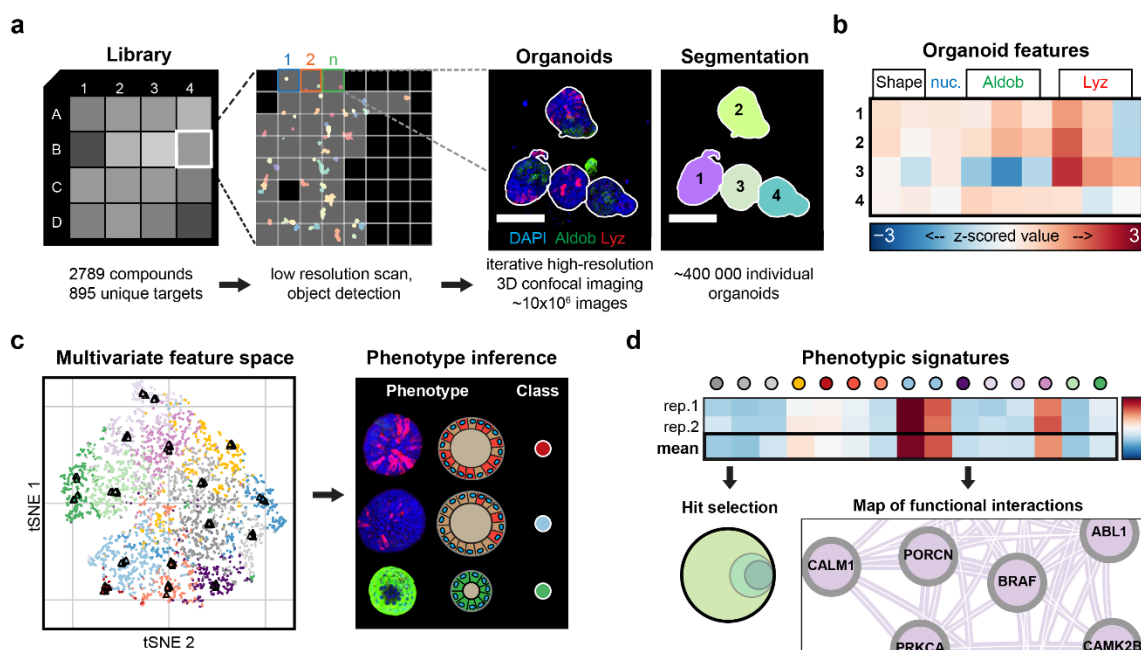


Figure 7: From phenotypic screen to functional genetic interactions

a, Overview of the screening assay and automated iterative imaging pipeline, **b**, Extracted multivariate feature array per object. **c**, tSNE representation of the multivariate feature space used for unbiased phenotype detection and classification. **d**, Phenotypic signature for each screened condition used to select hits and infer functional genetic interactions from the phenotypic landscape.

To describe the phenotypic diversity observed in the screened conditions in a quantitative way, individual organoids can be clustered by phenotypic similarity using multivariate feature arrays describing every individual object (**Figure 7b**). There are many clustering methods that mostly vary in distance metric used to infer similarity between data points in the multidimensional space. However, most of these methods require an assumption on the number of groups or clusters present in the data which in this case was not known a priori. To overcome this limitation I used a method developed for identifying subpopulations in multidimensional single cell data,

PhenoGraph (Levine et al., 2015) (**Figure 7c**). PhenoGraph models the feature space of individual organoids with a nearest-neighbor graph whereby each organoid is represented by a node and connected by a set of edges to a neighborhood of highly similar objects. This graph infers phenotypic similarity simultaneously condensing the data structure and is used to identify sets of highly interconnected nodes, termed communities. As community detection algorithms make no assumption about the size, number, or form of subpopulations, they are instrumental to the goal of inferring the number of phenotypes in a data-driven manner.

My analysis revealed that the phenotypic landscape is highly complex, characterized by presence of several phenotypes even under steady state conditions. To factor this into the analysis, I used relative abundance (enrichment or depletion) of each detected phenotype in every screened condition, generating quantitative phenotypic fingerprints (**Figure 7d**). These described both the magnitude of the observed phenotypic effect and the reproducibility between replicas of the same condition, at the same time maintaining the phenotypic resolution. I used this method to select 342 conditions fulfilling the phenotypic effect strength and reproducibility criteria which corresponded to 230 unique target genes. As this method allows precise quantification in samples presenting pleotropic phenotypes, I expect it to be well suited for other datasets with single object resolution. It could for instance be used for assessing drug response in cancer cell lines, giving means to incorporate cell-to cell variability in the analysis and revealing the effects of drugs on the entire tumor ecosystem.

Furthermore, phenotypic fingerprints proved to be useful not only for hit selection but ultimately allowed to infer a map of functional interactions from a single screen. For this, I calculated hierarchical interaction score (HIS) values for identified 230 genes using the phenotypic fingerprints as multivariate input. Generated HIS values were then used to infer interactions between identified targets described by strength (similarity of the phenotypic signatures) and the phenotypic resolution (which phenotypic class contributed most to inferring an interaction). Inferred HIS interactions enriched for genes functionally co-annotated in public databases, that I validated by assessing the probability of a pair of genes connected by non-zero HIS edge to be co-annotated with same KEGG or GO term (**Appendix 1**). My results show an increase in such

probability for genes selected as hits as compared to the initial library but also a correlation of gene pair co-annotation probability with the HIS value for the given interaction. Thus, I was able to both identify previously known but also infer novel functional interactions from a single screen by quantitative analysis of the phenotypic landscape.

In the first part of this section, I present additional data showing how the generated map of functional interactions could further be used to infer the hierarchical relationships between phenotypes and to map the symmetry breaking event in early organoid development.

1. Inferring the symmetry breaking event from the phenotypic space

The inferred HIS interactions together form a landscape with modular composition: the connectivity is distributed unequally with groups of nodes forming dense subnetworks, that can be seen as blocks in the heatmap representation of the HIS interaction landscape (**Appendix 1, Figure 8a, b**). Nodes connecting such clusters correspond to genes placed upstream in the HIS hierarchy, indicating potential key players in organoid development, as seen for beta-Catenin, an integral part of canonical Wnt signaling (**Appendix 1**).

Intuitively, certain phenotypes would be expected to bifurcate from the normal developmental trajectory at earlier steps of organoid development. For example, formation of the *enterocyst* phenotype implies absence of Paneth cells and subsequent differentiation to absorptive cells, meaning that commitment to this phenotype occurs at the symmetry breaking event, when initial Paneth cells appear. Commitment to other phenotypes, characterized by presence of Paneth cells, such as *progenitor-reduced* on the other hand would be expected to happen after the symmetry breaking event.

To characterize these hierarchical relationships between phenotypes, I generated a branching diagram representing the phenotype lineage tree (**Figure 8c**) from hierarchically clustered HIS interaction matrix. In this dendrogram the leaves branch off in the sequence of least co-occurrence with other phenotypes.

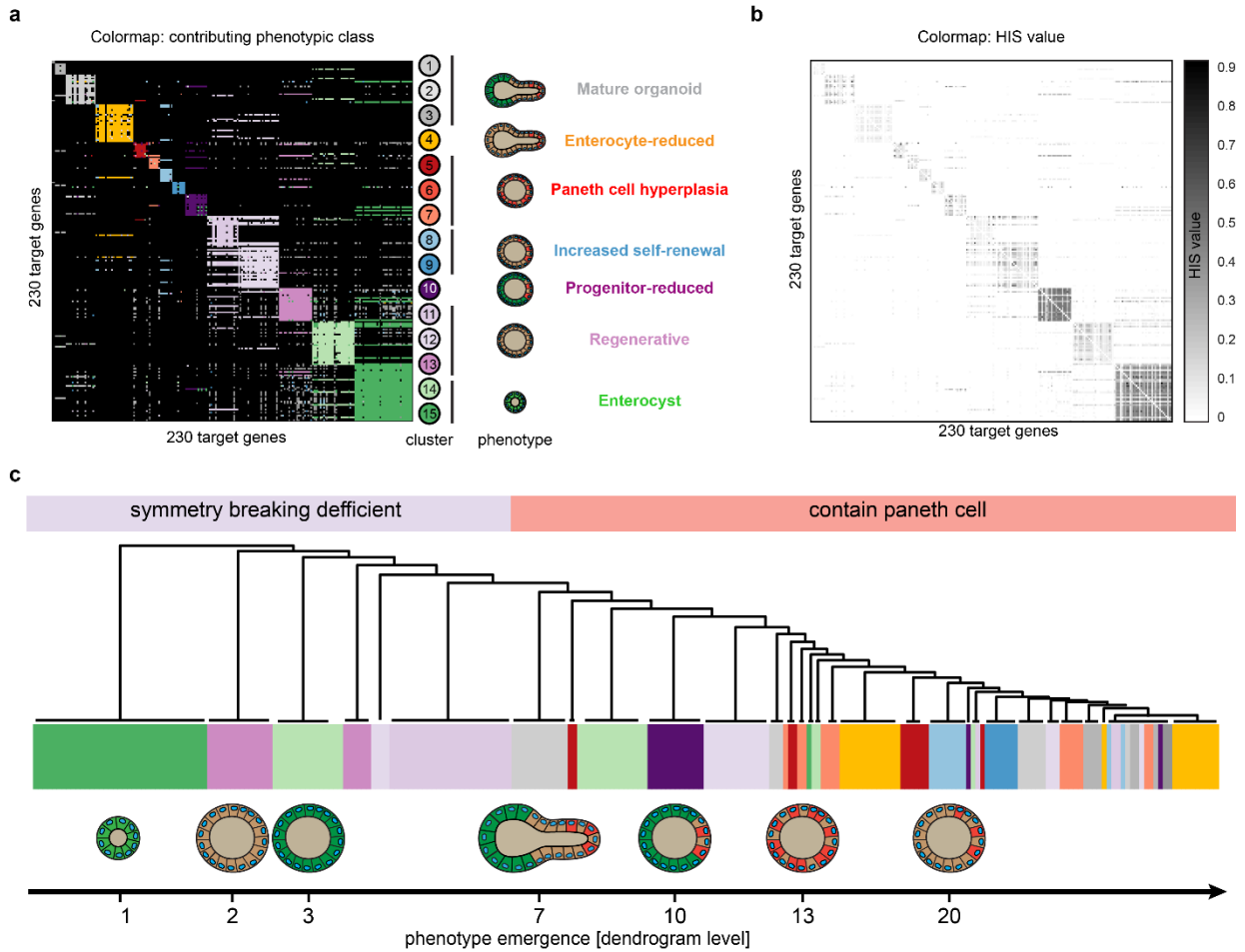


Figure 8: Inferring the symmetry breaking event from the HIS interaction landscape

a, **b**, Heatmaps of the HIS pairs for the 230 target genes, color-coded for the phenotypic class readout contributing most to HIS value inference (**a**) or for the HIS value (**b**). **c**, Dendrogram depicting co-occurrence of phenotypes in screened conditions inferred from Cityblock distance metric analysis of the HIS interaction matrix in **b**.

In-line with the empirical considerations described above, the first 5 dendrogram levels separate conditions enriched for phenotypes deficient for symmetry breaking and characterized by absence of Paneth cells. The first branch consists of the *enterocyst* phenotype with premature terminal differentiation to enterocyte lineage. The second branch consists solely from conditions enriched in organoids lacking both differentiated cell types, with the organoids unable to break symmetry but also prevented from undergoing terminal differentiation (*regenerative*

phenotype). Downstream branching sequence suggests that other phenotypes observed in the screen are formed after the inferred position of the symmetry breaking event and can co-occur with mature organoids.

To further investigate the relationships between phenotypic clusters, I collaborated with the group of Fabian Theis to use their recently developed method, partition-based graph abstraction or PAGA (Wolf et al., 2019). PAGA relies on using graph-like maps of individual objects in multivariate feature space that preserve both continuous and disconnected structure in data at multiple resolutions (**Figure 9a**). The data-driven principle of PAGA allowed to robustly reconstruct branching gene expression changes and was successfully applied to reconstruct the lineage relations of a whole adult animal (Plass et al., 2018).

We used PAGA to generate a map describing the connectivity between the 15 identified phenotypic clusters (**Figure 9b**). Similarly to the dendrogram representing the phenotype lineage tree (**Figure 8b**), PAGA graph was strongly partitioned into phenotypes with either successful or failed symmetry breaking event. This structure reflects the sequence of events during organoid formation: if symmetry breaking is not successful, there are only two possible outcomes, either *enterocyst* or *regenerative* phenotype, making formation of the mature organoids impossible. Successful symmetry breaking on the other hand allows formation of the mature organoids that co-occur with other phenotypes formed post-symmetry breaking.

Analysis of the PAGA graph also delivered further insights, showing strong relations between the phenotypes often observed in Wnt hyperactivating conditions (such as GSK3 β inhibitors) and those typical for Notch inhibitors (such as γ -secretase inhibitors). In fact, both phenotypes are characterized by overabundance of Paneth cells consistent with regulation of secretory cell fate by combined action of Wnt and Notch signaling.

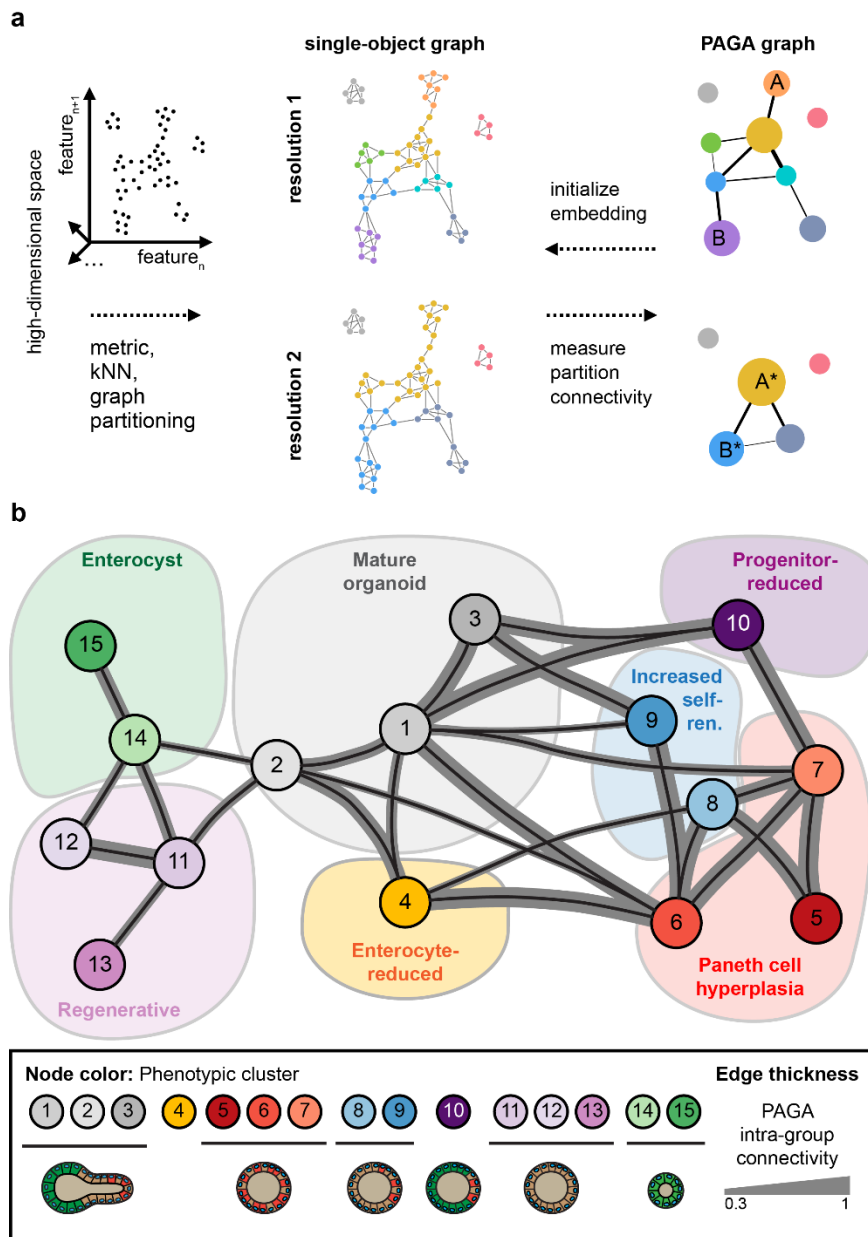


Figure 9: PAGA partitioning of the organoid phenotypic space

a, Schematic of the PAGA principle. High-dimensional data is represented as a kNN graph that is then partitioned at a desired resolution where partitions represent groups of connected nodes. A PAGA graph is obtained by associating a node with each partition connecting each node by weighted edges. After discarding low weight-edges, PAGA graph reveals the topology of the data at a chosen resolution showing connected and disconnected regions. Adapted from Wolf et al. (2019). **b**, PAGA graph of the organoid dataset using the same feature space as used for PhenoGraph clustering. Node color and edge thickness: see legend.

In summary, we were able to infer the symmetry breaking event from the data using two different methods. In the first case I inferred functional interactions using HIS and subsequently analyzed the resulting network for clusters of genes tightly linked together by HIS-determined interactions. In the second case we used the same set of features describing every individual organoid as was used for PhenoGraph clustering to generate a PAGA map, observing in both cases a separation of conditions with high penetrance of the symmetry breaking-deficient phenotypes (*enterocyst* and *regenerative* phenotypes) from other phenotypic outcomes.

The *enterocyst* phenotype is also observed under endogenous conditions and was previously reported by our group (Serra et al., 2019). It emerges from failure to produce initial Paneth cells followed by differentiation towards absorptive lineage after withdrawal of exogenous Wnt. This illustrates how intestinal progenitor cells default towards enterocyte fate in absence of exogenous growth-promoting signals such as Wnt3a. Consistently, inhibiting the Wnt pathway by destabilizing β -catenin resulted in a strong increase in *enterocyst* phenotype. As shown in the Appendix 1, *enterocyst* is also a frequent phenotypic outcome in conditions inhibiting cell cycle or metabolic machinery such as MTOR signaling, possibly due to premature cell cycle exit and differentiation. In case of the *regenerative* phenotype however, organoids remain in an undifferentiated state even though no Paneth cells are formed, meaning that conditions in which this phenotype is enriched promote the regenerative capacity of the intestinal epithelium even in absence of exogenous Wnt stimulation. Among these conditions I have observed the highest phenotypic penetrance for two genes that function in the retinoic acid signaling pathway and focused on these for the follow-up studies.

2. Retinoic acid signaling

As outlined above, phenotypic screen has identified modulators of the retinoic acid signaling pathway to influence the differentiation potential of the progenitor cells with stimulation (agonist treatment) promoting differentiation towards absorptive cell fate and inhibition (antagonist treatment) drastically reducing the amount of differentiated cells. In this section I will discuss the phenotypic effects of perturbed RA signaling and metabolism in intestinal organoids.

2.1 Nuclear retinoic acid receptors RXR and RAR

RXR and RAR are nuclear receptors activated by ligand binding and are uniquely able to translate changes in ligand abundance directly to gene expression. Mechanism of target gene expression activation has been subject of extensive research and many aspects of the nuclear receptor signaling have been described in meticulous detail (Evans and Mangelsdorf, 2014). An interesting feature of nuclear receptor signaling is the ability of RXR to form heterodimers with a plethora of partner nuclear receptors making RXR crucial for mediating gene expression response in several pathways, such as Retinoic acid (RA) signaling, Peroxisome proliferator-activated receptor (PPAR) signaling and numerous others (Evans and Mangelsdorf, 2014).

RXR-RAR heterodimers in particular have been shown to bind regions of DNA containing retinoic acid response elements (RAREs) and to mediate repression of target gene expression in ligand-unbound *apo*-state (Rochel and Moras, 2014). The heterodimer is activated by binding of a vitamin A metabolite *atRA* to RAR mediating a conformation change to *holo*-state that drives recruitment of co-activator machinery and ultimately activates target gene expression. Although *atRA* is widely used to induce differentiation in ES cell cultures (Martinez-Ceballos and Gudas, 2008), the exact role of RA signaling in tissue homeostasis and adult stem cell differentiation is less studied.

As described in Appendix 1, RA has shown a differentiation-promoting effect in the context of intestinal organoids with an inverse effect observed for inhibition of the pathway. Whereas *atRA*

and 9cis-RA treatment conditions had high occurrence of *enterocyst* and *progenitor-reduced* phenotypes, RXRi treatment manifested in highly penetrant *regenerative* phenotype. The RXRi treatment phenotype featured nuclear retention of YAP1, only observed in early steps of organoid formation under control conditions that was retained even after withdrawal of exogenous Wnt3A. This homogenous YAP1 nuclear localization could also explain the absence of Paneth cells in this condition: firstly, as discussed above, variability in YAP1 subcellular localization precedes establishment of Notch-driven lateral inhibition. Secondly, sustained nuclear Yap activity has also been shown to inhibit Wnt target genes, depleting the pool of Lgr5+ stem cells (Barry et al., 2013). As Math1, a transcription factor crucial for secretory lineage commitment, is a known Wnt target gene, its suppression in RXRi treatment condition, together with the inability to establish delta-Notch interactions would explain the observed Paneth cell deficiency.

To understand the downstream transcriptional output of the RA signaling, I profiled RXRi- and retinoid-treated organoids using RNA sequencing, observing significant changes in expression of 1884 genes. RXRi treatment resulted in retention of a transcriptional profile characteristic for early organoids and upregulation of genes associated with fetal-like transition in the intestinal epithelium (**Appendix 1**). When explored in detail, RXRi-induced transcriptional changes feature upregulation of both positive cell cycle regulators and DNA repair machinery. The latter observation is interesting as it sheds light on DNA damage control in rapidly cycling cells (**Figure 10**) and suggests that RXRi-induced phenotype is indeed regenerative, whereby cells upregulate positive regulators of the cell cycle but also ensure that frequent replication does not lead to accumulation of DNA damage. This is supported by enrichment of genes in RXRi treated organoids functionally annotated with base mismatch repair (KEGG annotations: *Nucleotide excision repair* and *Mismatch repair*) and interstrand cross-link repair (KEGG annotation: *Fanconi anemia pathway*).

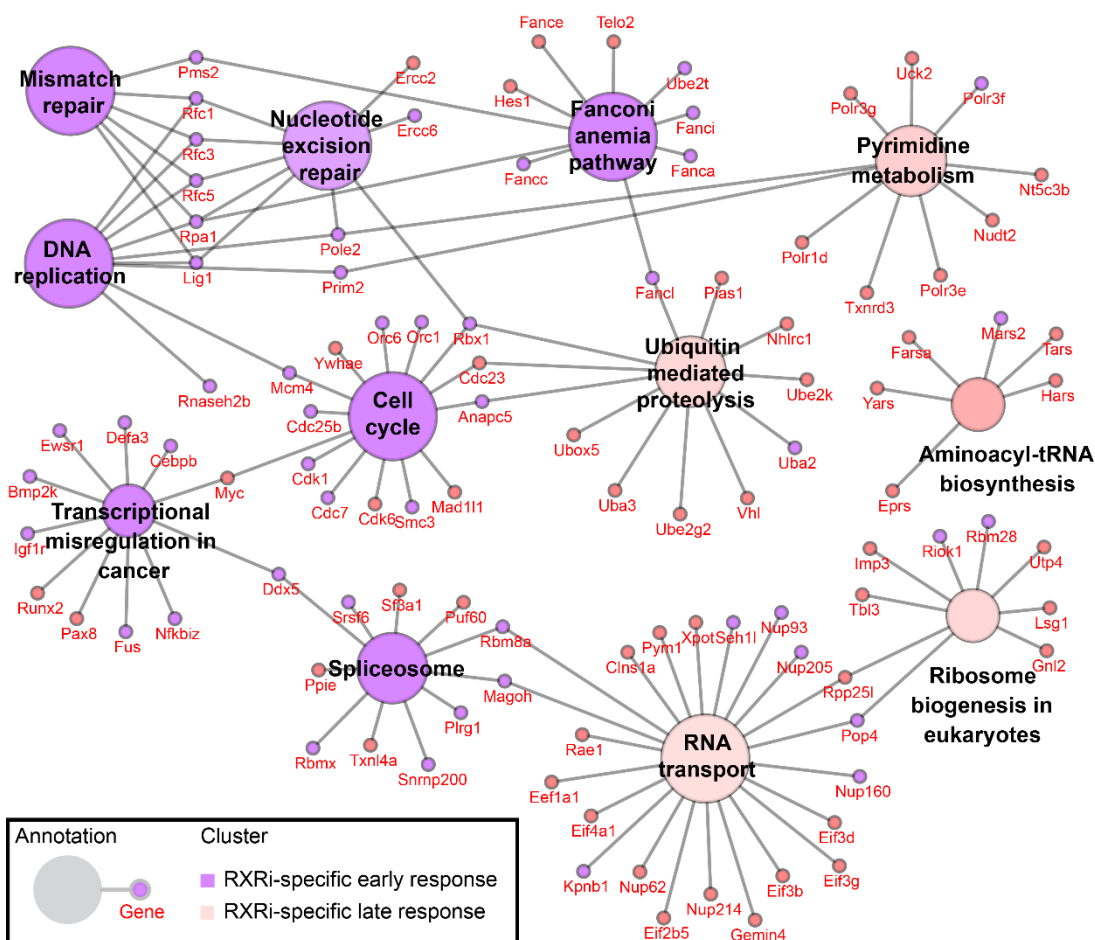


Figure 10: RXR antagonist treatment-induced transcriptional changes

Network representation of annotation enrichment analysis for genes upregulated regulated at 6 and 24 hour time point in RXRi treated organoids. Small nodes show genes, large nodes show functional annotations. Color indicates time point-specific annotation enrichment (see network legend).

My observations highlighted the importance of endogenous RA signaling for enterocyte differentiation and exit from the regenerative state. However the tool compounds I used acted at the level of nuclear receptors, directly perturbing the transcriptional output. In order to understand the regulation of endogenous RA signaling, it was thus necessary to explain the upstream mechanisms controlling the RA signaling activity.

2.2 Metabolic control through RA availability

The best studied function of the RXR-RAR heterodimer is exerted during embryo development where atRA acts as a crucial morphogen forming a pattern along the anterior-posterior axis. RA signaling function in this context relies on precise control over target gene expression through atRA concentration that is modulated at the level of synthesis and degradation (Sakai et al., 2001). My investigation of RA metabolism in the intestinal organoids (**Appendix 1**) shows that the conversion of retinylaldehyde to atRA by ALDH1A1 is a characteristic feature of the enterocytes resulting in biased expression of genes carrying RARE motifs in these cells under homeostatic conditions (**Figure 11a, Appendix 1**). Consequently, organoids cultured in medium lacking retinol exhibited phenotypes similar to those of RXRi-treated organoids, featuring reduced absorptive cell numbers, increased proliferation and nuclear translocation of YAP1, with an inverse phenotype observed in atRA-treated organoids (**Figure 11b**).

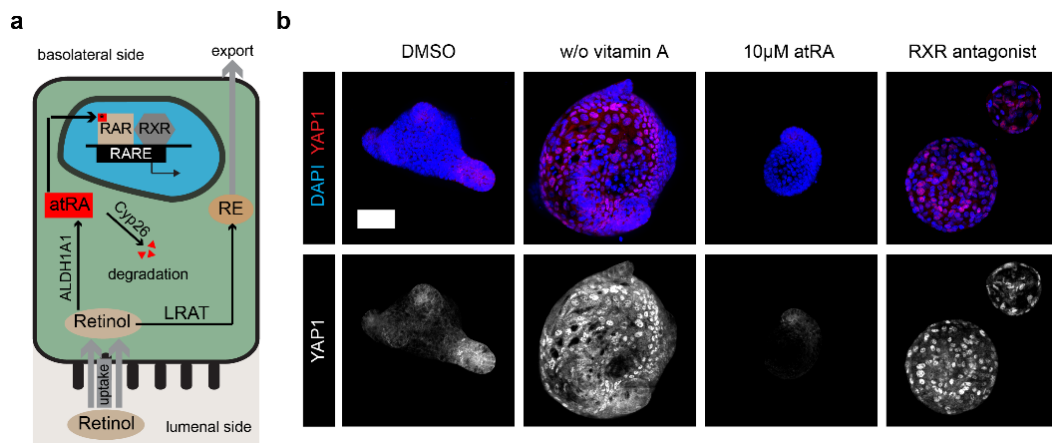


Figure 11: Vitamin A is necessary for enterocyte differentiation

a, Schematic depiction of retinol metabolism in intestinal epithelial cells. Retinol is taken up from the lumen, converted atRA by ALDH1A1, in the nucleus atRA binds Retinoid X receptor RXR-RAR heterodimers bound to Retinoic acid response elements (RARE) activating target gene expression. Retinol can alternatively be metabolized to retinyl ester (RE) and transported to the lymph system, excess atRA can be degraded by cytochrome p450 enzymes (Cyp26). **b**, Representative images of day 4 organoids cultured from single cells in indicated treatment conditions. Composite maximum intensity projection of a confocal z-stack, nuclei, DAPI, antibody staining for YAP1, scale bar, 50 μm .

This phenotype is also in-line with increased abundance of proliferating ki67⁺ cells in both RXRi and retinol-free conditions (**Appendix 1**). Taken together, ALDH1A1 acts as a crucial regulator of retinol metabolism, exerting control over expression of RARE-driven genes. These genes define the absorptive enterocytes and are required for their differentiation, as evident from enterocyte-deficient phenotypes in RXRi and retinol-free conditions.

Based on these observations I propose a model where activation of RA metabolism ensures directionality in enterocyte differentiation by initiating a positive feedback loop. As cells move away from the crypt, they upregulate ALDH1A1, resulting in higher intracellular atRA levels and driving the expression of enterocyte-specific genes, thus ensuring irreversible differentiation to absorptive lineage. Compromised RA signaling and metabolism on the other hand render cells unable to exit the regenerative state and increase the pool of cycling progenitors characterized by nuclear YAP accumulation. At the organoid level this manifests in higher numbers of cycling progenitors at the cost of enterocyte fraction with subsequent increase in organoid size. Interestingly, also in other systems, such as the colitis-induced colonic tumor model, the tumorigenesis potential arises from altered retinoic acid metabolism (Bhattacharya et al., 2016) indicating that cells with compromised RA supply are more likely to remain in an undifferentiated and proliferative state.

3. Loss of intestinal identity is linked to Cdx2

Functional annotation enrichment analysis of RNA sequencing data and comparison with tissue type-specific transcriptional profiles have revealed a significant reduction in expression of small intestine-specific genes in RXRi-treated organoids (**Appendix 1**). At the same time, RXRi-treated organoids featured upregulation of genes characteristic for more anterior GI tract tissues and genes associated with fetal-like transition in intestinal epithelium, suggesting loss of intestinal transcriptional signature (**Appendix 1**). In this section I will expand on the mechanism underlying the regenerative phenotype observed for inhibition of retinoic acid signaling, showing that loss of intestinal identity is linked to the transcription factor Cdx2.

3.1 Cdx2 expression is necessary for establishing intestinal identity

Cdx2 is expressed in the posterior part of the digestive tract during development (Stringer et al., 2012), forming a sharp boundary at the junction of stomach and duodenum (Silberg et al., 2000). Consistently, Cdx2 expression needs to be induced for generating PSC-derived intestinal organoids (Spence et al., 2011), highlighting its crucial role for acquiring the intestinal identity. Furthermore, Cdx2 deletion has been shown to lead to autonomous reprogramming of intestinal organoids to stomach organoids (Simmini et al., 2014). Similarly, conditional knockout of Cdx2 in mouse early endoderm resulted in replacement of the intestinal epithelium with keratinocytes of esophageal identity (Gao et al., 2009). Collectively, these observations suggest that lack of Cdx2 results in ectopic activation of a more anterior foregut program in the intestine. Aberrant Cdx2 expression on the other hand is associated with intestinal metaplasia, for example in Barrett's Esophagus (Eda et al., 2003), suggesting that Cdx2 specifically defines the posterior endoderm identity and shapes the intestinal transcriptome through activation and maintenance of expression of intestine-specific transcription factors such as Isx, Cdx1 and HNF1a (Gao et al., 2009). Furthermore, the anteriorization observed in Cdx2 mutant colon (Beck et al., 1999) and intestine (Gao et al., 2009) suggests that Cdx2 is responsible for suppression of the foregut differentiation program in the intestinal cells. I thus postulate that Cdx2-responsive genes mediate the transition to the intestinal transcriptional profile in later stages of organoid development, whereas lack of Cdx2 would result in a permissive environment and an anteriorized transcriptional identity of organoids.

In the RNA sequencing experiment in compound-treated organoids (**Appendix 1**), genes showing differential expression between treatments were clustered according to their expression profile. This revealed that genes upregulated in retinoid-stimulated organoids were downregulated in RXRi condition, while genes upregulated in RXRi were downregulated by retinoid treatment (**Figure 12a, b**). When analyzed for presence of Cdx2 binding motifs in proximity of the promotor region, expression profile clusters with the highest percentage of Cdx2 motif-containing genes were among the ones showing strongest downregulation in RXRi treated organoids (**Figure 12c**).

Consistently, clusters of genes depleted of these motifs were the highest upregulated in the RXRi condition.

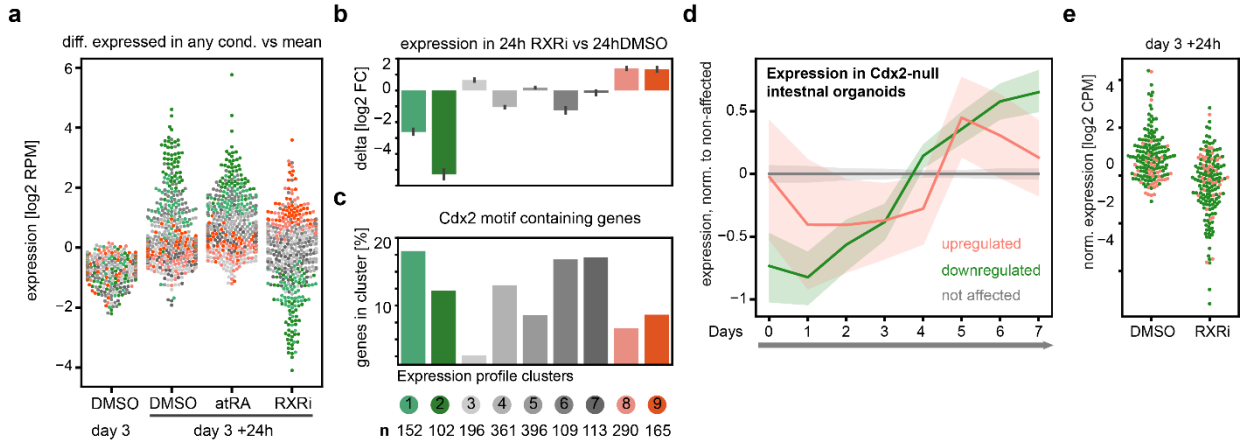


Figure 12: RXR antagonist treatment resembles Cdx2-null transcriptional signature

a, Swarm plot depicting expression values of selected 1884 genes in day 3 untreated organoids and in indicated treatment conditions 24h hours after treatment. Every data point is a gene, color coded for assigned cluster label (k-means clustering). Stratified sampling, 50 genes per cluster, color-coded by expression profile cluster. **b**, Bar plots depicting mean expression of genes from respective clusters in the RXR antagonist treated condition compared to DMSO (log2 fold change). **c**, Bar plots depicting abundance of genes containing Cdx2 binding motifs in assigned clusters. **d**, Expression of genes up- or downregulated in Cdx2-null organoids during intestinal organoid development, solid lines indicate mean values per time points, opaque interval shows standard deviation. **e**, Expression of genes up- or downregulated in Cdx2-null organoids in control and RXRi-treated organoids. **b**, **c**: Data shown for the indicated number of genes composing each cluster as mean \pm s.d.

To obtain an independently validated list of genes that behave as Cdx2 targets, I selected genes that were downregulated in Cdx2-null intestinal organoids (Simmini et al., 2014), observing upregulation on transition from day 3 to day 4 of organoid development, sustained from day 4 onwards (**Figure 12d**). In the RXRi-treated organoids, Cdx2 target genes were similarly downregulated (**Figure 12e**), corroborating the results of transcription factor binding site analysis. Taken together, this shows that both during early stages of organoid development and in the RXRi treatment condition cells do not upregulate Cdx2-dependent expression programs.

This orthogonal behavior indicates that Cdx2 targets are suppressed in cells with compromised RA signaling, however, how this regulation is achieved was not clear.

3.1 Cdx2 expression depends on RA signaling activity

To understand whether RXR signaling directly affects Cdx2 levels, I imaged organoids cultured in presence of RXR antagonist and exogenous retinoic acid, observing significantly reduced levels of Cdx2 in RXRi-treated organoids both in wild-type organoids (**Figure 13a, b**) and in Cdx2-EGFP transgene line (**Figure 13c**).

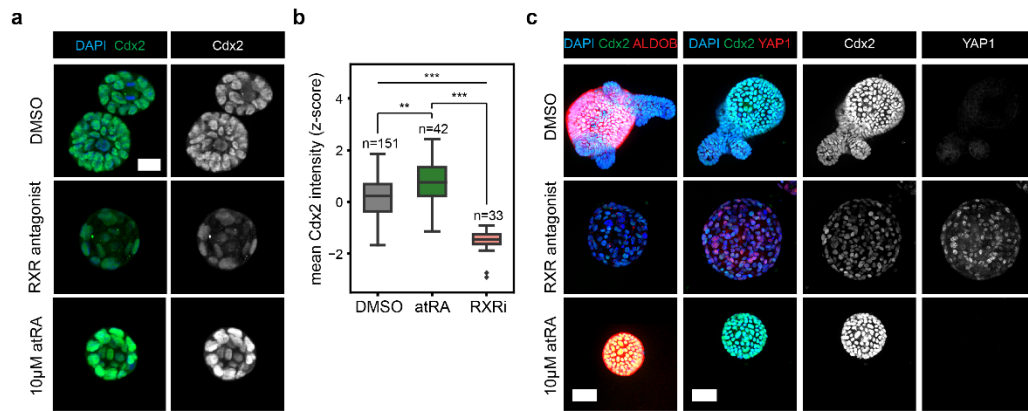


Figure 13: Cdx2 expression relies on RXR activity

a, Representative images of day 2.5 organoids cultured from single cells in indicated treatment conditions. Composite maximum intensity projection of a confocal z-stack, antibody staining for Cdx2 as indicated, nuclei, DAPI, scale bar, 20 µm. **b**, Box plot showing the mean Cdx2 intensity in organoids from conditions shown in **a**. Asterisk indicate statistical significance (Students t-test). **c**, Representative images of day 4 Cdx2-EGFP organoids cultured from single cells in indicated treatment conditions. Composite maximum intensity projection of a confocal z-stack, Cdx2-GFP, antibody staining for Aldolase B (left panel) and YAP1 (right panel), scale bar, 50 µm.

Interestingly, RA treatment resulted in higher Cdx2 expression, similarly Cdx2 expression was higher in post-mitotic Aldolase B-positive enterocytes as compared to the crypt cells (**Figure 13a-c**).

In fact, the intestinal metaplasia observed when Cdx2 is ectopically expressed in the gastric mucosa is foremost characterized by differentiation of functionally mature absorptive enterocytes (Mutoh et al., 2005), underlining that Cdx2 is necessary and sufficient for enterocyte development. My observations on RA signaling activity suggest that Cdx2 expression in intestinal organoids is dependent on RA signaling input: enterocytes exhibit active RA signaling and, consequently, have higher Cdx2 levels, suggesting regulation of Cdx2 expression by RA signaling.

During embryo development, RA signaling is crucial for correct patterning of main body axes that is achieved by RA-patterned spatial domains of Hox gene expression. While Hox gene code is crucial for the correct zonation of the endoderm along the AP axis, there are at least two non-Hox transcription factors necessary for the gut formation, Pdx1 and Cdx2. Cdx2 acts as an integrator of the combined Fgf, Wnt and RA signaling input (Savory et al., 2009) and its function seems to be independent of Hox genes (Gao et al., 2009). In avian development, compromised RA signaling activity has been shown to influence expression of Cdx2 homolog CdxA, resulting in loss of CdxA expression in the developing intestine (Bayha et al., 2009). Much less is known about regulation of Cdx2 expression by RA signaling in mammals. Based on my observations, it is feasible to suggest RA-mediated control of intestine-specific genes through regulation of Cdx2 expression by RA-responsive elements. Furthermore, such regulation could be decoupled from the RA effect on the expression of Hox genes, enabling control over tissue identity in intestine regeneration in adult organisms where the AP axis has already been established.

Nonetheless, other types of regulation cannot be excluded, such as co-regulation of Cdx2 targets by RXR-RAR heterodimers, whereby RA signaling controls the chromatin accessibility, “priming” Cdx2 target genes. This hypothesis could be validated with a ChIP experiment, assessing the relative positions of bound RXR-RAR heterodimers around the promoter regions of Cdx2 target genes. An enrichment of occupied RARE elements around the promoters of Cdx2 target genes could indicate that RARE elements act as enhancers for these genes. This hypothesis is supported by reported presence of liganded RXR at the active enhancer sites in macrophages (Daniel et al., 2014).

Based on the results discussed above I propose a model in which endogenous RA signaling is involved in two key steps of organoid development. First, as cells undergo a regenerative response forming the initial cyst structure, they lose intestinal identity and reacquire it after day 3 of organoid development. Compromised RA signaling at this stage results in lower Cdx2 levels and causes expression of a more anterior transcriptional program. This identity change could be mediated by misexpression of more anterior patterning cues, such as Wnt10a, as has been observed for developing Cdx2-null mouse intestine (Gao et al., 2009). This switch however seems to be insufficient for ectopic activation of esophageal or stomach transcriptome and rather forces the organoids to remain in an undifferentiated state. Whether RA signaling inhibition could be exploited to transform intestinal to esophageal or stomach organoids poses a biologically interesting question. This could be approached by removing the RXR antagonist from organoids at the cyst stage while concomitantly providing more anterior patterning cues, such as Wnt10a.

The second important step in organoid development involving RA signaling occurs when intestinal identity is reacquired after symmetry breaking and differentiated cell types begin to appear. Exit from the rapidly proliferating TA cell state and commitment to absorptive lineage requires endogenous RA activity mediated by the RXR-RAR heterodimer complex. Subsequently, RA signaling is required for enterocyte functional maturation and is associated with higher Cdx2 levels in enterocytes. Differentiation-inducing effect of RA treatment can thus be explained by increased expression of Cdx2 and downstream intestine-specific program, ensuring commitment to enterocyte fate but also resulting in reduced plasticity.

Taken together, my results show that RXRi treated organoids fail to acquire the transcriptional identity of mature intestinal epithelium due to inability to initiate and sustain Cdx2-driven intestine-specific transcriptome. This results in an earlier transcriptional signature characterized by higher expression of both anterior and regeneration-related genes, accompanied by YAP1 nuclear translocation and active cell cycle maintenance.

4. RXR α treatment improves intestinal regeneration *in vivo*

To understand the physiological implications of perturbed RA signaling in intestinal epithelium regeneration, together with our collaborators we conducted an *in vivo* study in mice using irradiation-induced cycling cell ablation to trigger a regenerative response. Results of the *in vivo* assay were consistent with regeneration-promoting effect of RXR α treatment: RXR α -treated mice exhibited reduced weight loss and improved intestinal barrier integrity during recovery from irradiation-induced crypt ablation (**Appendix 1**). At the tissue level, cycling cell ablation results in progressive cell mass loss and subsequent villi shortening. Consistently, mice treated with RXR α after irradiation exhibited less intestine decellularisation and longer villi compared to irradiated vehicle-treated mice (**Figure 14**). This could be explained by an increase in cycling cells in the RXR α treated mice, an effect observed in the intestinal organoids.

Interestingly, histology imaging also suggests that the increase in cycling cells is transient. In our *in vivo* study mice were pulsed with the compound twice, with the second treatment 72 hours before necropsy. In the collected samples we observed increased villus length and presence of secretory cells, however no significant increase in ki67⁺ cycling cells in the intravillus region (**Figure 14**). This could be explained by two factors: firstly, RXR α treatment could result in a temporally restricted increase in cycling cell abundance that differentiate upon compound withdrawal, resulting in improved villi formation. Secondly, establishment of the crypt could be a more gradual process that, similarly to the de novo crypt formation during organoid development, takes place after the villi have been formed.

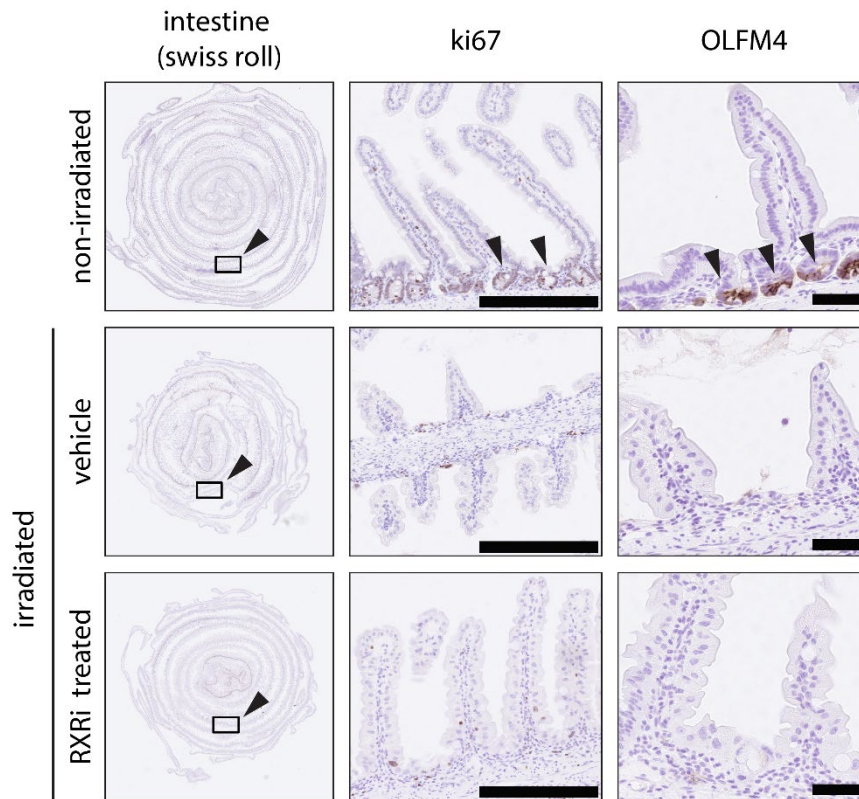


Figure 14: RXRi treatment improves intestinal epithelium regeneration

Histological images of the small intestine from mice from indicated treatment groups (left, arrowheads and rectangles indicate the region displayed in the middle and right panels), antibody staining for ki67 (middle) and OLFM4 (right), scale bars, 250 μm and 50 μm respectively, arrowheads indicate crypts.

Further studies could shed light on the dynamics of increased proliferation caused by RXRi treatment: in order to validate whether RXRi treatment in irradiated mice indeed results in a transient expansion of the cycling cell pool, histological samples would need to be harvested at earlier time points, possibly within 24 hours after compound treatment. Similarly, further studies would be required to describe the process of intestinal crypt formation. For this, a longer time frame of the *in vivo* study would be instrumental, which could require irradiation of a smaller fragment of the intestine to mitigate the weight loss in mice, prolonging their survival.

5. Concluding remarks

In this thesis I show how functional genetic interactions can be inferred from a single screen using phenotypic fingerprints. This approach can be used on any other arrayed screen with single object resolution offering means to robustly identify phenotypic effects also in a complicated landscape characterized by pleiotropic phenotypes.

Secondly, I characterized a set of 230 genes that influence the phenotypic outcome of intestinal organoid formation. This data set can be used to explore novel functional modules involved in intestinal organoid regeneration and homeostasis as exemplified by the follow up studies where I investigated the RA signaling.

Furthermore, I identified the upstream regulation of the RA signaling, showing how it is controlled by metabolism of retinol in a cell type-specific manner. Speculating, RA signaling could serve as functionally redundant or complimentary to BMP signaling, establishing an opposing gradient to the Wnt activity, possibly in a cell-autonomous manner. This would explain the functional role of retinol metabolism in cell fate control, ensuring directionality in TA to enterocyte transition and shaping the crypt-villus boundary.

Lastly, results from our mouse study suggest that transient inhibition of RXR likely sets off a pulse of increased cell proliferation, resulting in improved regeneration of functional villi. This work served as a basis for the patent application EP19182782.3, where we propose RXR antagonists as potential therapeutics for improving tissue regeneration upon acute damage. Together with recent reports of regeneration-promoting fasting diet it could pose an interesting and promising strategy in mitigating effects of acute intestinal damage, for instance in cancer patients undergoing radiation and chemotherapy.

ACKNOWLEDGEMENTS

I would first of all like to thank Prisca for being a great mentor over the time of my PhD. She helped and supported me but at the same time was understanding and gave me freedom to explore unexpected results. Prisca's endless drive for science, her energetic and optimistic approach helped me to get through the rough patches of my PhD. Ultimately, I am very happy to have had the opportunity to do my PhD project in her lab, and I would do it again if I had to choose! I would also like to thank my thesis committee, Matthias Lütolf and Jörg Betschinger, for helping shape the project over the course of these years and providing constructive feedback and fruitful discussions.

The time I spent in Prisca's lab was an amazing experience in many respects, I am very happy to have witnessed the very beginning and how the lab developed over the years. I would therefore like to thank all of the lab members, past and present for being the best group of people I had the pleasure of working with! I am grateful for the friendly and fun atmosphere, for the support and kind words, for the insightful (and also not so insightful) discussions, for the running jokes, Friday beers in the office and all the great times we had together over the years. My special thank you goes to my office mates, Denise, Marietta and Urs, I really enjoyed your company and you guys are awesome!

I think this project would have not been possible without the support of the FMI facilities and the FMI IT. I am very grateful to the whole FAIM team and Laurent Gelman in particular for helping us build the screening pipeline from scratch. I also owe a special thank you to Enrico Tagliavini for always having an open ear for our IT issues and being resourceful and friendly. I thank Sebastien Smallwood and Michael Stadler for their expertise and professionalism that truly helped this project.

Last but not least I would like to thank my family. I would like to thank my wife Anna-Maria for taking a step into the unknown together with me and being always understanding, cheerful and infinitely supportive. I would like to thank our son Erik for making me want to be a better person

and helping me understand what truly matters. I deeply thank my parents for their love, care and endless support and I think it is the support and comfort given to me by my family that truly made this thesis possible.

REFERENCES

- Alferez, D., Wilkinson, R.W., Watkins, J., Poulson, R., Mandir, N., Wedge, S.R., Pyrah, I.T., Smith, N.R., Jackson, L., Ryan, A.J., *et al.* (2008). Dual inhibition of VEGFR and EGFR signaling reduces the incidence and size of intestinal adenomas in Apc(Min/+) mice. *Mol Cancer Ther* 7, 590-598.
- Andersson, E.R., and Lendahl, U. (2014). Therapeutic modulation of Notch signalling--are we there yet? *Nat Rev Drug Discov* 13, 357-378.
- Barcellos-Hoff, M.H., Aggeler, J., Ram, T.G., and Bissell, M.J. (1989). Functional differentiation and alveolar morphogenesis of primary mammary cultures on reconstituted basement membrane. *Development* 105, 223-235.
- Baron, M. (2003). An overview of the Notch signalling pathway. *Semin Cell Dev Biol* 14, 113-119.
- Barry, E.R., Morikawa, T., Butler, B.L., Shrestha, K., de la Rosa, R., Yan, K.S., Fuchs, C.S., Magness, S.T., Smits, R., Ogino, S., *et al.* (2013). Restriction of intestinal stem cell expansion and the regenerative response by YAP. *Nature* 493, 106-110.
- Bastide, P., Darido, C., Pannequin, J., Kist, R., Robine, S., Marty-Double, C., Bibeau, F., Scherer, G., Joubert, D., Hollande, F., *et al.* (2007). Sox9 regulates cell proliferation and is required for Paneth cell differentiation in the intestinal epithelium. *J Cell Biol* 178, 635-648.
- Bayha, E., Jorgensen, M.C., Serup, P., and Grapin-Botton, A. (2009). Retinoic acid signaling organizes endodermal organ specification along the entire antero-posterior axis. *PLoS One* 4, e5845.
- Beck, F., Chawengsaksophak, K., Waring, P., Playford, R.J., and Furness, J.B. (1999). Reprogramming of intestinal differentiation and intercalary regeneration in Cdx2 mutant mice. *Proc Natl Acad Sci U S A* 96, 7318-7323.
- Beck, F., Erler, T., Russell, A., and James, R. (1995). Expression of Cdx-2 in the mouse embryo and placenta: possible role in patterning of the extra-embryonic membranes. *Dev Dyn* 204, 219-227.
- Bhattacharya, N., Yuan, R., Prestwood, T.R., Penny, H.L., DiMaio, M.A., Reticker-Flynn, N.E., Krois, C.R., Kenkel, J.A., Pham, T.D., Carmi, Y., *et al.* (2016). Normalizing Microbiota-Induced Retinoic Acid Deficiency Stimulates Protective CD8(+) T Cell-Mediated Immunity in Colorectal Cancer. *Immunity* 45, 641-655.
- Bjerknes, M., and Cheng, H. (1999). Clonal analysis of mouse intestinal epithelial progenitors. *Gastroenterology* 116, 7-14.
- Buczacki, S.J., Zecchini, H.I., Nicholson, A.M., Russell, R., Vermeulen, L., Kemp, R., and Winton, D.J. (2013). Intestinal label-retaining cells are secretory precursors expressing Lgr5. *Nature* 495, 65-69.
- Bullen, T.F., Forrest, S., Campbell, F., Dodson, A.R., Hershman, M.J., Pritchard, D.M., Turner, J.R., Montrose, M.H., and Watson, A.J. (2006). Characterization of epithelial cell shedding from human small intestine. *Lab Invest* 86, 1052-1063.
- Butler, C.R., Hynds, R.E., Gowers, K.H., Lee Ddo, H., Brown, J.M., Crowley, C., Teixeira, V.H., Smith, C.M., Urbani, L., Hamilton, N.J., *et al.* (2016). Rapid Expansion of Human Epithelial Stem Cells Suitable for Airway Tissue Engineering. *Am J Respir Crit Care Med* 194, 156-168.

- Cai, J., Zhang, N., Zheng, Y., de Wilde, R.F., Maitra, A., and Pan, D. (2010). The Hippo signaling pathway restricts the oncogenic potential of an intestinal regeneration program. *Genes Dev* *24*, 2383-2388.
- Camargo, F.D., Gokhale, S., Johnnidis, J.B., Fu, D., Bell, G.W., Jaenisch, R., and Brummelkamp, T.R. (2007). YAP1 increases organ size and expands undifferentiated progenitor cells. *Curr Biol* *17*, 2054-2060.
- Chacon-Martinez, C.A., Koester, J., and Wickstrom, S.A. (2018). Signaling in the stem cell niche: regulating cell fate, function and plasticity. *Development* *145*.
- Chan, E.H., Nousiainen, M., Chalamalasetty, R.B., Schafer, A., Nigg, E.A., and Sillje, H.H. (2005). The Ste20-like kinase Mst2 activates the human large tumor suppressor kinase Lats1. *Oncogene* *24*, 2076-2086.
- Chen, C.L., Gajewski, K.M., Hamaratoglu, F., Bossuyt, W., Sansores-Garcia, L., Tao, C., and Halder, G. (2010). The apical-basal cell polarity determinant Crumbs regulates Hippo signaling in *Drosophila*. *Proc Natl Acad Sci U S A* *107*, 15810-15815.
- Ciruna, B., and Rossant, J. (2001). FGF signaling regulates mesoderm cell fate specification and morphogenetic movement at the primitive streak. *Dev Cell* *1*, 37-49.
- Clevers, H. (2016). Modeling Development and Disease with Organoids. *Cell* *165*, 1586-1597.
- Costanzo, M., VanderSluis, B., Koch, E.N., Baryshnikova, A., Pons, C., Tan, G., Wang, W., Usaj, M., Hanchard, J., Lee, S.D., *et al.* (2016). A global genetic interaction network maps a wiring diagram of cellular function. *Science* *353*.
- Daniel, B., Nagy, G., Hah, N., Horvath, A., Czimmerer, Z., Poliska, S., Gyuris, T., Keirsse, J., Gysemans, C., Van Ginderachter, J.A., *et al.* (2014). The active enhancer network operated by liganded RXR supports angiogenic activity in macrophages. *Genes Dev* *28*, 1562-1577.
- Dupont, S. (2016). Role of YAP/TAZ in cell-matrix adhesion-mediated signalling and mechanotransduction. *Exp Cell Res* *343*, 42-53.
- Dye, B.R., Hill, D.R., Ferguson, M.A., Tsai, Y.H., Nagy, M.S., Dyal, R., Wells, J.M., Mayhew, C.N., Nattiv, R., Klein, O.D., *et al.* (2015). In vitro generation of human pluripotent stem cell derived lung organoids. *Elife* *4*.
- Eda, A., Osawa, H., Satoh, K., Yanaka, I., Kihira, K., Ishino, Y., Mutoh, H., and Sugano, K. (2003). Aberrant expression of CDX2 in Barrett's epithelium and inflammatory esophageal mucosa. *J Gastroenterol* *38*, 14-22.
- Eiraku, M., Takata, N., Ishibashi, H., Kawada, M., Sakakura, E., Okuda, S., Sekiguchi, K., Adachi, T., and Sasai, Y. (2011). Self-organizing optic-cup morphogenesis in three-dimensional culture. *Nature* *472*, 51-56.
- Eiraku, M., Watanabe, K., Matsuo-Takasaki, M., Kawada, M., Yonemura, S., Matsumura, M., Wataya, T., Nishiyama, A., Muguruma, K., and Sasai, Y. (2008). Self-organized formation of polarized cortical tissues from ESCs and its active manipulation by extrinsic signals. *Cell Stem Cell* *3*, 519-532.
- Evans, R.M., and Mangelsdorf, D.J. (2014). Nuclear Receptors, RXR, and the Big Bang. *Cell* *157*, 255-266.

- Farin, H.F., Jordens, I., Mosa, M.H., Basak, O., Korving, J., Tauriello, D.V., de Punder, K., Angers, S., Peters, P.J., Maurice, M.M., *et al.* (2016). Visualization of a short-range Wnt gradient in the intestinal stem-cell niche. *Nature* **530**, 340-343.
- Farin, H.F., Van Es, J.H., and Clevers, H. (2012). Redundant sources of Wnt regulate intestinal stem cells and promote formation of Paneth cells. *Gastroenterology* **143**, 1518-1529 e1517.
- Fatehullah, A., Tan, S.H., and Barker, N. (2016). Organoids as an in vitro model of human development and disease. *Nat Cell Biol* **18**, 246-254.
- Fausett, S.R., Brunet, L.J., and Klingensmith, J. (2014). BMP antagonism by Noggin is required in presumptive notochord cells for mammalian foregut morphogenesis. *Dev Biol* **391**, 111-124.
- Fre, S., Huyghe, M., Mourikis, P., Robine, S., Louvard, D., and Artavanis-Tsakonas, S. (2005). Notch signals control the fate of immature progenitor cells in the intestine. *Nature* **435**, 964-968.
- Gadue, P., Huber, T.L., Paddison, P.J., and Keller, G.M. (2006). Wnt and TGF-beta signaling are required for the induction of an in vitro model of primitive streak formation using embryonic stem cells. *Proc Natl Acad Sci U S A* **103**, 16806-16811.
- Gao, N., White, P., and Kaestner, K.H. (2009). Establishment of intestinal identity and epithelial-mesenchymal signaling by Cdx2. *Dev Cell* **16**, 588-599.
- Gao, X., Bali, A.S., Randell, S.H., and Hogan, B.L. (2015). GRHL2 coordinates regeneration of a polarized mucociliary epithelium from basal stem cells. *J Cell Biol* **211**, 669-682.
- Gehart, H., and Clevers, H. (2019). Tales from the crypt: new insights into intestinal stem cells. *Nat Rev Gastroenterol Hepatol* **16**, 19-34.
- Gilbert, S., Nivarthi, H., Mayhew, C.N., Lo, Y.H., Noah, T.K., Vallance, J., Rulicke, T., Muller, M., Jegga, A.G., Tang, W., *et al.* (2015). Activated STAT5 confers resistance to intestinal injury by increasing intestinal stem cell proliferation and regeneration. *Stem Cell Reports* **4**, 209-225.
- Gjorevski, N., Sachs, N., Manfrin, A., Giger, S., Bragina, M.E., Ordonez-Moran, P., Clevers, H., and Lutolf, M.P. (2016). Designer matrices for intestinal stem cell and organoid culture. *Nature* **539**, 560-564.
- Gordon, J.I., and Hermiston, M.L. (1994). Differentiation and self-renewal in the mouse gastrointestinal epithelium. *Curr Opin Cell Biol* **6**, 795-803.
- Gregorieff, A., Liu, Y., Inanlou, M.R., Khomchuk, Y., and Wrana, J.L. (2015). Yap-dependent reprogramming of Lgr5(+) stem cells drives intestinal regeneration and cancer. *Nature* **526**, 715-718.
- Harrison, R.G., Greenman, M.J., Mall, F.P., and Jackson, C.M. (1907). Observations of the living developing nerve fiber. *The Anatomical Record* **1**, 116-128.
- He, X.C., Yin, T., Grindley, J.C., Tian, Q., Sato, T., Tao, W.A., Dirisina, R., Porter-Westpfahl, K.S., Hembree, M., Johnson, T., *et al.* (2007). PTEN-deficient intestinal stem cells initiate intestinal polyposis. *Nat Genet* **39**, 189-198.
- He, X.C., Zhang, J., Tong, W.G., Tawfik, O., Ross, J., Scoville, D.H., Tian, Q., Zeng, X., He, X., Wiedemann, L.M., *et al.* (2004). BMP signaling inhibits intestinal stem cell self-renewal through suppression of Wnt-beta-catenin signaling. *Nat Genet* **36**, 1117-1121.
- Hong, A.W., Meng, Z., and Guan, K.L. (2016). The Hippo pathway in intestinal regeneration and disease. *Nat Rev Gastroenterol Hepatol* **13**, 324-337.

- Huch, M., Dorrell, C., Boj, S.F., van Es, J.H., Li, V.S., van de Wetering, M., Sato, T., Hamer, K., Sasaki, N., Finegold, M.J., *et al.* (2013). In vitro expansion of single Lgr5⁺ liver stem cells induced by Wnt-driven regeneration. *Nature* **494**, 247-250.
- Iakobachvili, N., and Peters, P.J. (2017). Humans in a Dish: The Potential of Organoids in Modeling Immunity and Infectious Diseases. *Front Microbiol* **8**, 2402.
- Jadhav, U., Saxena, M., O'Neill, N.K., Saadatpour, A., Yuan, G.C., Herbert, Z., Murata, K., and Shivdasani, R.A. (2017). Dynamic Reorganization of Chromatin Accessibility Signatures during Dedifferentiation of Secretory Precursors into Lgr5⁺ Intestinal Stem Cells. *Cell Stem Cell* **21**, 65-77 e65.
- Kim, K.A., Kakitani, M., Zhao, J., Oshima, T., Tang, T., Binnerts, M., Liu, Y., Boyle, B., Park, E., Emtage, P., *et al.* (2005). Mitogenic influence of human R-spondin1 on the intestinal epithelium. *Science* **309**, 1256-1259.
- Kim, N.G., and Gumbiner, B.M. (2015). Adhesion to fibronectin regulates Hippo signaling via the FAK-Src-PI3K pathway. *J Cell Biol* **210**, 503-515.
- Kim, T.H., Escudero, S., and Shivdasani, R.A. (2012). Intact function of Lgr5 receptor-expressing intestinal stem cells in the absence of Paneth cells. *Proc Natl Acad Sci U S A* **109**, 3932-3937.
- Korinek, V., Barker, N., Moerer, P., van Donselaar, E., Huls, G., Peters, P.J., and Clevers, H. (1998). Depletion of epithelial stem-cell compartments in the small intestine of mice lacking Tcf-4. *Nat Genet* **19**, 379-383.
- Krejci, A., and Bray, S. (2007). Notch activation stimulates transient and selective binding of Su(H)/CSL to target enhancers. *Genes Dev* **21**, 1322-1327.
- Kubo, A., Shinozaki, K., Shannon, J.M., Kouskoff, V., Kennedy, M., Woo, S., Fehling, H.J., and Keller, G. (2004). Development of definitive endoderm from embryonic stem cells in culture. *Development* **131**, 1651-1662.
- Kuhnert, F., Davis, C.R., Wang, H.T., Chu, P., Lee, M., Yuan, J., Nusse, R., and Kuo, C.J. (2004). Essential requirement for Wnt signaling in proliferation of adult small intestine and colon revealed by adenoviral expression of Dickkopf-1. *Proc Natl Acad Sci U S A* **101**, 266-271.
- Kurmann, A.A., Serra, M., Hawkins, F., Rankin, S.A., Mori, M., Astapova, I., Ullas, S., Lin, S., Bilodeau, M., Rossant, J., *et al.* (2015). Regeneration of Thyroid Function by Transplantation of Differentiated Pluripotent Stem Cells. *Cell Stem Cell* **17**, 527-542.
- Lancaster, M.A., and Knoblich, J.A. (2014). Organogenesis in a dish: modeling development and disease using organoid technologies. *Science* **345**, 1247125.
- Lancaster, M.A., Renner, M., Martin, C.A., Wenzel, D., Bicknell, L.S., Hurles, M.E., Homfray, T., Penninger, J.M., Jackson, A.P., and Knoblich, J.A. (2013). Cerebral organoids model human brain development and microcephaly. *Nature* **501**, 373-379.
- Levine, J.H., Simonds, E.F., Bendall, S.C., Davis, K.L., Amir el, A.D., Tadmor, M.D., Litvin, O., Fienberg, H.G., Jager, A., Zunder, E.R., *et al.* (2015). Data-Driven Phenotypic Dissection of AML Reveals Progenitor-like Cells that Correlate with Prognosis. *Cell* **162**, 184-197.
- Li, Z., Zhao, B., Wang, P., Chen, F., Dong, Z., Yang, H., Guan, K.L., and Xu, Y. (2010). Structural insights into the YAP and TEAD complex. *Genes Dev* **24**, 235-240.
- Liberali, P., Snijder, B., and Pelkmans, L. (2014). A hierarchical map of regulatory genetic interactions in membrane trafficking. *Cell* **157**, 1473-1487.

- Liberali, P., Snijder, B., and Pelkmans, L. (2015). Single-cell and multivariate approaches in genetic perturbation screens. *Nat Rev Genet* *16*, 18-32.
- Loomans, C.J.M., Williams Giuliani, N., Balak, J., Ringnalda, F., van Gurp, L., Huch, M., Boj, S.F., Sato, T., Kester, L., de Sousa Lopes, S.M.C., *et al.* (2018). Expansion of Adult Human Pancreatic Tissue Yields Organoids Harboring Progenitor Cells with Endocrine Differentiation Potential. *Stem Cell Reports* *10*, 712-724.
- Marshman, E., Booth, C., and Potten, C.S. (2002). The intestinal epithelial stem cell. *Bioessays* *24*, 91-98.
- Martinez-Ceballos, E., and Gudas, L.J. (2008). *Hoxa1* is required for the retinoic acid-induced differentiation of embryonic stem cells into neurons. *J Neurosci Res* *86*, 2809-2819.
- McCauley, H.A., and Wells, J.M. (2017). Pluripotent stem cell-derived organoids: using principles of developmental biology to grow human tissues in a dish. *Development* *144*, 958-962.
- McCracken, K.W., Cata, E.M., Crawford, C.M., Sinagoga, K.L., Schumacher, M., Rockich, B.E., Tsai, Y.H., Mayhew, C.N., Spence, J.R., Zavros, Y., *et al.* (2014). Modelling human development and disease in pluripotent stem-cell-derived gastric organoids. *Nature* *516*, 400-404.
- Meng, Z., Moroishi, T., and Guan, K.L. (2016). Mechanisms of Hippo pathway regulation. *Genes Dev* *30*, 1-17.
- Morgan, R.G., Mortenson, E., and Williams, A.C. (2018). Targeting LGR5 in Colorectal Cancer: therapeutic gold or too plastic? *Br J Cancer* *118*, 1410-1418.
- Mutoh, H., Satoh, K., Kita, H., Sakamoto, H., Hayakawa, H., Yamamoto, H., Isoda, N., Tamada, K., Ido, K., and Sugano, K. (2005). *Cdx2* specifies the differentiation of morphological as well as functional absorptive enterocytes of the small intestine. *Int J Dev Biol* *49*, 867-871.
- Nakano, T., Ando, S., Takata, N., Kawada, M., Muguruma, K., Sekiguchi, K., Saito, K., Yonemura, S., Eiraku, M., and Sasai, Y. (2012). Self-formation of optic cups and storable stratified neural retina from human ESCs. *Cell Stem Cell* *10*, 771-785.
- Olabi, S., Ucar, A., Brennan, K., and Streuli, C.H. (2018). Integrin-Rac signalling for mammary epithelial stem cell self-renewal. *Breast Cancer Res* *20*, 128.
- Orkin, R.W., Gehron, P., McGoodwin, E.B., Martin, G.R., Valentine, T., and Swarm, R. (1977). A murine tumor producing a matrix of basement membrane. *J Exp Med* *145*, 204-220.
- Pardo-Saganta, A., Law, B.M., Tata, P.R., Villoria, J., Saez, B., Mou, H., Zhao, R., and Rajagopal, J. (2015). Injury induces direct lineage segregation of functionally distinct airway basal stem/progenitor cell subpopulations. *Cell Stem Cell* *16*, 184-197.
- Pinto, D., Gregorieff, A., Begthel, H., and Clevers, H. (2003). Canonical Wnt signals are essential for homeostasis of the intestinal epithelium. *Genes Dev* *17*, 1709-1713.
- Plass, M., Solana, J., Wolf, F.A., Ayoub, S., Misios, A., Glazar, P., Obermayer, B., Theis, F.J., Kocks, C., and Rajewsky, N. (2018). Cell type atlas and lineage tree of a whole complex animal by single-cell transcriptomics. *Science* *360*.
- Qi, Z., Li, Y., Zhao, B., Xu, C., Liu, Y., Li, H., Zhang, B., Wang, X., Yang, X., Xie, W., *et al.* (2017). BMP restricts stemness of intestinal Lgr5(+) stem cells by directly suppressing their signature genes. *Nat Commun* *8*, 13824.
- Rheinwald, J.G., and Green, H. (1975). Serial cultivation of strains of human epidermal keratinocytes: the formation of keratinizing colonies from single cells. *Cell* *6*, 331-343.

- Rochel, N., and Moras, D. (2014). Architecture of DNA Bound RAR heterodimers. *Subcell Biochem* 70, 21-36.
- Rossi, G., Manfrin, A., and Lutolf, M.P. (2018). Progress and potential in organoid research. *Nat Rev Genet* 19, 671-687.
- Ruffner, H., Sprunger, J., Charlat, O., Leighton-Davies, J., Grosshans, B., Salathe, A., Zietzling, S., Beck, V., Therier, M., Isken, A., *et al.* (2012). R-Spondin potentiates Wnt/beta-catenin signaling through orphan receptors LGR4 and LGR5. *PLoS One* 7, e40976.
- Sachs, N., de Ligt, J., Kopper, O., Gogola, E., Bounova, G., Weeber, F., Balgobind, A.V., Wind, K., Gracanin, A., Begthel, H., *et al.* (2018). A Living Biobank of Breast Cancer Organoids Captures Disease Heterogeneity. *Cell* 172, 373-386 e310.
- Sakai, Y., Meno, C., Fujii, H., Nishino, J., Shiratori, H., Saijoh, Y., Rossant, J., and Hamada, H. (2001). The retinoic acid-inactivating enzyme CYP26 is essential for establishing an uneven distribution of retinoic acid along the antero-posterior axis within the mouse embryo. *Genes Dev* 15, 213-225.
- Sato, T., van Es, J.H., Snippert, H.J., Stange, D.E., Vries, R.G., van den Born, M., Barker, N., Shroyer, N.F., van de Wetering, M., and Clevers, H. (2011). Paneth cells constitute the niche for Lgr5 stem cells in intestinal crypts. *Nature* 469, 415-418.
- Sato, T., Vries, R.G., Snippert, H.J., van de Wetering, M., Barker, N., Stange, D.E., van Es, J.H., Abo, A., Kujala, P., Peters, P.J., *et al.* (2009). Single Lgr5 stem cells build crypt-villus structures in vitro without a mesenchymal niche. *Nature* 459, 262-265.
- Savory, J.G., Bouchard, N., Pierre, V., Rijli, F.M., De Repentigny, Y., Kothary, R., and Lohnes, D. (2009). Cdx2 regulation of posterior development through non-Hox targets. *Development* 136, 4099-4110.
- Schmitt, M., Schewe, M., Sacchetti, A., Feijtel, D., van de Geer, W.S., Teeuwssen, M., Sleddens, H.F., Joosten, R., van Royen, M.E., van de Werken, H.J.G., *et al.* (2018). Paneth Cells Respond to Inflammation and Contribute to Tissue Regeneration by Acquiring Stem-like Features through SCF/c-Kit Signaling. *Cell Rep* 24, 2312-2328 e2317.
- Schroeter, E.H., Kisslinger, J.A., and Kopan, R. (1998). Notch-1 signalling requires ligand-induced proteolytic release of intracellular domain. *Nature* 393, 382-386.
- Serra, D., Mayr, U., Boni, A., Lukonin, I., Rempfler, M., Challet Meylan, L., Stadler, M.B., Strnad, P., Papasaikas, P., Vischi, D., *et al.* (2019). Self-organization and symmetry breaking in intestinal organoid development. *Nature* 569, 66-72.
- Shen, J.P., Zhao, D., Sasik, R., Luebeck, J., Birmingham, A., Bojorquez-Gomez, A., Licon, K., Klepper, K., Pekin, D., Beckett, A.N., *et al.* (2017). Combinatorial CRISPR-Cas9 screens for de novo mapping of genetic interactions. *Nat Methods* 14, 573-576.
- Shimizu, H., Okamoto, R., Ito, G., Fujii, S., Nakata, T., Suzuki, K., Murano, T., Mizutani, T., Tsuchiya, K., Nakamura, T., *et al.* (2014). Distinct expression patterns of Notch ligands, Dll1 and Dll4, in normal and inflamed mice intestine. *PeerJ* 2, e370.
- Shirai, H., Mandai, M., Matsushita, K., Kuwahara, A., Yonemura, S., Nakano, T., Assawachananont, J., Kimura, T., Saito, K., Terasaki, H., *et al.* (2016). Transplantation of human embryonic stem cell-derived retinal tissue in two primate models of retinal degeneration. *Proc Natl Acad Sci U S A* 113, E81-90.

- Silberg, D.G., Swain, G.P., Suh, E.R., and Traber, P.G. (2000). Cdx1 and cdx2 expression during intestinal development. *Gastroenterology* *119*, 961-971.
- Simmini, S., Bialecka, M., Huch, M., Kester, L., van de Wetering, M., Sato, T., Beck, F., van Oudenaarden, A., Clevers, H., and Deschamps, J. (2014). Transformation of intestinal stem cells into gastric stem cells on loss of transcription factor Cdx2. *Nat Commun* *5*, 5728.
- Slemmons, K.K., Crose, L.E.S., Riedel, S., Sushnitha, M., Belyea, B., and Linardic, C.M. (2017). A Novel Notch-YAP Circuit Drives Stemness and Tumorigenesis in Embryonal Rhabdomyosarcoma. *Mol Cancer Res* *15*, 1777-1791.
- Snijder, B., Liberali, P., Frechin, M., Stoeger, T., and Pelkmans, L. (2013). Predicting functional gene interactions with the hierarchical interaction score. *Nat Methods* *10*, 1089-1092.
- Snippert, H.J., van der Flier, L.G., Sato, T., van Es, J.H., van den Born, M., Kroon-Veenboer, C., Barker, N., Klein, A.M., van Rheenen, J., Simons, B.D., *et al.* (2010). Intestinal crypt homeostasis results from neutral competition between symmetrically dividing Lgr5 stem cells. *Cell* *143*, 134-144.
- Spence, J.R., Mayhew, C.N., Rankin, S.A., Kuhar, M.F., Vallance, J.E., Tolle, K., Hoskins, E.E., Kalinichenko, V.V., Wells, S.I., Zorn, A.M., *et al.* (2011). Directed differentiation of human pluripotent stem cells into intestinal tissue in vitro. *Nature* *470*, 105-109.
- Spit, M., Koo, B.K., and Maurice, M.M. (2018). Tales from the crypt: intestinal niche signals in tissue renewal, plasticity and cancer. *Open Biol* *8*.
- Stringer, E.J., Duluc, I., Saandi, T., Davidson, I., Bialecka, M., Sato, T., Barker, N., Clevers, H., Pritchard, C.A., Winton, D.J., *et al.* (2012). Cdx2 determines the fate of postnatal intestinal endoderm. *Development* *139*, 465-474.
- Suzuki, K., Fukui, H., Kayahara, T., Sawada, M., Seno, H., Hiai, H., Kageyama, R., Okano, H., and Chiba, T. (2005). Hes1-deficient mice show precocious differentiation of Paneth cells in the small intestine. *Biochem Biophys Res Commun* *328*, 348-352.
- Tadokoro, T., Wang, Y., Barak, L.S., Bai, Y., Randell, S.H., and Hogan, B.L. (2014). IL-6/STAT3 promotes regeneration of airway ciliated cells from basal stem cells. *Proc Natl Acad Sci U S A* *111*, E3641-3649.
- Taguchi, A., Kaku, Y., Ohmori, T., Sharmin, S., Ogawa, M., Sasaki, H., and Nishinakamura, R. (2014). Redefining the in vivo origin of metanephric nephron progenitors enables generation of complex kidney structures from pluripotent stem cells. *Cell Stem Cell* *14*, 53-67.
- Takasato, M., Er, P.X., Becroft, M., Vanslambrouck, J.M., Stanley, E.G., Elefanty, A.G., and Little, M.H. (2014). Directing human embryonic stem cell differentiation towards a renal lineage generates a self-organizing kidney. *Nat Cell Biol* *16*, 118-126.
- Tetteh, P.W., Basak, O., Farin, H.F., Wiebrands, K., Kretzschmar, K., Begthel, H., van den Born, M., Korving, J., de Sauvage, F., van Es, J.H., *et al.* (2016). Replacement of Lost Lgr5-Positive Stem Cells through Plasticity of Their Enterocyte-Lineage Daughters. *Cell Stem Cell* *18*, 203-213.
- Tong, A.H., Lesage, G., Bader, G.D., Ding, H., Xu, H., Xin, X., Young, J., Berriz, G.F., Brost, R.L., Chang, M., *et al.* (2004). Global mapping of the yeast genetic interaction network. *Science* *303*, 808-813.
- Turner, D.A., Baillie-Johnson, P., and Martinez Arias, A. (2016). Organoids and the genetically encoded self-assembly of embryonic stem cells. *Bioessays* *38*, 181-191.

- van Es, J.H., Jay, P., Gregorieff, A., van Gijn, M.E., Jonkheer, S., Hatzis, P., Thiele, A., van den Born, M., Begthel, H., Brabletz, T., *et al.* (2005). Wnt signalling induces maturation of Paneth cells in intestinal crypts. *Nat Cell Biol* 7, 381-386.
- van Es, J.H., Sato, T., van de Wetering, M., Lyubimova, A., Yee Nee, A.N., Gregorieff, A., Sasaki, N., Zeinstra, L., van den Born, M., Korving, J., *et al.* (2012). Dll1+ secretory progenitor cells revert to stem cells upon crypt damage. *Nat Cell Biol* 14, 1099-1104.
- Wang, Y., Gunasekara, D.B., Reed, M.I., DiSalvo, M., Bultman, S.J., Sims, C.E., Magness, S.T., and Allbritton, N.L. (2017). A microengineered collagen scaffold for generating a polarized crypt-villus architecture of human small intestinal epithelium. *Biomaterials* 128, 44-55.
- Wolf, F.A., Hamey, F.K., Plass, M., Solana, J., Dahlin, J.S., Gottgens, B., Rajewsky, N., Simon, L., and Theis, F.J. (2019). PAGA: graph abstraction reconciles clustering with trajectory inference through a topology preserving map of single cells. *Genome Biol* 20, 59.
- Yui, S., Nakamura, T., Sato, T., Nemoto, Y., Mizutani, T., Zheng, X., Ichinose, S., Nagaishi, T., Okamoto, R., Tsuchiya, K., *et al.* (2012). Functional engraftment of colon epithelium expanded in vitro from a single adult Lgr5(+) stem cell. *Nat Med* 18, 618-623.

APPENDIX

Manuscript 1:

Regenerative landscape of intestinal organoids

Ilya Lukonin^{1,2}, Denise Serra^{1,2}, Katrin Volkmann¹, Janine Baaten³, Rui Zhao³, Shelly Meeusen³, Francisca Maurer¹, Michael B. Stadler^{1,4}, Jeremy Jenkins⁵, Prisca Liberali^{1,2}

¹Friedrich Miescher Institute for Biomedical Research (FMI), Maulbeerstrasse 66, 4058 Basel, Switzerland

²University of Basel. Petersplatz 1, 4001 Basel, Switzerland

³Genomics Institute of the Novartis Research Foundation, 10675 John Jay Hopkins Drive, San Diego, CA 92121, USA

⁴Swiss Institute of Bioinformatics, Maulbeerstrasse 66, 4058 Basel, Switzerland

⁵ Novartis Institutes for Biomedical Research Chemical Biology & Therapeutics (CBT), 181 Massachusetts Avenue, Cambridge, MA 02139, USA

Abstract

Development of intestinal organoids from single intestinal stem cells recapitulates the regenerative capacity of the intestinal epithelium. To unravel molecular mechanisms orchestrating organoid formation and regeneration of intestinal tissue, we developed a high-content image-based screening assay for an annotated compound library. We generated multivariate feature profiles for hundreds of thousands of individual organoids to quantitatively describe the phenotypic landscape of organoid development. The resulting phenotypic fingerprints were then used to infer regulatory genetic interactions from a single screen, establishing a novel paradigm in genetic interaction screening applied to an emergent system. This allowed the identification of modules of genes that regulate cell identity transitions and maintain the balance between regeneration and homeostasis, unraveling novel roles for several pathways, among them retinoic acid signaling. We then characterized a crucial role for retinoic acid nuclear receptors in controlling the exit from the regenerative state and in driving enterocyte differentiation. By combining quantitative imaging with RNA sequencing we confirmed the role of endogenous retinoic acid signaling and metabolism for initiating transcriptional programs that guide intestinal epithelium cell fate transitions and identified a small molecule inhibitor of retinoid X receptor, RXR, that improved intestinal regeneration *in vivo*.

The intestinal epithelium consists of a single layer of polarized cells arranged into regular spatially distinct structures named villi that contain differentiated cells with the most abundant being absorptive enterocytes. The villi are interspaced by crypts where the Leucine-rich repeat-containing G-protein coupled receptor 5 (Lgr5)-positive stem cells and secretory Paneth cells reside^{1,2}. At the crypt periphery cells gain transit amplifying (TA) identity and divide rapidly before migrating upward the villus³ and undergoing terminal differentiation⁴. Coordinated spatial organization of cell fate transitions along the crypt-villus axis results in a stereotypic patterned distribution of cell types whereas the conveyor belt-like replacement of lost cells facilitates cell turnover⁵. These features allow the intestinal epithelium to be the most rapidly renewing tissue in the human body⁶ with the entire tissue being replaced at a rate of 4-5 days. Recent studies have revealed the broad plasticity of intestinal epithelial cells⁷ that allows them to dedifferentiate and replenish the pool of cycling cells lost upon damage^{8,9}. After the crypt compartment has been regenerated, the same pattern re-emerges and homeostasis is restored through coordinated action of signaling pathways such as Hippo¹⁰, Wnt, BMP¹¹, Notch¹¹, and others¹². However, it remains poorly understood, how the spatial organization is regulated and coordinated, especially in the adult intestine after regeneration.

Intestinal organoids are an *ex vivo* culture system of the intestinal epithelium that recapitulates numerous important aspects of the parent tissue: cell type diversity, spatial organization, but also the ability to regenerate and return to homeostatic conditions following damage^{2,13,14}. In fact, an entire intestinal organoid can develop from a single cell forming an emergent, self-organized structure undergoing spatially and temporally controlled cell fate transitions^{14,15}. In the first step, single cells form a symmetric cyst-like structure in which all cells reside in a Yap-dependent regenerative state and lack expression of genes characteristic for intestinal cell types¹⁴. Subsequently this symmetry is broken, resulting first in the formation of secretory Paneth cells that define and maintain the crypt², and then the differentiation of absorptive enterocytes that emerge and continue to reside distal from the crypt¹⁵. Thus, the resulting spatial distribution of cell types in organoids mimics the organization along the crypt-villus axis and development of intestinal organoids from a single cell recapitulates the regeneration of the intestinal epithelium and the re-establishment of homeostasis^{16,17}.

Here we developed an image-based phenotypic screening platform in intestinal organoids cultured from single cells to characterize the phenotypic landscape of organoid development and describe a tool box of compounds that direct the phenotypic outcome. The newly identified tool compounds were used to infer functional genetic interactions and identify pathways impacting different steps of organoid development. We then focused on conditions that improve the regeneration potential of the intestinal epithelium and discovered a role for nuclear retinoic acid receptors and retinol metabolism in intestinal damage response and homeostasis both *in vitro* and *in vivo*. Taken together, our study establishes a novel paradigm for genetic interaction screening applied to an emergent self-organized system that we used to identify a small molecule that improved the regeneration of the intestinal epithelium.

Phenotypic landscape of intestinal organoids development

To systematically identify the molecular mechanisms underlying the organoid development we devised an image-based screen with a chemical genetics approach. Intestinal organoids were generated from single cells over the course of four days in continuous presence of a chemical library consisting of 2789 selected tool compounds annotated with 895 unique primary targets (**Fig. 1a, Supplementary Table 1**). Resulting organoids were stained for markers of enterocytes (Aldolase B^{18,19}) and Paneth cells (Lysozyme²⁰), DNA (DAPI) and total protein content (CellTrace) and imaged with a high throughput spinning disk confocal microscope (ca. 10^7 images, **Fig. 1a, b and Extended Data Fig. 1a**). Segmentation and feature extraction yielded a multivariate feature set profiling ~450,000 individual organoids that had high technical reproducibility between replicates in number and size (**Extended Data Fig. 1b**) and no detectable plate effects (**Extended Data Fig. 1c**). Using feature selection we defined a set of features (**Fig. 1b and Extended Data Fig. 1h**) that showed reproducible, significant and condition-specific perturbation effects in active control conditions, γ -secretase inhibitor DAPT²¹ and GSK3 β inhibitor CHIR99021²² (**Extended Data Fig. 1d, e, f**).

Given the complex nature of organoid phenotypes that cannot be reduced to a single readout (**Extended Data Fig. 1g**) we used the position of individual organoids in feature space to cluster them by phenotypic similarity²³ (**Fig. 1c**). Every organoid was unambiguously assigned to one of the identified 15 phenotypic classes that in turn represented different grades of severity of 7 major organoid phenotypes (**Fig. 1d**). The most frequently observed phenotype was that of mature organoids (the “wild-type” phenotype) with both differentiated cell types spatially distributed along the crypt-villus axis (classes 1-3, further referred to as *mature organoids*). Other phenotypes included *Paneth cell hyperplasia* (classes 5 to 7), *Wnt hyperactivation phenotype* featuring expanded crypt region (classes 8 and 9), perturbed abundance and spatial distribution of cell types (class 10, further referred to as *progenitor-reduced*), organoids consisting only of enterocytes (classes 14 and 15, further referred to as *enterocysts*) and organoids lacking both differentiated cell types (classes 11-13) (**Fig. 1d**). This latter phenotype is reminiscent of the YAP1 overexpression and regenerative state phenotype¹⁴ and therefore further referred to as *regenerative*.

For every compound in the library we described the relative enrichment or depletion of each phenotypic class (**Fig. 1e**), generating an individual characteristic phenotypic fingerprint. In active control conditions we observed the phenotypes previously reported for these perturbations, such as a *Wnt hyperactivation* phenotype for CHIR99021. Phenotypic fingerprints together with their correlation between replicates (above 0.9 for active controls, **Extended Data Fig. 2a**) were then used to identify hits from the screen, revealing 342 compounds with significant and reproducible phenotypes of which 334 were annotated with a primary human target gene (**Fig. 1f, Extended Data Fig. 3a, Supplementary Table 1**) and corresponded to 230 unique target gene-modality pairs (target activator or target inhibitor, **Extended Data Fig. 3b**). From these, 39 genes were targeted by two or more compounds with different chemistry but highly similar phenotypic fingerprints (**Fig. 1f**) and 35 were strongly enriched over the initial library (**Extended Data Fig. 3c, d, Supplementary Table 1**). These formed a network significantly enriched for reported STRING interactions (**Extended Data Fig. 3e**). Functional annotations enriched in this network included both pathways implicated in intestinal organoid development and homeostasis (Wnt, Notch and

TGF beta signaling) but also pathways that have not been associated with it before, such as nuclear receptor signaling. We furthermore found phenotype-specific annotation enrichments, e.g. the PI3K-Akt-mTOR pathway for the *enterocyst* and MAP kinase pathway for the *regenerative* phenotypes. Our screen therefore recovered known regulators of intestinal development and regeneration described by their phenotypic fingerprints, and provides a high-quality resource for mapping novel interactions directly from the multivariate phenotypic readouts.

Mapping functional interactions that govern organoid development

One classical approach to map functional genetic interactions are double gene knockout screens²⁴, however, such an approach historically reads out colony fitness. While applied with great success to mammalian cell lines through transduction of pooled libraries^{25,26}, it is impractical for arrayed phenotypic screens due to an exponential increase in pairwise combinations. A recently developed statistical method, the hierarchical interaction score (HIS), enables inference of functional interactions from multivariate readouts and the identification of hierarchical nested relationships for pairs of conditions²⁷⁻³⁰ (**Fig. 2a**). Using the HIS on the phenotypic fingerprints we identified ~7500 HIS interactions (**Fig. 2b, Extended Data Fig. 4a**) that were enriched in STRING interactions and contained a high percentage of gene pairs co-annotated with KEGG and GO terms (**Extended Data Fig. 4b, c**). We then determined an optimal threshold of HIS value corresponding to the highest enrichment of co-annotated terms (GO: ca. 46%, KEGG: ca. 22%) and reported STRING interactions (ca. 2.8 fold enrichment) **Extended Data Fig. 4b, d**. The interactions retained at this HIS threshold were used to create the first map of functional genetic interactions underlying the development of intestinal organoids (**Fig. 2c**). In the resulting network we found phenotype-specific annotation enrichments, for example enrichment in genes involved in cell cycle regulation, phosphatidylinositol and AMPK signaling for the *enterocyst* phenotype, while genes involved in colorectal cancer, Ras and Wnt signaling were enriched for the *regenerative* phenotype (**Fig. 2c**).

In the generated network a subset of nodes had more outgoing than incoming edges suggesting these to be upstream regulators and potential key players of organoid development (**Fig. 2a, c**). These included β -Catenin (CTNNB1), which, when destabilized, resulted in a pleiotropic phenotypic fingerprint (**Extended Data Fig. 4e and f**), consistent with the crucial role of canonical Wnt signaling in organoid development^{31,32}. In addition, the network connectivity was not evenly distributed (**Fig. 2b, Extended Data Fig. 4a**) with 6 highly interconnected clusters (**Fig. 2c**) showing cluster-specific phenotypic fingerprints and functional annotation enrichments. For example, conditions perturbing AMPK-signaling genes resulted in a less severe *enterocyst* phenotype, whereas targeting cell cycle associated genes produced a more severe phenotypic outcome. Similarly, conditions perturbing the actin cytoskeleton resulted in an enrichment of a less severe *regenerative* phenotype compared to its enrichment when targeting genes annotated with PPAR signaling and transcriptional misregulation in cancer. We therefore conclude that quantitative multivariate fingerprints capture the phenotypic landscape of organoid development and allow inference of functional genetic interactions from a single arrayed screen.

Retinol metabolism, through RXR and RAR activity, controls exit from regenerative state and differentiation to enterocytes

We focused our attention on a subnetwork with an increase in severe *regenerative* phenotype abundance that included compounds targeting retinoid X receptor alpha (RXRa) and retinoic acid nuclear receptor (RARa) observing the highest phenotypic penetrance for an RXRa antagonist (Cpd2170^{33,34}, further referred to as RXRi, **Extended Data Fig. 4g** and **Supplementary Table 1**). RXR and RAR form nuclear receptor heterodimers³⁵, that in ligand-unbound state occupy retinoic acid response elements (RAREs) on chromatin repressing the expression of target genes. Binding of a vitamin A metabolite, all-trans retinoic acid (atRA) to RAR induces recruitment of transcriptional coactivators and target gene de-repression³⁶ which can be modulated by agonists and antagonists in an orthogonal manner. We validated the primary screen phenotypes by showing that treatment with RXRi induced a near-complete absence of enterocytes, whereas organoids cultured in the presence of an RXR agonist (NRX 194204), atRA or 9-cis retinoic acid (9cis-RA), individually and in combination, exhibited increased enterocyte differentiation (**Fig. 3a**). Interestingly, the differentiation defect observed in RXRi condition could not be rescued by concomitant atRA stimulation (**Fig. 3a, Extended Data Fig. 5a, b**) hinting at the importance of RXR activation state. Also when treated at a later time point, RXRi-treated organoids had increased size and lacked enterocytes, with an inverse phenotype observed for RXR agonist treatment (increase in enterocyte fraction, **Fig. 3b**). The reduction in enterocyte differentiation caused by RXRi was accompanied by an increase in SOX9⁺ and ki67⁺ cycling cells no longer confined to the crypt (**Extended Data Fig. 5c, d, e**) with an opposite phenotype observed in RXR agonist- and retinoid-treated organoids (**Extended Data Fig. 5c, d, e**).

To investigate how endogenous RA signaling activity is controlled in the intestine, we looked at metabolism of the atRA precursor, vitamin A (retinol). Intestinal cells absorb³⁷, process and secrete vitamin A into the lymph system³⁸, but can also metabolize it to atRA³⁹ (**Fig. 3c**). Interestingly, we found that genes involved in RA metabolism are specifically expressed in enterocytes^{40,41}, in particular ALDH1A1 (**Extended Data Fig. 6b**). This enzyme mediates the rate-limiting step in atRA production⁴², indicating that enterocytes are potentially able to maintain higher intracellular atRA levels compared to the crypt cells. Indeed, ALDH1A1 abundance in enterocytes (**Fig. 3d, Extended Data Fig. 5f**) translated into productive upregulation of RARE motif-containing reporter gene (**Fig. 3e** and **Extended Data Fig. 5g**) and retinoid treatment resulted in an expansion of the Aldolase B/RARE-dsGFP – double positive region (**Extended Data Fig. 5g**). Also *in vivo* RA signaling activity was enriched in the villi region of the adult intestine as visualized in RARE-LacZ transgene mice (**Extended Data Fig. 5h**). Consistently, organoids cultured in Vitamin A-depleted medium displayed reduced enterocyte numbers accompanied by an increase in cycling cells extending further away from the crypt with both effects reversed by exogenous atRA (**Fig. 3f, g** and **Extended Data Fig. 5i**). A similar phenotype was observed with ALDH1A1 inhibition, independently from the presence of Vitamin A in the medium (**Fig. 3f, g**). This data shows that retinoic acid metabolism is necessary for enterocyte differentiation and obtains regional specificity through ALDH1A1-controlled intracellular atRA synthesis.

To then understand if the RXR α -induced proliferative and undifferentiated phenotype is related to the Yap-dependent regenerative state^{14,43,44}, we looked at YAP1 subcellular localization. We observed that organoids treated with RXR α retained pronounced nuclear localization of YAP1 (**Fig. 3h**), and were actively cycling (**Fig. 3i**) even after withdrawal of exogenous Wnt. We therefore hypothesized that RXR α “locks” the cells in a Yap-dependent regenerative state and that RXR activity is necessary for exit from this state.

RXR antagonist treatment imposes a regenerative state and suppresses intestinal identity

To understand how RA signaling drives enterocyte differentiation, we determined the transcriptional dynamics of predicted RXR/RAR target genes during organoid development. This revealed enrichment of RXR and RAR homo- and heterodimer motifs in proximity of promoters of genes induced from day 3 onwards (**Fig. 4a, Extended Data Fig. 7a and b, c**). These genes were predominantly regulators of fatty acid degradation, PPAR and Notch signaling, and genes associated with enterocyte functions (**Extended Data Fig. 7d**). We then confirmed which genes responded to RA using RNA sequencing in RXR α - and retinoid- treated organoids (**Fig. 4b, Extended Data Fig. 7e**). We observed that retinoids induced a transcriptional response with increased expression of enterocyte-specific genes (**Extended Data Fig. 7f**) while the transcriptional profile of RXR α -treated organoids at day 4 resembled control undifferentiated organoids at day 1-3, suggesting suppressed differentiation and arrested Yap-dependent regenerative state (**Fig. 4c**). Genes specifically upregulated in retinoid stimulation conditions at earlier (6 hour) time point and downregulated by RXR α (1336 genes, **Extended Data Fig. 7g, h**) were enriched for functional annotations such as RNA processing, splicing and ribosome activity. At 24 hours, genes upregulated in retinoid-treated organoids and downregulated in RXR α were enriched for functional annotations associated with enterocyte function (2586 genes, **Fig. 4d**). Together with the transcription factor binding motif analysis (**Extended Data Fig. 7d**) this shows an involvement of retinoic acid signaling in enterocyte differentiation.

To characterize the cell state induced by absence of RA signaling, we first clustered genes by differential expression between treatment conditions. This revealed that genes upregulated in retinoic acid stimulated organoids were downregulated in RXR α and enriched for RARE motifs, while genes upregulated in RXR α were downregulated in retinoid treatment and depleted of RARE motifs (**Fig. 4e-f, Extended Data Fig. 8a, b, c, Supplementary Table 2**). Because transition to a regenerative state is accompanied by both increased expression of fetal-like genes and reduced expression of genes characteristic for adult tissue⁴³, we initially analyzed genes that were specifically expressed in different tissues of the gastrointestinal (GI) tract¹⁹. We observed that both early stages of organoid development and RXR α -treated organoids express genes specific for more anterior GI tract tissues and repress the expression of intestine-specific genes (**Extended Data Fig. 8d and e**). RXR α -treated organoids also lacked the canonical intestinal stem cell signature⁴⁰ (**Extended Data Fig. 8f**), consistently showing that compromised RXR-mediated signaling not only suppresses differentiation to enterocytes but also hinders the ability of organoids to acquire intestinal identity. To understand whether RXR α -treated organoids also undergo a transition to a fetal-like state, we analyzed the expression of genes comprising the fetal-like regenerative signature⁴³, observing an upregulation in RXR α -treated organoids (**Fig. 4g**). Moreover, the RXR α -induced regenerative state is similar in its transcriptional changes to the helminth infection-induced fetal-like reversion of intestinal

cells⁴⁵ whereby genes depleted of RXR/RAR motifs were the most strongly upregulated, and genes enriched for RXR/RAR motifs showed the strongest downregulation (**Fig. 4h and Extended Data Fig. 8g**). To conclude, the RXRi-induced regenerative state is characterized by a lack of intestinal identity, manifesting in reduced expression of genes specific to the small intestine and the upregulation of genes associated with fetal-like state. This suggests RXR antagonists as potential treatments to promote intestinal epithelium regeneration.

RXR antagonist treatment improves regeneration ensuing irradiation-induced damage *in vivo*

To validate the regeneration-promoting effect of RXRi treatment, we devised an *in vivo* study using an irradiation-induced colitis model in which the small intestine of mice was irradiated with 20Gy to ablate cycling cells (**Fig. 5a**). Subsequently, mice were left to recover for 6 days and pulsed with RXRi twice, at day 1 and day 3 after irradiation. At the cellular level, loss of the cycling cells resulted in shorter villi and an acute loss of barrier function (**Extended Data Fig. 9e**), and, ultimately, weight loss due to compromised intestinal function. RXRi treatment significantly improved regeneration of the intestine resulting in reduced weight loss (**Fig. 5b, Extended Data Fig. 9c, d**) and lower amount of blood in the stool (**Fig. 5c, Extended Data Fig. 9g**). At the tissue level, in irradiated mice, RXRi treatment resulted in less decellularization (**Fig. 5d**) and regeneration of longer functional villi containing mature goblet cells (**Fig. 5e**). This validates the regenerative phenotype observed in the organoid system *in vivo*, showing that transient inhibition of RXR-mediated signaling can be used to improve regeneration of the intestinal epithelium. RXRi-treated mice recovered better from irradiation-induced damage and developed functional villi, making RXR antagonists a potential therapeutic agent to improve regeneration of the intestinal epithelium after acute damage.

Discussion

In this study we established an image-based screening platform and developed multivariate phenotypic fingerprinting to characterize the phenotypic landscape of organoid development and to generate the first map of functional genetic interactions governing intestinal organoid development and self-organization. With network analysis we show that our workflow can both predict known and infer novel functional genetic interactions from a single screen. Using our approach, we establish a critical role for nuclear retinoic acid receptors as regulators of regenerative properties of the intestinal tissue. We describe the role of RA signaling and metabolism in cell type transitions and show that early RXR inhibition forces organoids to reside in a Yap-dependent regenerative state^{14,46}, maintaining an active cell cycle and failing to undergo differentiation to any of the intestinal cell types. We propose that endogenous RA signaling, therefore, safeguards the exit from regenerative state shaping the cell type composition of the organoid and ensuring return to homeostasis.

We show that in intestinal organoids under homeostatic conditions, RA signaling is controlled in enterocytes through ALDH1A1-dependent metabolic flux, maintaining cell type balance between enterocytes and undifferentiated progenitors. Interestingly, also in the context of a colitis-induced colonic tumor model the tumorigenesis potential arises from altered retinoic acid metabolism⁴⁷ indicating that cells with compromised RA metabolism are more likely to remain in an undifferentiated and proliferative state. In intestinal homeostasis, a number of downstream effects of RA signaling have been proposed, including transcriptional induction of HOXA5 and downstream negative regulators of the cell cycle³⁶. However, the downstream effectors and resulting transcriptional changes were not clear. Here we reveal that early response to retinoic acid stimulation induces the upregulation of gene regulatory programs necessary for starting differentiation, resulting in the subsequent upregulation of genes involved in enterocyte function. Moreover, we show that the regenerative state induced by RXR inhibition is characterized both by the loss of expression of intestine-specific transcriptional program and by an increase in expression of fetal-like genes. We therefore propose a model in which endogenous RXR activation is required for initiating transition to intestinal identity and is indispensable for return to homeostasis ensuing regeneration in the intestinal organoid system.

Finally, we demonstrated the regenerative potential of a transient RXR antagonist treatment *in vivo*. This could be explored further in the future combining the inhibitor treatment with different diets such as fasting⁴⁸ or calorie restriction⁴⁹ to promote regeneration of functional epithelium after acute damage. Another promising future direction could be reduction of dietary Vitamin A or targeting retinol-specific importer Stra6 as a strategy to modulate the regenerative potential during recovery. In summary, this work illustrates how a multivariate phenotypic screening approach in an emergent organoid system can be used to identify physiologically relevant targets that can ultimately be translated *in vivo* unravelling the mechanisms controlling the regenerative potential of intestinal epithelium.

Acknowledgements

We thank L. Challet Meylan for support in organoid culture, D. Vischi, S. Iftikhar and E. Tagliavini for IT support, L. Gelman for assistance and training, H. Kohler for sorting, S. Smallwood for sequencing, L. Pelkmans, M. Lutolf, J. Betschinger, C. Tsiairis, S. Gasser and laboratory members for reading the manuscript. Funding: SNSF (POOP3_157531 to P.L.). This work received funding from the ERC under the European Union's Horizon 2020 research and innovation programme (grant agreement no. 758617).

Author contributions

P.L. conceived and supervised the study, P.L. and I.L. designed the experiments, J.J. designed the annotated compound library, I.L. and K.V. performed the image-based screen, I.L. performed the image analysis, F.M. performed lentivirus production and organoid preparations, I.L. performed the imaging and transcriptomics experiments, M.B.S. designed transcription factor motifs analysis, I.L., D.S. and M.B.S. performed the analysis of RNA-seq data, J.B., R.Z. and S.M. designed, performed and analyzed the mouse irradiation study, P.L. and I.L. wrote the paper.

References

- 1 Garabedian, E. M., Roberts, L. J., McNevin, M. S. & Gordon, J. I. Examining the role of Paneth cells in the small intestine by lineage ablation in transgenic mice. *J Biol Chem* **272**, 23729-23740 (1997).
- 2 Sato, T. *et al.* Paneth cells constitute the niche for Lgr5 stem cells in intestinal crypts. *Nature* **469**, 415-418, doi:10.1038/nature09637 (2011).
- 3 Marshman, E., Booth, C. & Potten, C. S. The intestinal epithelial stem cell. *Bioessays* **24**, 91-98, doi:10.1002/bies.10028 (2002).
- 4 Bullen, T. F. *et al.* Characterization of epithelial cell shedding from human small intestine. *Lab Invest* **86**, 1052-1063, doi:10.1038/labinvest.3700464 (2006).
- 5 Bjerknes, M. & Cheng, H. Clonal analysis of mouse intestinal epithelial progenitors. *Gastroenterology* **116**, 7-14 (1999).
- 6 Heath, J. P. Epithelial cell migration in the intestine. *Cell Biol Int* **20**, 139-146, doi:10.1006/cbir.1996.0018 (1996).
- 7 Wells, J. M. & Watt, F. M. Diverse mechanisms for endogenous regeneration and repair in mammalian organs. *Nature* **557**, 322-328, doi:10.1038/s41586-018-0073-7 (2018).
- 8 Tetteh, P. W. *et al.* Replacement of Lost Lgr5-Positive Stem Cells through Plasticity of Their Enterocyte-Lineage Daughters. *Cell Stem Cell* **18**, 203-213, doi:10.1016/j.stem.2016.01.001 (2016).
- 9 van Es, J. H. *et al.* Dll1+ secretory progenitor cells revert to stem cells upon crypt damage. *Nat Cell Biol* **14**, 1099-1104, doi:10.1038/ncb2581 (2012).
- 10 Gregorieff, A. & Wrana, J. L. Multiple roles for the hippo effector yap in gut regeneration and cancer initiation. *Mol Cell Oncol* **3**, e1143992, doi:10.1080/23723556.2016.1143992 (2016).
- 11 Tian, H. *et al.* Opposing activities of Notch and Wnt signaling regulate intestinal stem cells and gut homeostasis. *Cell Rep* **11**, 33-42, doi:10.1016/j.celrep.2015.03.007 (2015).
- 12 Joosten, S. P. J. *et al.* MET Signaling Mediates Intestinal Crypt-Villus Development, Regeneration, and Adenoma Formation and Is Promoted by Stem Cell CD44 Isoforms. *Gastroenterology* **153**, 1040-1053 e1044, doi:10.1053/j.gastro.2017.07.008 (2017).
- 13 Grun, D. *et al.* Single-cell messenger RNA sequencing reveals rare intestinal cell types. *Nature* **525**, 251-255, doi:10.1038/nature14966 (2015).
- 14 Serra, D. *et al.* Self-organization and symmetry breaking in intestinal organoid development. *Nature* **569**, 66-72, doi:10.1038/s41586-019-1146-y (2019).
- 15 Sato, T. *et al.* Single Lgr5 stem cells build crypt-villus structures in vitro without a mesenchymal niche. *Nature* **459**, 262-265, doi:10.1038/nature07935 (2009).
- 16 Chacon-Martinez, C. A., Koester, J. & Wickstrom, S. A. Signaling in the stem cell niche: regulating cell fate, function and plasticity. *Development* **145**, doi:10.1242/dev.165399 (2018).
- 17 Qi, Z. *et al.* BMP restricts stemness of intestinal Lgr5(+) stem cells by directly suppressing their signature genes. *Nat Commun* **8**, 13824, doi:10.1038/ncomms13824 (2017).
- 18 Chang, J. *et al.* Proteomic changes during intestinal cell maturation in vivo. *J Proteomics* **71**, 530-546, doi:10.1016/j.jprot.2008.08.003 (2008).
- 19 Carithers, L. J. *et al.* A Novel Approach to High-Quality Postmortem Tissue Procurement: The GTEx Project. *Biopreserv Biobank* **13**, 311-319, doi:10.1089/bio.2015.0032 (2015).
- 20 Peeters, T. & Vantrappen, G. The Paneth cell: a source of intestinal lysozyme. *Gut* **16**, 553-558 (1975).

- 21 VanDussen, K. L. *et al.* Notch signaling modulates proliferation and differentiation of intestinal crypt base columnar stem cells. *Development* **139**, 488-497, doi:10.1242/dev.070763 (2012).
- 22 Yin, X. *et al.* Niche-independent high-purity cultures of Lgr5+ intestinal stem cells and their progeny. *Nat Methods* **11**, 106-112, doi:10.1038/nmeth.2737 (2014).
- 23 Levine, J. H. *et al.* Data-Driven Phenotypic Dissection of AML Reveals Progenitor-like Cells that Correlate with Prognosis. *Cell* **162**, 184-197, doi:10.1016/j.cell.2015.05.047 (2015).
- 24 Tong, A. H. *et al.* Global mapping of the yeast genetic interaction network. *Science* **303**, 808-813, doi:10.1126/science.1091317 (2004).
- 25 Shen, J. P. *et al.* Combinatorial CRISPR-Cas9 screens for de novo mapping of genetic interactions. *Nat Methods* **14**, 573-576, doi:10.1038/nmeth.4225 (2017).
- 26 Park, R. J. *et al.* A genome-wide CRISPR screen identifies a restricted set of HIV host dependency factors. *Nat Genet* **49**, 193-203, doi:10.1038/ng.3741 (2017).
- 27 Snijder, B., Liberali, P., Frechin, M., Stoeger, T. & Pelkmans, L. Predicting functional gene interactions with the hierarchical interaction score. *Nat Methods* **10**, 1089-1092, doi:10.1038/nmeth.2655 (2013).
- 28 Liberali, P., Snijder, B. & Pelkmans, L. A hierarchical map of regulatory genetic interactions in membrane trafficking. *Cell* **157**, 1473-1487, doi:10.1016/j.cell.2014.04.029 (2014).
- 29 Liberali, P., Snijder, B. & Pelkmans, L. Single-cell and multivariate approaches in genetic perturbation screens. *Nat Rev Genet* **16**, 18-32, doi:10.1038/nrg3768 (2015).
- 30 Berchtold, D., Battich, N. & Pelkmans, L. A Systems-Level Study Reveals Regulators of Membrane-less Organelles in Human Cells. *Mol Cell* **72**, 1035-1049 e1035, doi:10.1016/j.molcel.2018.10.036 (2018).
- 31 Andreu, P. *et al.* A genetic study of the role of the Wnt/beta-catenin signalling in Paneth cell differentiation. *Dev Biol* **324**, 288-296, doi:10.1016/j.ydbio.2008.09.027 (2008).
- 32 Pinto, D., Gregorieff, A., Begthel, H. & Clevers, H. Canonical Wnt signals are essential for homeostasis of the intestinal epithelium. *Genes Dev* **17**, 1709-1713, doi:10.1101/gad.267103 (2003).
- 33 Ebisawa, M. *et al.* Retinoid X receptor-antagonistic diazepinylbenzoic acids. *Chem Pharm Bull (Tokyo)* **47**, 1778-1786 (1999).
- 34 Sakaki, J. *et al.* Synthesis and structure-activity relationship of novel RXR antagonists: orally active anti-diabetic and anti-obesity agents. *Bioorg Med Chem Lett* **17**, 4804-4807, doi:10.1016/j.bmcl.2007.06.080 (2007).
- 35 Evans, R. M. & Mangelsdorf, D. J. Nuclear Receptors, RXR, and the Big Bang. *Cell* **157**, 255-266, doi:10.1016/j.cell.2014.03.012 (2014).
- 36 Ordonez-Moran, P., Dafflon, C., Imajo, M., Nishida, E. & Huelsken, J. HOXA5 Counteracts Stem Cell Traits by Inhibiting Wnt Signaling in Colorectal Cancer. *Cancer Cell* **28**, 815-829, doi:10.1016/j.ccell.2015.11.001 (2015).
- 37 Borel, P. *et al.* Processing of vitamin A and E in the human gastrointestinal tract. *Am J Physiol Gastrointest Liver Physiol* **280**, G95-G103, doi:10.1152/ajpgi.2001.280.1.G95 (2001).
- 38 Nayak, N., Harrison, E. H. & Hussain, M. M. Retinyl ester secretion by intestinal cells: a specific and regulated process dependent on assembly and secretion of chylomicrons. *J Lipid Res* **42**, 272-280 (2001).
- 39 Lampen, A., Meyer, S., Arnhold, T. & Nau, H. Metabolism of vitamin A and its active metabolite all-trans-retinoic acid in small intestinal enterocytes. *J Pharmacol Exp Ther* **295**, 979-985 (2000).
- 40 Haber, A. L. *et al.* A single-cell survey of the small intestinal epithelium. *Nature* **551**, 333-339, doi:10.1038/nature24489 (2017).

- 41 Goverse, G. *et al.* Diet-Derived Short Chain Fatty Acids Stimulate Intestinal Epithelial Cells To Induce Mucosal Tolerogenic Dendritic Cells. *J Immunol* **198**, 2172-2181, doi:10.4049/jimmunol.1600165 (2017).
- 42 Molotkov, A. & Duester, G. Genetic evidence that retinaldehyde dehydrogenase Raldh1 (Aldh1a1) functions downstream of alcohol dehydrogenase Adh1 in metabolism of retinol to retinoic acid. *J Biol Chem* **278**, 36085-36090, doi:10.1074/jbc.M303709200 (2003).
- 43 Yui, S. *et al.* YAP/TAZ-Dependent Reprogramming of Colonic Epithelium Links ECM Remodeling to Tissue Regeneration. *Cell Stem Cell* **22**, 35-49 e37, doi:10.1016/j.stem.2017.11.001 (2018).
- 44 Gregorieff, A., Liu, Y., Inanlou, M. R., Khomchuk, Y. & Wrana, J. L. Yap-dependent reprogramming of Lgr5+ stem cells drives intestinal regeneration and cancer. *Nature*, 1-16, doi:10.1038/nature15382 (2015).
- 45 Nusse, Y. M. *et al.* Parasitic helminths induce fetal-like reversion in the intestinal stem cell niche. *Nature* **559**, 109-113, doi:10.1038/s41586-018-0257-1 (2018).
- 46 Kim, T. H. & Shivasani, R. A. Genetic evidence that intestinal Notch functions vary regionally and operate through a common mechanism of Math1 repression. *J Biol Chem* **286**, 11427-11433, doi:10.1074/jbc.M110.188797 (2011).
- 47 Bhattacharya, N. *et al.* Normalizing Microbiota-Induced Retinoic Acid Deficiency Stimulates Protective CD8(+) T Cell-Mediated Immunity in Colorectal Cancer. *Immunity* **45**, 641-655, doi:10.1016/j.immuni.2016.08.008 (2016).
- 48 Rangan, P. *et al.* Fasting-Mimicking Diet Modulates Microbiota and Promotes Intestinal Regeneration to Reduce Inflammatory Bowel Disease Pathology. *Cell Rep* **26**, 2704-2719 e2706, doi:10.1016/j.celrep.2019.02.019 (2019).
- 49 Yousefi, M. *et al.* Calorie Restriction Governs Intestinal Epithelial Regeneration through Cell-Autonomous Regulation of mTORC1 in Reserve Stem Cells. *Stem Cell Reports* **10**, 703-711, doi:10.1016/j.stemcr.2018.01.026 (2018).

Figures 1-5

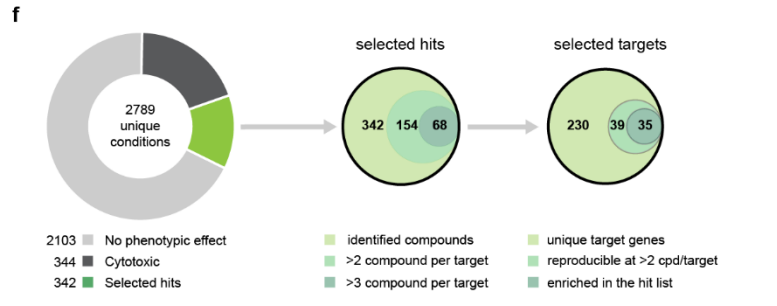
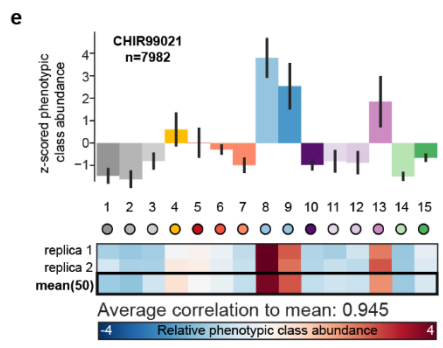
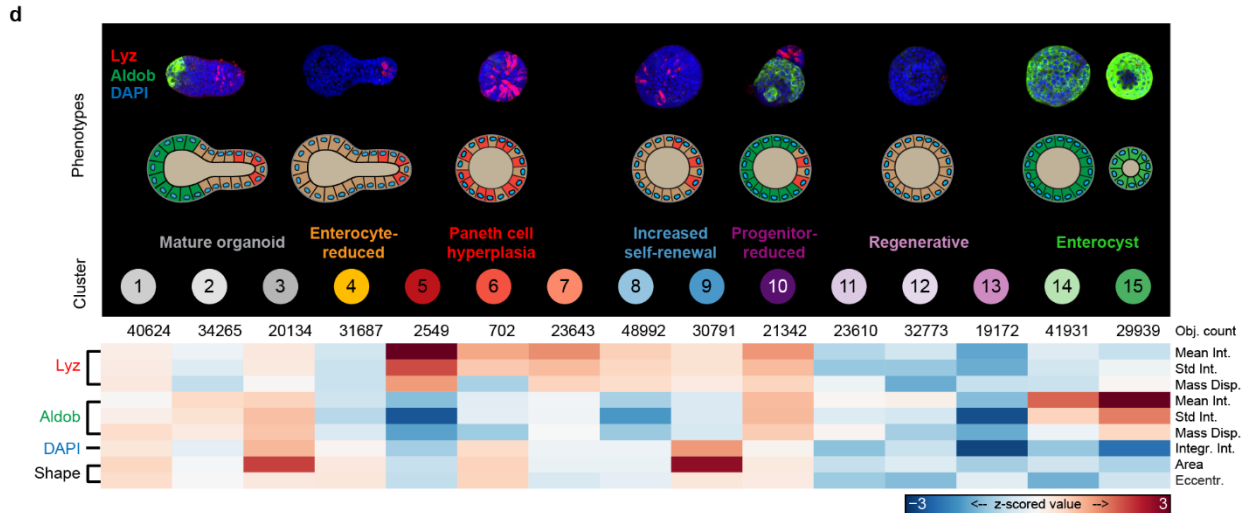
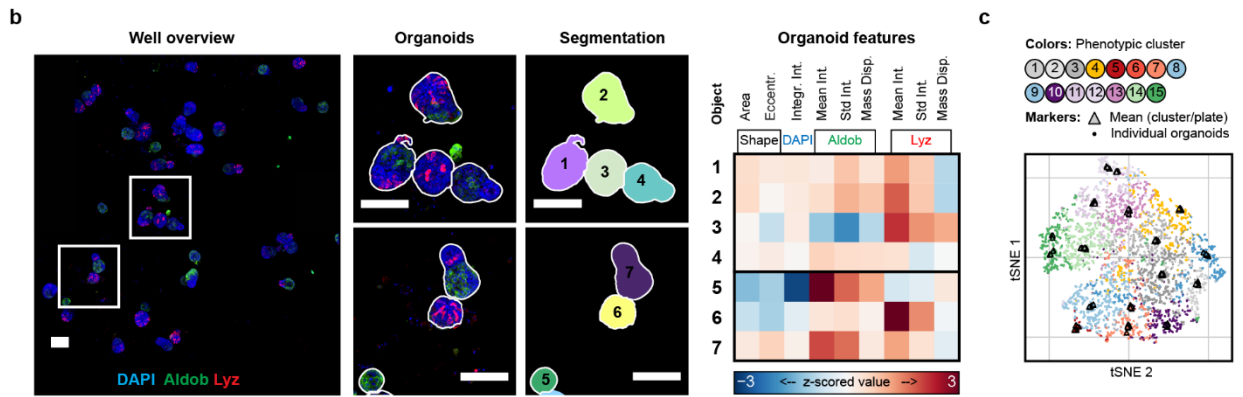
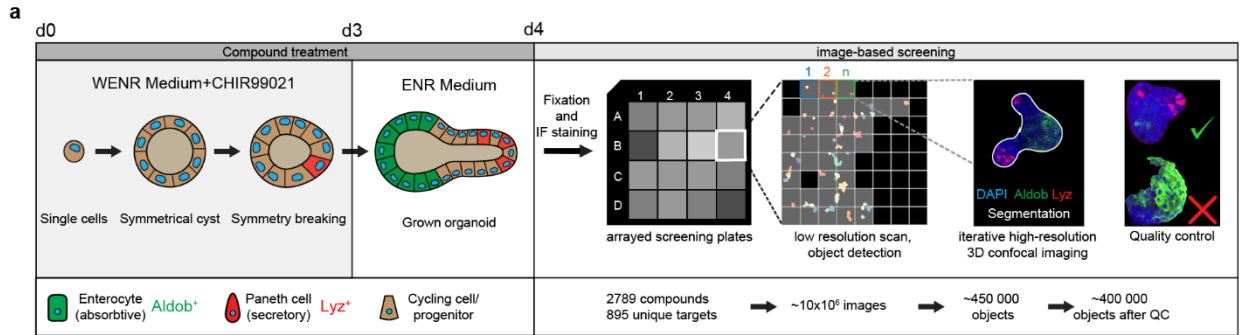


Figure 1 | Robust phenotypic signatures characterize the landscape of organoid development.

a, Overview of the image-based screening workflow used in this study. **b**, Left panel: an example image of a stitched well-level overview, regions indicated by white boxes, scale bar, 100 μm . Middle panel: enlarged regions from left panel, scale bar, 100 μm . Right panel: segmentation images for the objects shown in the middle panel, color-coded for object unique identifier (overlaid in black). Rightmost panel: heatmap of z-scored feature values extracted from indicated objects, Eccentr.: Eccentricity, Integr. Int.: Integrated Intensity, Mean Int.: Mean Intensity, Std Int.: Standard Deviation of intensity, Mass Disp.: Mass displacement for indicated immunofluorescence channels. **c**, tSNE map color coded for phenotypic clusters, every data point represents either an individual organoid or a mean value per cluster per plate (as indicated by marker type). Stratified sampling, 5% of entire data set. **d**, Phenotypic clusters identified using multivariate feature array. Upper panel: representative organoid images per class and cartoon representation of the observed phenotype. Bottom panel: heatmap of mean z-scored values per class for the indicated feature array. Feature naming as in panel b. **e**, Bar plot showing relative z-score transformed abundance of respective phenotypic clusters in the CHIR99021 condition (top), error bars show standard deviation. Heatmap representation of the phenotypic signature for two representative replicates and mean over 50 replicates (mean(50)) (bottom). **f**, Circular chart representing the initial library and selected hits, middle: Venn diagram representation of selected hits grouped by target coverage, right: Venn diagram representation of selected target genes grouped by reproducibility and hit list-specific enrichment. Microscopy images shown in **a**, **b** and **d** are composite maximum intensity projections of confocal z-stacks, nuclei, DAPI, antibody staining for Lysozyme (Lyz) and Aldolase B (Aldob).

Figure 2: Using HIS to infer functional interactions from a single phenotypic screen

a, Schematic of hierarchical interaction score (HIS) principle. HIS is calculated pair wise for a set of genes described by multivariate phenotypic signatures (left) to generate a matrix of graded interactions (middle) in which every interaction contains information on which readout contributed most to assigning the interaction. In the resulting HIS-based network (right) the strength of the interactions (thickness of the edges) reflects the similarity of the observed enrichment/depletion and directionality is from the gene with the broader set of effects to the gene with the narrower set of effects. **b**, Heatmap of the HIS pairs for the 230 target genes, all interactions with non-zero HIS values are shown color-coded for the phenotypic class readout contributing most to HIS value inference. **c**, Network visualization of the HIS interactions with HIS values ≥ 0.2 between 124 genes. Inner network: nodes are colored according to the highest enrichment detected for a phenotypic class, edge color indicates the phenotypic class readout contributing most to HIS value inference (see legend). Off-diagonal interactors depicted as highlighted labeled nodes inside the inner circular graph. Outer networks: detected subnetwork regions. Edge thickness reflects HIS interaction value (see legend), only edges with the highest HIS value per node are shown. Node outline indicates modality (inhibitor or activator), see legend. Functional annotations (KEGG terms) enriched per phenotype (inner circle) and per subnetwork (outer circle).

Phenotypic landscape of intestinal organoid development
APPENDIX

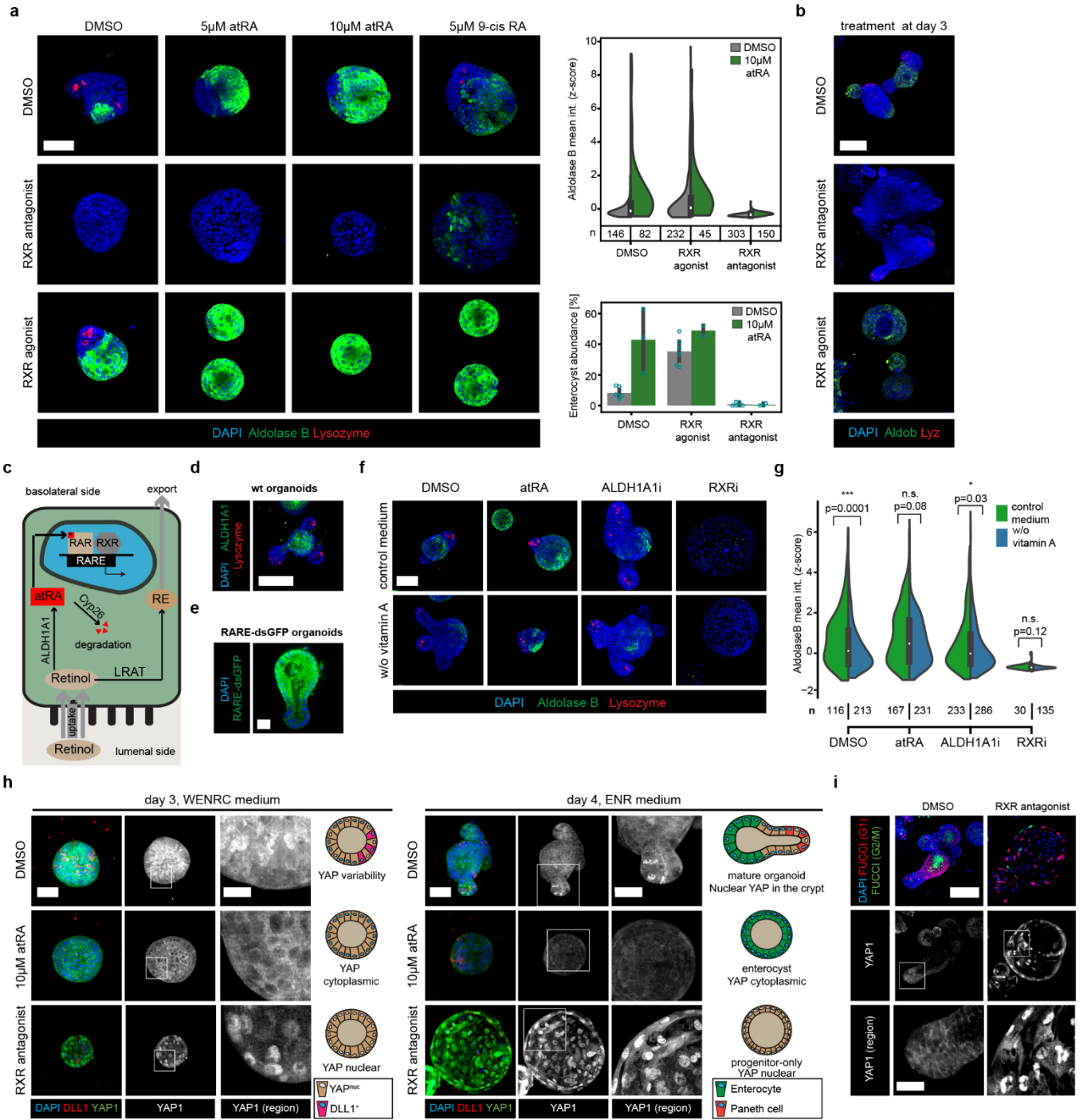


Figure 3 | Retinol metabolism and RXR activity are indispensable for enterocyte differentiation

a, Representative images of organoids cultured from single cells in indicated treatment conditions (left), nuclei, DAPI, antibody staining for Lysozyme and Aldolase B, scale bar, 50 μ m. Violin plots showing distribution of mean Aldolase B staining intensity in control and treated organoids (top right). Bar plot indicating abundance of the enterocyst phenotype in indicated conditions (bottom right), values are percentages in individual wells, n of 3 for 10 μ M atRA condition, n of 6 for DMSO control shown as mean \pm s.d. **b**, Representative images of organoids cultured from single cells, indicated treatment was performed concomitant with switch to ENR medium at day 3, nuclei, DAPI, antibody staining for Lysozyme (Lyz) and Aldolase B (Aldob), scale bar, 100 μ m. **c**, Schematic depiction of retinol metabolism in intestinal epithelial cells. Retinol is taken up from the lumen, converted to all-trans retinoic acid (atRA) by ALDH1A1, in the nucleus atRA binds Retinoid X receptor (RXR)- retinoic acid receptor (RAR) heterodimers bound to Retinoic acid response elements (RARE) activating target gene expression. Retinol can alternatively be metabolized to retinyl ester (RE) and transported to the lymph system, excess atRA can be degraded by cytochrome p450 enzymes (Cyp26). **d**, Representative images of wild type organoids cultured from single cells, fixed 48 hours after switching to ENR medium, antibody staining for Lysozyme and ALDH1A1, scale bar, 100 μ m. **e**, Representative image of a RARE-dsGFP organoid cultured from single cell (left). Confocal z-plane image from the middle plane of the organoid. Scale bar, 60 μ m. **f**, Representative images of wild type organoids cultured from single cells in medium with or without vitamin A. Indicated treatment concomitant with switch to ENR medium at day 3, organoids fixed 24 hours post-treatment (left). Nuclei, DAPI (blue), RARE-dsGFP. Scale bar, 50 μ m. **g**, Violin plots showing distribution of z-scored mean Aldolase B staining intensity (mean int. (z-score)) in control and treated organoids. Asterisks show statistical significance determined with two-sided t-test performed for same compound treatment in +/- Vitamin A condition, p values as indicated, n.s., not significant. **h**, Representative images and graphic representations of phenotypes observed in organoids cultured from single cells in indicated treatment conditions at day 3 (left panel) and day 4 (right panel), nuclei, DAPI, antibody staining for YAP1 and DLL1, scale bars, 50 μ m (day 3) or 50 μ m (day 4) Both panels: enlarged areas marked by white boxes in the middle column shown in the right column, scale bars, 10 μ m (day 3) or 20 μ m (day 4). **i**, Representative images of Fucci2 organoids cultured from single cells, with or without continuous presence of RXR antagonist fixed at day 4, mVenus-hGem(1/110) (FUCCI(G2/M)), mCherry-hCdt1(30/120)(FUCCI (G1)), scale bar, 100 μ m. Enlarged areas marked by white boxes in the middle row shown in the bottom row. Scale bar, 20 μ m. Microscopy images shown in **a**, **b**, **d**, **f**, **h** and **i** are composite maximum intensity projections of confocal z-stacks, nuclei, DAPI, antibody staining as indicated in individual panels. In the violin plots in **a** and **g** the violin range was extended by one standard deviation. Box plots inside violin plots show quartile range, whiskers show value interval with excluded outliers, white dots indicate median values, n, number of individual organoids in respective conditions. **f**, **g**: DMSO, DMSO control, RXRi, 5 μ M RXR antagonist, ALDH1A1i, 5 μ M ALDH1A1 inhibitor.

Phenotypic landscape of intestinal organoid development

APPENDIX

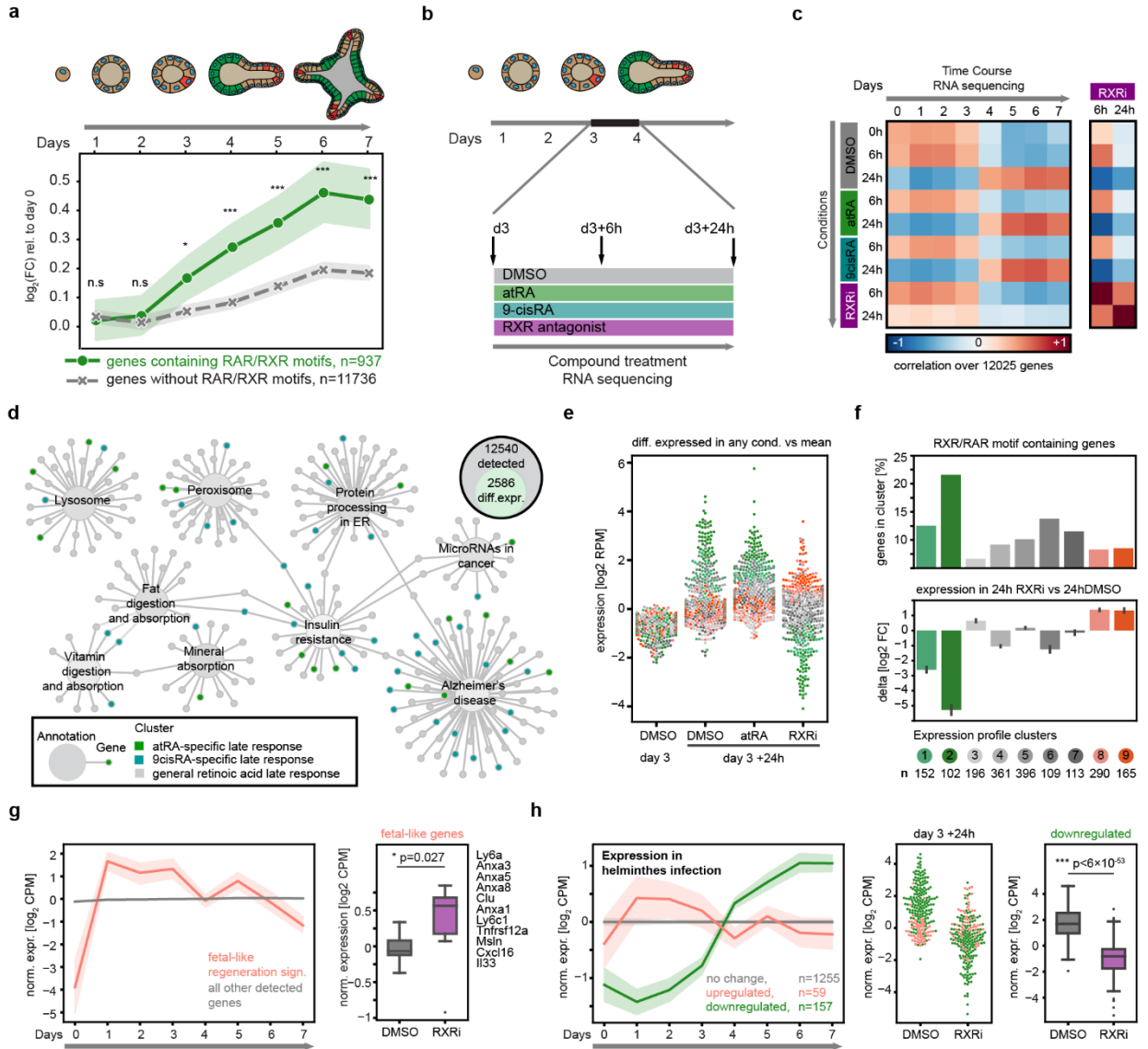


Figure 4 | RXR-mediated signaling is required for exit from regenerative state and acquisition of intestinal identity

a, Expression of genes containing RAR/RXR heterodimer transcription factor binding motifs in 1000 base pair region around the transcription start site during organoid development. Log₂-transformed fold change (log₂(FC)) of count per million (CPM) values, relative to the expression at day 0. Solid line indicates mean value, opaque interval shows standard deviation. **b**, Schematic depiction of the compound-based RNA sequencing experiment, d3, day 3 of organoid development from single cells. **c**, Heatmap representation of correlation values between samples of the time course RNA sequencing experiment and compound stimulation RNA sequencing experiment. Correlation values calculated for Log₂-transformed count per million (CPM) values, normalized to mean expression over all samples of respective data sets. 12025 genes detected in both data sets were used for calculation. DMSO, DMSO control, atRA, 10 μM all-trans retinoic acid, 9cis, 10μM 9-cis retinoic acid, RXRi, 5 μM RXR antagonist. **d**, Network representation of annotation enrichment analysis for genes differentially regulated in indicated treatment conditions. Small nodes show genes, large nodes show functional annotations. Color indicates treatment-specific annotations (see legend). **e**, Swarm plot depicting expression values of selected 1884 genes in day 3 untreated organoids and in indicated treatment conditions 24h hours after treatment. Every data point is a gene, color coded for assigned cluster label (k-means clustering). Stratified sampling, 50 genes per cluster, color-coded same as in **f**. **f**, Bar plots depicting abundance of genes containing RXR/RAR binding motifs in assigned clusters (top) and mean expression of genes from respective clusters in the RXR antagonist treated condition compared to DMSO (log₂ fold change)(bottom). Data shown for the indicated number of genes composing each cluster as mean ± s.d. **g**, Expression of genes associated with fetal-like regenerative signature during intestinal organoid development (left) and in RXR antagonist treated organoids (right). Left panel: Right panel: box plots show quartile range, whiskers show value interval with excluded outliers, white dots indicate median values. Log₂-transformed count per million (CPM) values, normalized to mean expression over all samples in respective datasets used in both subpanels. **h**, Expression of genes up- or downregulated in parasitic helminthes infection during intestinal organoid development (left) and in RXR antagonist treated organoids (right). Log₂-transformed count per million (CPM) values, normalized to mean expression per time point in the “no change” group (left) or to mean expression over all samples (right). **g** and **h**: in line plots, solid lines indicate mean values per time points, opaque interval shows standard deviation, in box plots boxes show quartile range, whiskers show value interval with excluded outliers, solid lines indicate median values. Asterisks show statistical significance determined with two-sided t-test, p values as indicated, n.s., not significant. In **f**, **g** and **h**, n indicates number of genes in respective groups.

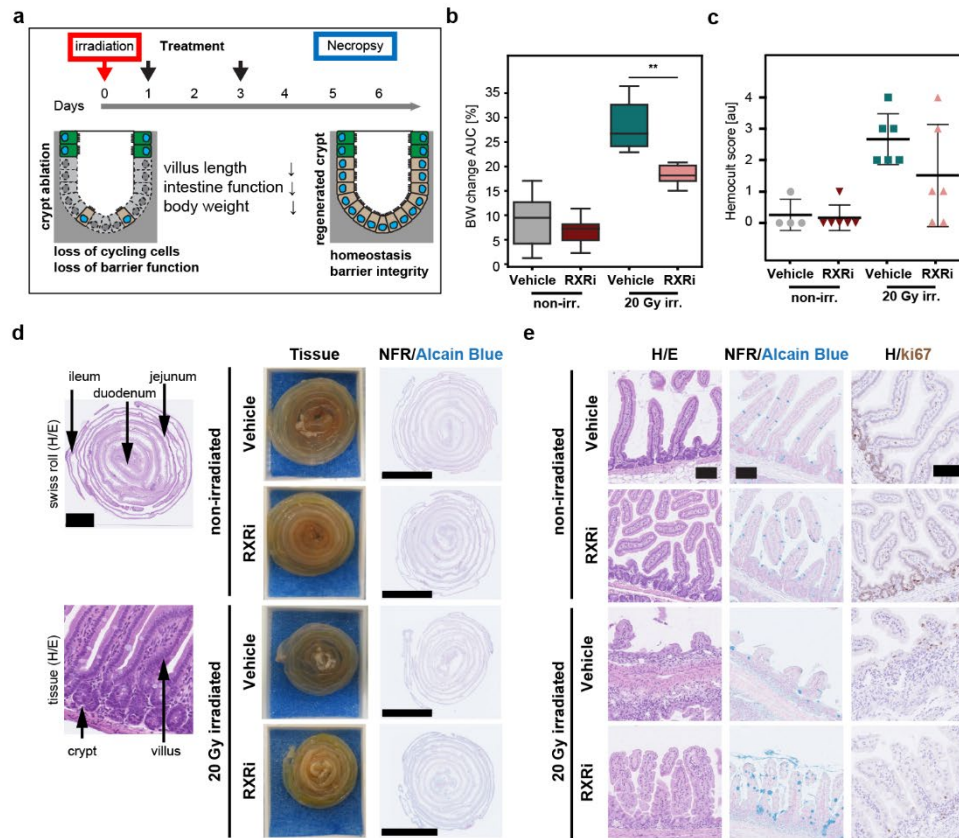


Figure 5 | RXR antagonist treatment improves intestine regeneration *in vivo*

a, Setup of the irradiation assay used in the mouse study and schematic depiction of the irradiation effect at the cellular level. **b**, Body weight change over the course of the mouse study for the indicated treatment groups ($n=6$ in each group) calculated as area under curve (AUC) for the indicated treatment groups. Box plots show quartile range, whiskers show value interval with excluded outliers, white dots indicate median values. Two-sided t-test, p values as indicated. **c**, Hemocult score of stool samples in indicated treatment groups. Every data point is a sample from an individual mouse belonging to the respective treatment cohort. **d**, Small intestine “Swiss rolls” from mice belonging to the indicated treatment groups (left) and histological images of the intestine (right). Scale bars, 5 mm (left), 10 mm (right). **e**, Histological staining of the jejunum part of the small intestinal tissue samples from indicated treatment groups. Goblet cells stained with Alcain Blue and cycling cells stained with ki67 antibody in indicated panels. Scale bars, 250 μm . Histology samples in **d** and **e** H&E, Hematoxylin and eosin stain, NFR, Nuclear Fast Red, Goblet cells stained with Alcain Blue.

Regenerative landscape of intestinal organoids

Ilya Lukonin^{1,2}, Denise Serra^{1,2}, Katrin Volkmann¹, Janine Baaten³, Rui Zhao³, Shelly Meeusen³, Francisca Maurer¹, Michael B. Stadler^{1,4}, Jeremy Jenkins⁵, Prisca Liberali^{1,2}

¹Friedrich Miescher Institute for Biomedical Research (FMI), Maulbeerstrasse 66, 4058 Basel, Switzerland

²University of Basel, Petersplatz 1, 4001 Basel, Switzerland

³Genomics Institute of the Novartis Research Foundation, 10675 John Jay Hopkins Drive, San Diego, CA 92121, USA

⁴Swiss Institute of Bioinformatics, Maulbeerstrasse 66, 4058 Basel, Switzerland

⁵ Novartis Institutes for Biomedical Research Chemical Biology & Therapeutics (CBT), 181 Massachusetts Avenue, Cambridge, MA 02139, USA

Extended Data Figures 1-9

Extended Data Figure 1 | Reproducibility of the image-based screen.

Extended Data Figure 2 | Robust phenotypic signatures

Extended Data Figure 3 | Identification of hit compounds and target genes

Extended Data Figure 4 | Validation of HIS predictive power

Extended Data Figure 5 | Profiling of the RXR antagonist treatment effect

Extended Data Figure 6 | Annotation enrichment analysis of cell type marker genes

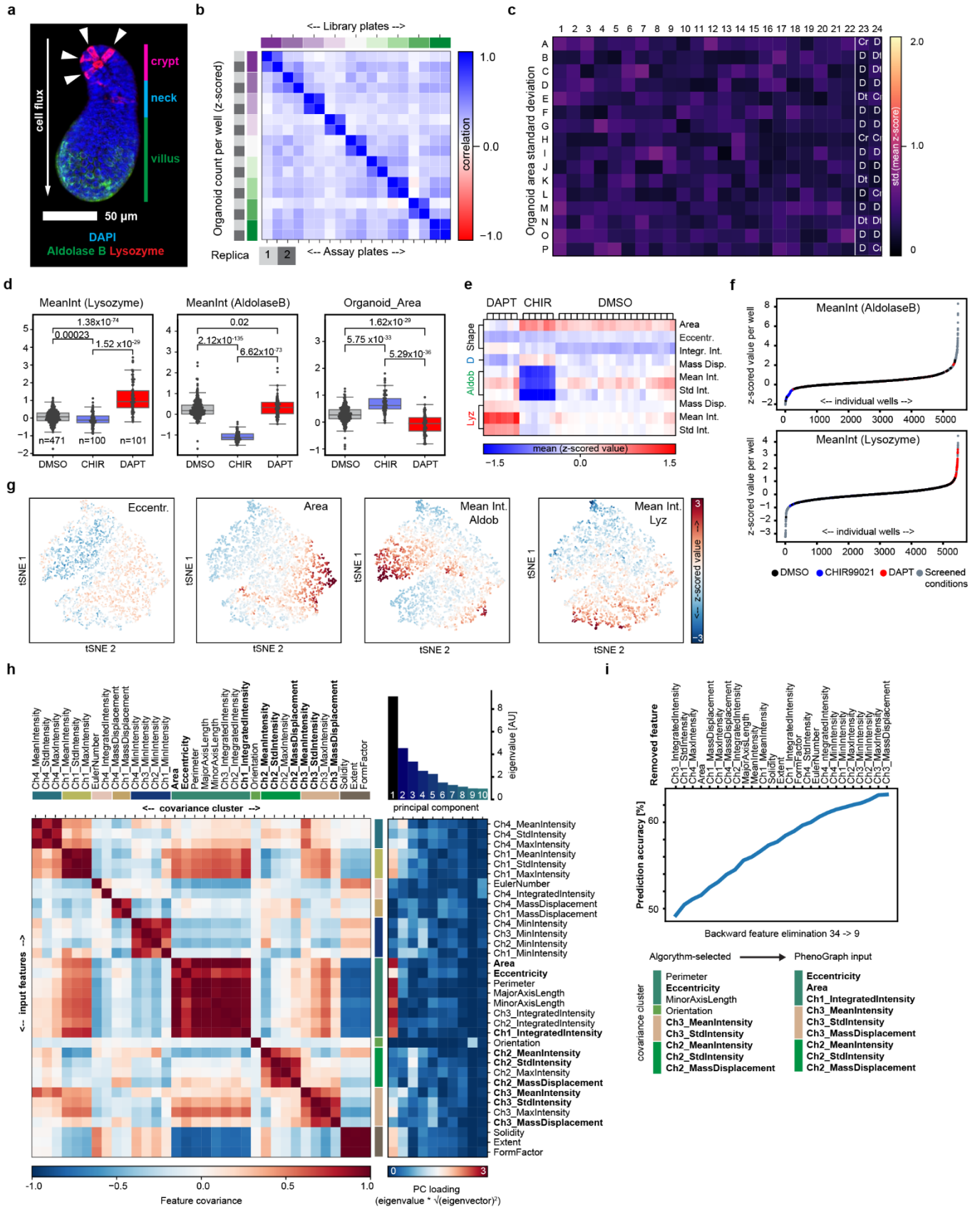
Extended Data Figure 7 | Transcriptional signature of RXRi-treated organoids

Extended Data Figure 8 | RXRi-treated organoids lose intestinal identity

Extended Data Figure 9 | RXRi treatment improves intestinal regeneration in irradiation-induced colitis model

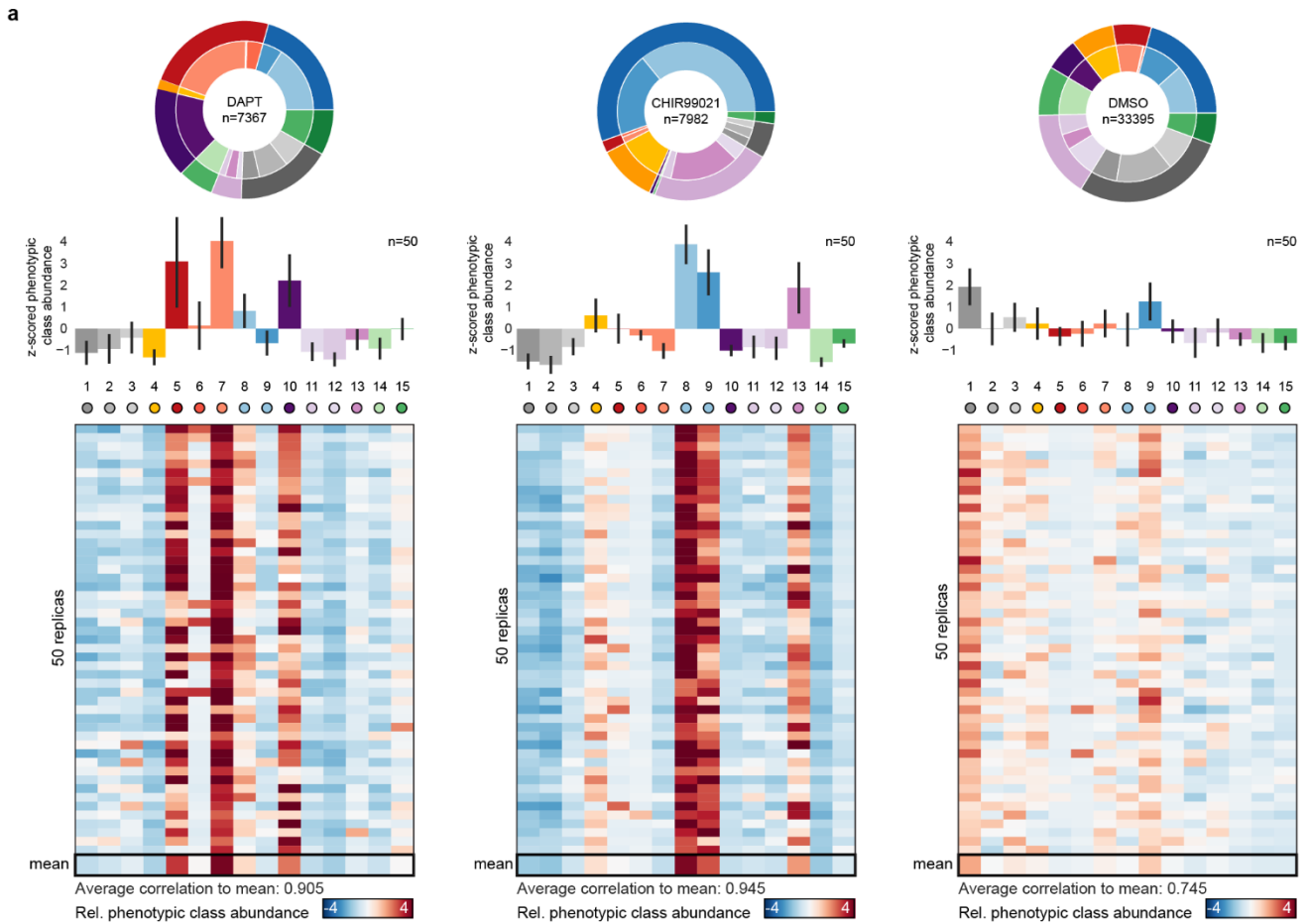
Phenotypic landscape of intestinal organoid development

APPENDIX



Extended Data Figure 1 | Reproducibility of the image-based screen.

a, An example image of an organoid with annotated regions along the major axis. Composite maximum intensity projection of a confocal z-stack. Antibody staining for Lysozyme (Lyz) and Aldolase B as indicated. Lysozyme-positive Paneth cells indicated by white arrowheads, scale bar, 50 μm . **b**, Reproducibility of detected organoid counts in replicas of the library plates. Heatmap shows correlation of organoid counts in screen replicates, plate replicates grouped by library plates as indicated. **c**, Heatmap of standard deviation of organoid size (z-scored organoid area) for respective well positions, passive and active controls indicated as D: DMSO, Cr: CHIR 99021, Dt: DAPT. **d**, Box plots showing distribution of mean values per well of indicated features in active and passive control conditions, middle line indicates median, boxes show the quartile range, individual data points shown as overlaid swarm plot. Statistical significance determined with two-sided t-test, p values as indicated. Mean Int.: Mean Intensity. **e**, Heatmap of z-scored organoid features used for clustering shown for individual well position of in-plate replicates of active and passive control conditions, mean values over 18 assay plates. Eccentr.: Eccentricity, Integr. Int.: Integrated Intensity, Mean Int.: Mean Intensity, Std Int.: Standard Deviation of intensity, Mass Disp.: Mass displacement for indicated immunofluorescence channels: DAPI (D), Lysozyme (Lyz) and Aldolase B (Aldob). **f**, Value distribution of indicated parameters, plot shows distribution of mean z-scored values of indicated features per well for the entire data set, sorted in ascending order. Every data point is an average value per well, control conditions color-coded as indicated in the legend. **g**, tSNE map color coded for z-scored values of indicated features (left to right: eccentricity, organoid area, mean intensity of AldolaseB and Lysozyme antibody staining), every data point represents an individual organoid, stratified sampling by PhenoGraph assignment, 5% of entire data set. **h**, Covariance matrix of the 34 extracted features (left), clustered by covariance (c-means clustering) into 10 clusters. Heatmap representation of principal component loading of the extracted features (right), eigenvalues of first 10 principal components shown as bar chart above. **i**, Line plot showing the naïve bayes predictor accuracy change throughout backwards feature elimination test. Final set of 9 features (“algorithm selected”) and list of features used as input for clustering with PhenoGraph shown below.

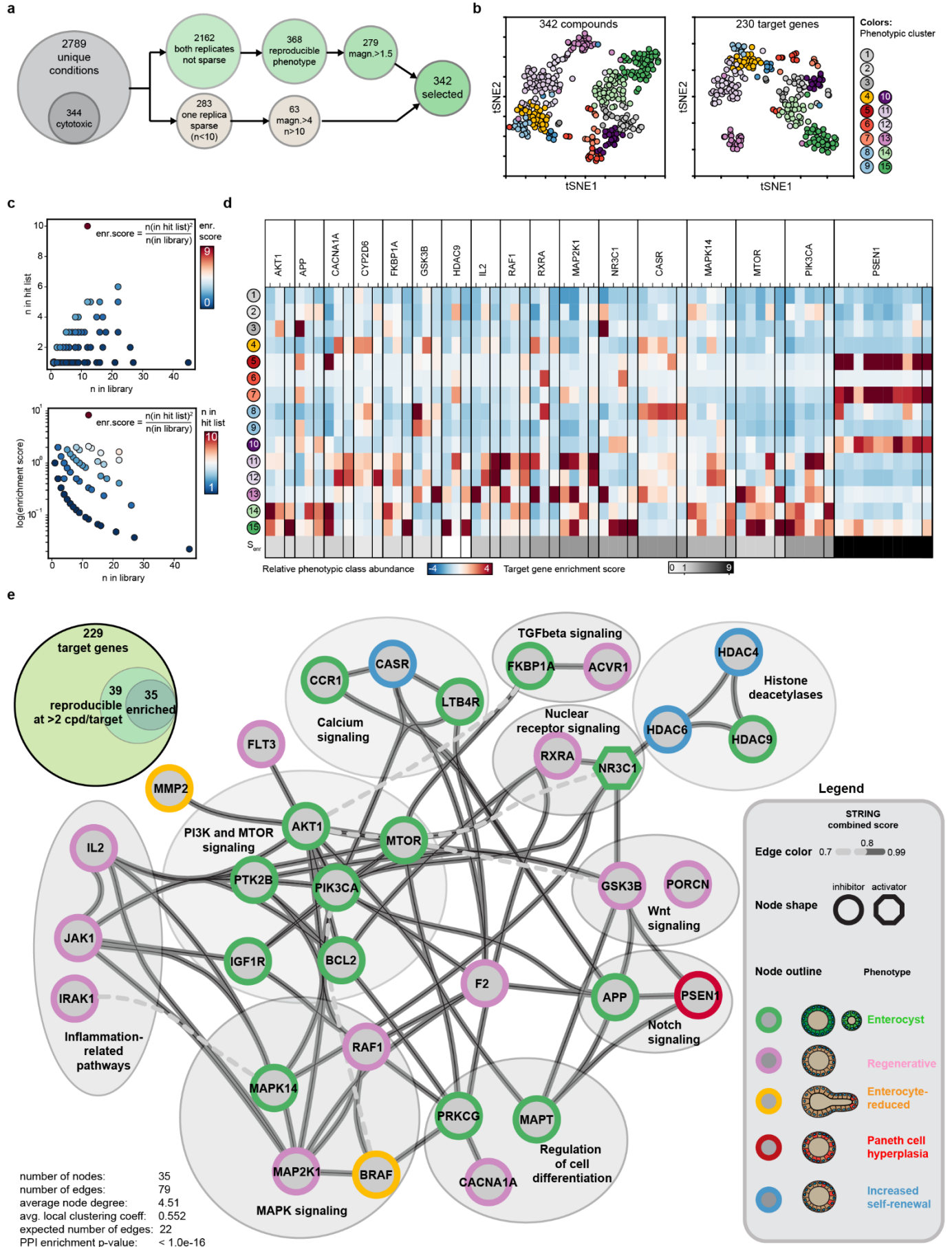


Extended Data Figure 2 | Robust phenotypic signatures

a, Circular graphs depicting distribution of phenotypic class assignment of organoids in control conditions (top) outer circle color indicates phenotypic group (see Fig. 1), inner circle color indicates assigned phenotypic cluster, n= 7367, 7982 and 33395 individual organoids for DAPT, CHIR99021 and DMSO conditions respectively. Bar plots showing relative z-score transformed abundance of respective phenotypic clusters, shown as mean \pm s.d. (middle). Heatmap representation of the individual and mean phenotypic signature for 50 replicates of the indicated control conditions (bottom).

Phenotypic landscape of intestinal organoid development

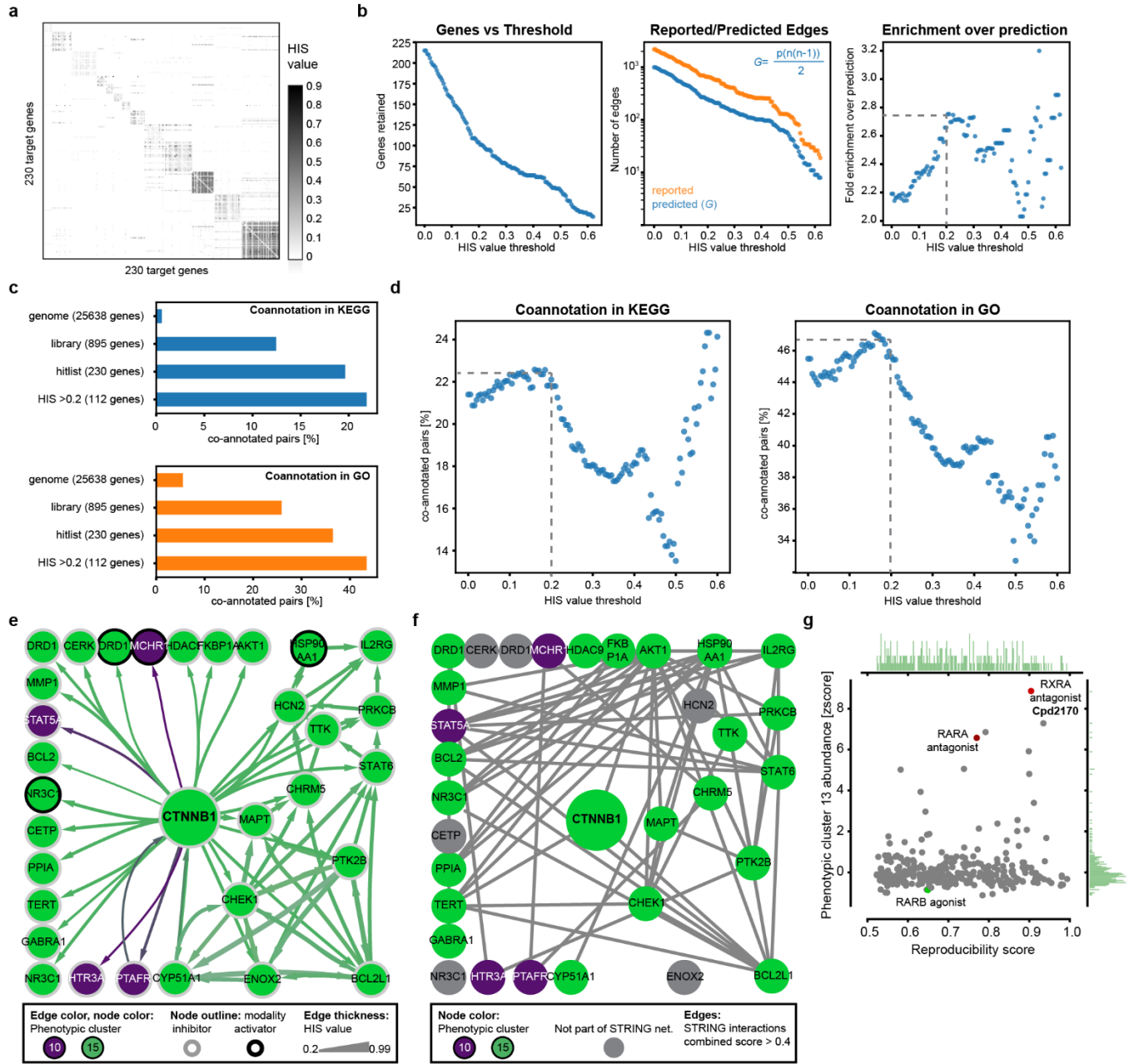
APPENDIX



Extended Data Figure 3 | Identification of hit compounds and target genes

a, Flowchart depicting filtering of the screened conditions, Magnitude (magn.) indicates the maximum z-scored abundance value detected for any phenotypic cluster. **b**, tSNE map color coded for phenotypic clusters as indicated, every data point represents either a compound condition (left) or a unique target gene-modality pair (right), tSNE calculated from 15-dimensional phenotypic signatures. Venn diagrams show compound coverage of target genes (left) and reproducibility per gene and enrichment from initial library (right). **c**, Scatterplot illustrating the compound abundance in library and hit list (left) and enrichment score distribution (right) for targets of the screen hits. Every data point is a unique target gene-modality pair. **d**, Heatmap of phenotypic signatures for a subset of genes with compound coverage ≥ 2 compounds per gene. Outlined heatmap rows indicate conditions used as representative conditions per target. S_{enr} , target enrichment score, see panel **c**. **e**, Venn diagram indicating the distribution of target genes by compound coverage (top left). Network of functional interactions for the set of genes with high compound coverage and hitlist specific enrichment, edges represent interactions known in the STRING database, thickness and line type represent STRING combined score (see network legend), nodes are unique target gene-modality pairs, node outline indicates the phenotypic cluster with highest enrichment. Circles indicate groups of similar functional annotation.

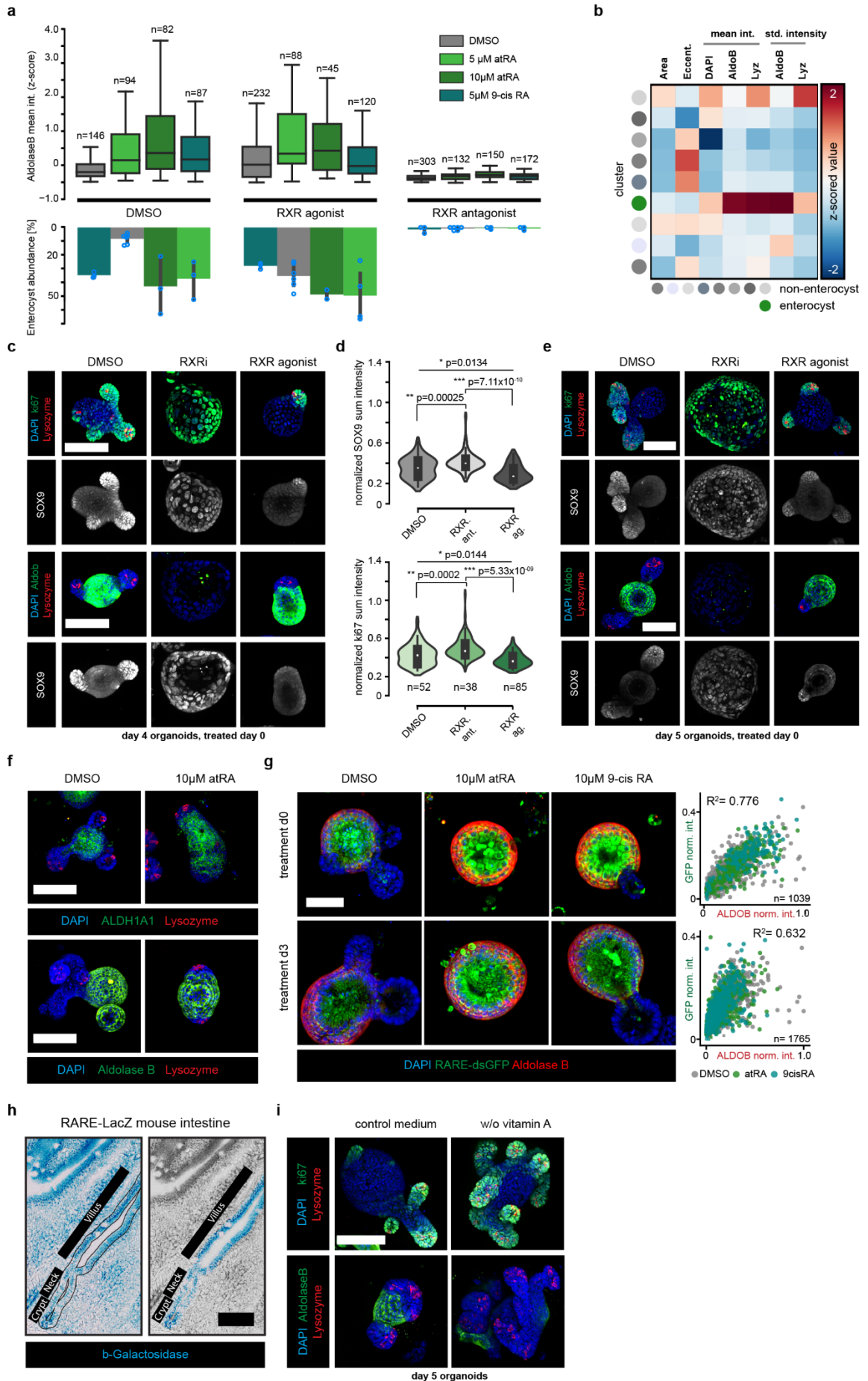
Phenotypic landscape of intestinal organoid development
APPENDIX



Extended Data Figure 4 | Validation of HIS predictive power

a, Heatmap of the HIS pair-wise interactions for the 230 target genes, color-coded for the HIS value. **b**, Scatter plots depicting number of retained nodes (left), number of STRING-reported and predicted edges (see Materials and Methods) (middle) and fold enrichment of reported STRING interactions over prediction (right) with increasing HIS threshold cutoff in the range from 0 to 0.6. Grey dashed line indicates the HIS value cutoff of 0.2. **c**, Bar plot showing percentage of co-annotated (KEGG, left, GO(levels 5-15), right) gene pairs in indicated sets of genes. **d**, Scatter plots showing percentage of co-annotated (KEGG, left, GO(levels 5-15), right) gene pairs present in the HIS interaction matrix with increasing HIS threshold cutoff in the range from 0 to 0.6. Grey dashed line indicates the HIS value cutoff of 0.2. **e**, HIS-based interaction network of beta-Catenin: nodes are colored according to the highest enrichment detected for a phenotypic class, edge color indicates the phenotypic class readout contributing most to HIS value inference (see legend) and edge arrow shape represents HIS-inferred directionality. All edges directed to/from beta-Catenin are shown, other only shown for HIS values above 0.6. **f**, Reported STRING interactions for the HIS-based interaction network of beta-Catenin: nodes are colored according to the highest enrichment detected for a phenotypic class, edges represent STRING-reported interactions with combined score above 0.4. **g**, Scatter plot depicting Phenotypic cluster 13 abundance in the hit conditions with reproducibility value above 0.5, compounds targeting RXR and RAR depicted with colored dots. Histograms show distributions of respective values.

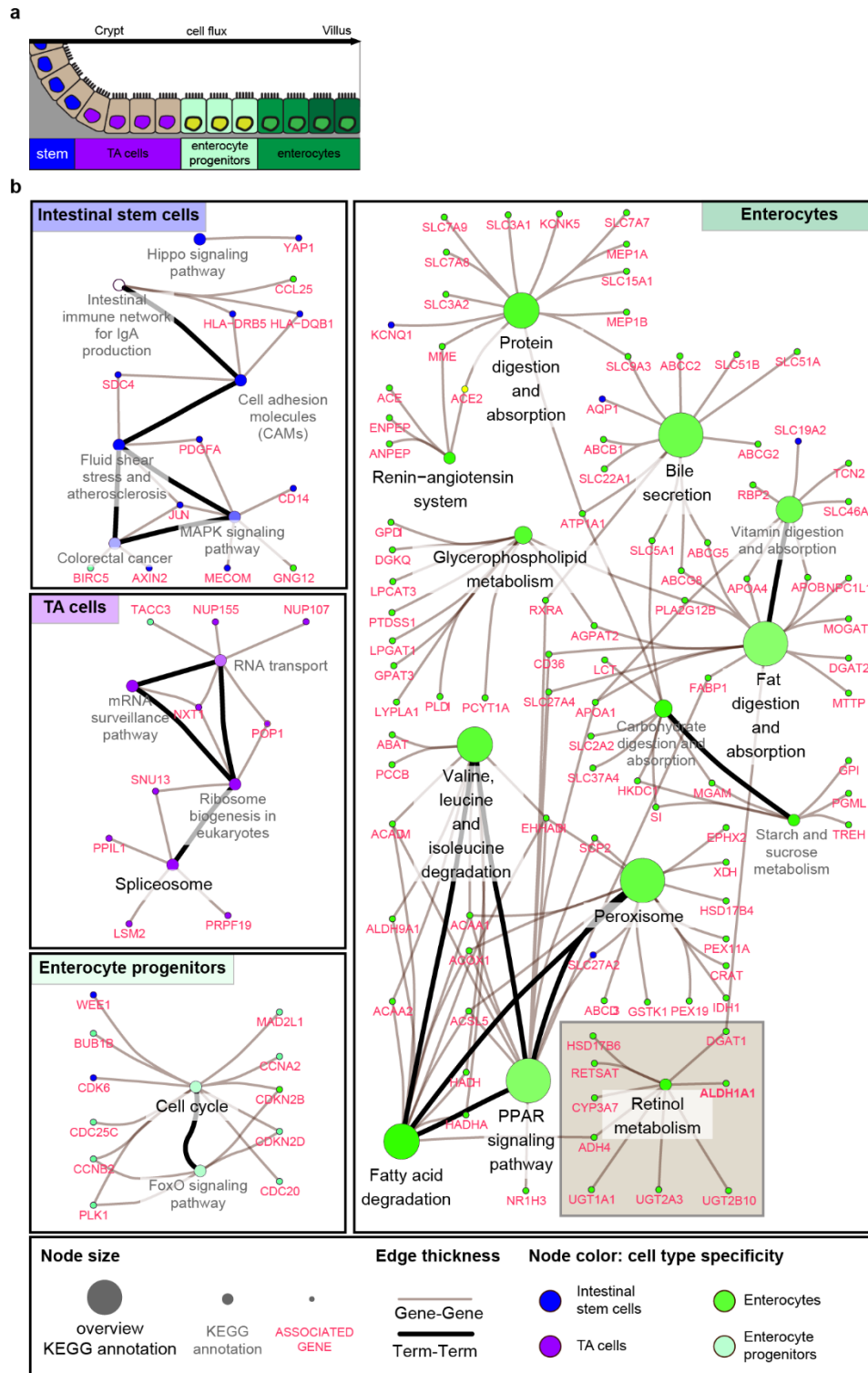
Phenotypic landscape of intestinal organoid development
APPENDIX



Extended Data Figure 5 | Profiling of the RXR antagonist treatment effect

a, Box plots showing distribution of mean Aldolase B staining intensity in control and treated organoids fixed at day 4 (top). Box plots show quartile range, whiskers show value interval with excluded outliers, middle lines indicate median values. Bar plots showing the abundance of enterocyst phenotype in indicated conditions (bottom). Error bars show standard deviation between technical replicates. N=3 for compound conditions and n=6 for DMSO controls. **b**, Heatmap representation of z-scored mean feature values per phenotypic class identified using PhenoGraph. **c**, Representative images of organoids cultured from single cells in indicated treatment conditions. Organoids fixed at day 4, 24 hours post switch to ENR medium, nuclei (DAPI) and antibody staining for Lysozyme, ki67 and SOX9 as indicated, scale bar, 100 μm . **d**, Violin plots showing distribution of mean Aldolase B (left) and SOX9 (right) staining intensity in control and treated organoids. Organoids fixed at day 5, 48 hours post switch to ENR medium. Violin range extended by one standard deviation. Box plots inside violin plots show quartile range, whiskers show value interval with excluded outliers, white dots indicate median values. Two-sided t-test, p values as indicated. **e**, Representative images of organoids cultured from single cells in indicated treatment conditions. Organoids fixed at day 5, 48 hours post switch to ENR medium (left). Nuclei, DAPI, and antibody staining for Lysozyme, Aldolase B and SOX9 (bottom) or antibody staining for Lysozyme, ki67 and SOX9 (top), scale bars, 100 μm . **f**, Representative images of wild type organoids cultured from single cells, indicated treatment was performed concomitant with switch to ENR medium at day 3 and organoids fixed 48 hours post-treatment. Nuclei, DAPI, antibody staining for Lysozyme and ALDH1A1 (top) or Lysozyme, and Aldolase B (bottom), scale bar, 100 μm . **g**, Representative images of RARE-dsGFP organoids cultured from single cells in indicated treatment conditions (left). Nuclei, DAPI, RARE-dsGFP and antibody staining for Aldolase B. Scale bar, 60 μm . Scatter plots depicting DAPI-normalized sum intensity of RARE-dsGFP reporter (GFP norm. int.) and Aldolase B (ALDOB norm. int.) antibody staining in individual organoids (right). Every data point is an individual organoids, color-coded for treatment condition as indicated. R^2 , Pearson correlation coefficient. **h**, Histological images of mouse small intestinal epithelium from RARE-LacZ mouse. Beta-Galactosidase staining in blue, regions along the crypt-villus axis as indicated. A single crypt flanked by villus regions highlighted in left panel shown in color in the right panel. Scale bar, 50 μm . **i**, Representative images of organoids cultured from single cells in indicated treatment conditions. Organoids fixed at day 5, 48 hours post switch to ENR medium (left). Composite maximum intensity projection of a confocal z-stack, DAPI and antibody staining for Lysozyme, Aldolase B and SOX9 (bottom) or antibody staining for Lysozyme, ki67 and SOX9 (top), scale bar, 100 μm . Microscopy images shown in **c**, **e**, **f**, **g** and **i** are composite maximum intensity projections of confocal z-stacks.

Phenotypic landscape of intestinal organoid development
APPENDIX

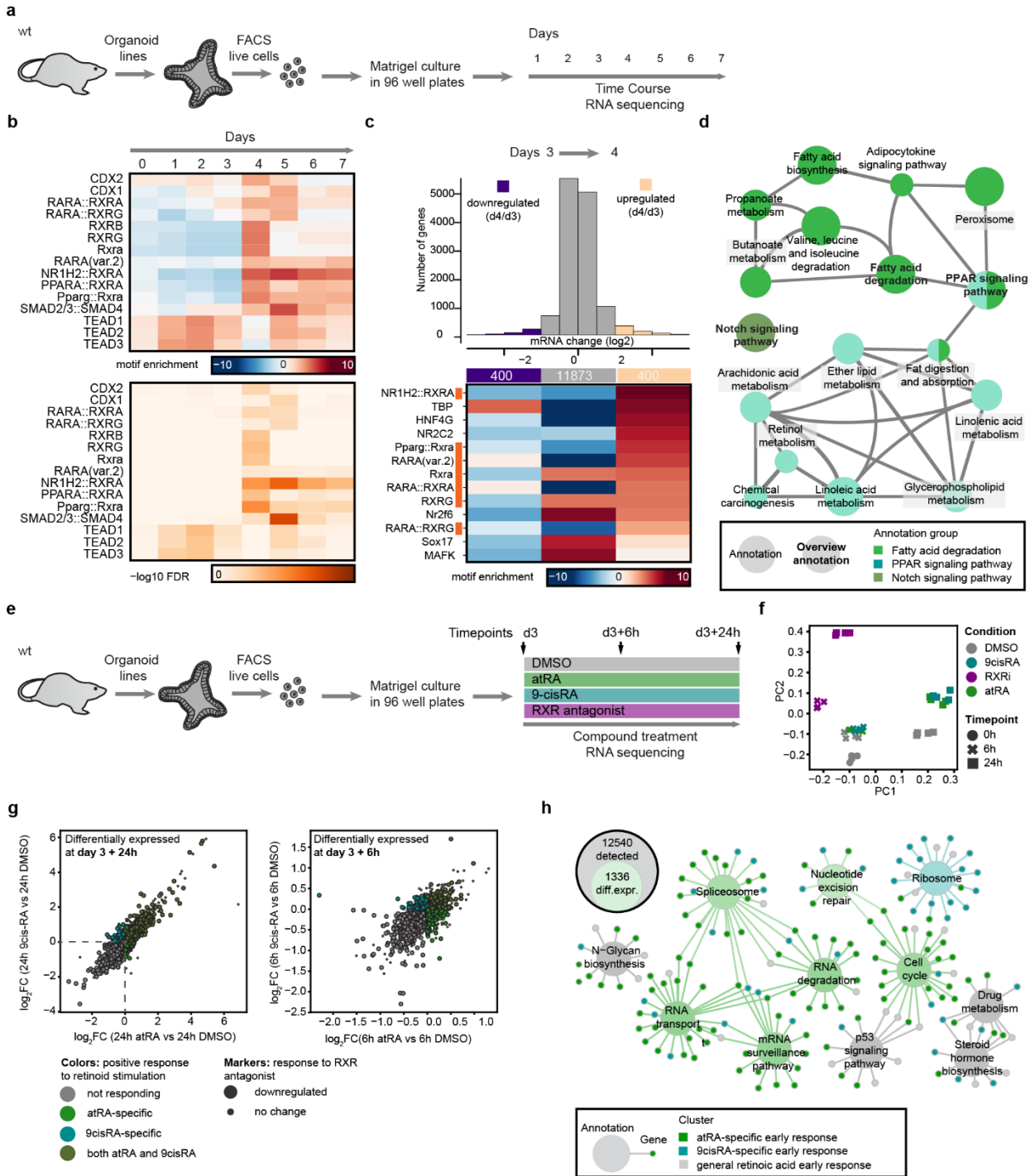


Extended Data Figure 6 | Annotation enrichment analysis of cell type marker genes

a, Schematic depiction of cell flux and cell fate transitions towards enterocyte fate at the crypt-villus boundary. **b**, Network representation of annotation enrichment analysis for published RNA sequencing dataset describing marker genes of intestinal epithelium cell types (see text for reference). Small nodes with labels in red show genes, large nodes show functional annotations. Edge thickness indicates either gene-annotation assignments (grey) or term-term relations (bold black). Color indicates cell type specificity of the annotations (see legend).

Phenotypic landscape of intestinal organoid development

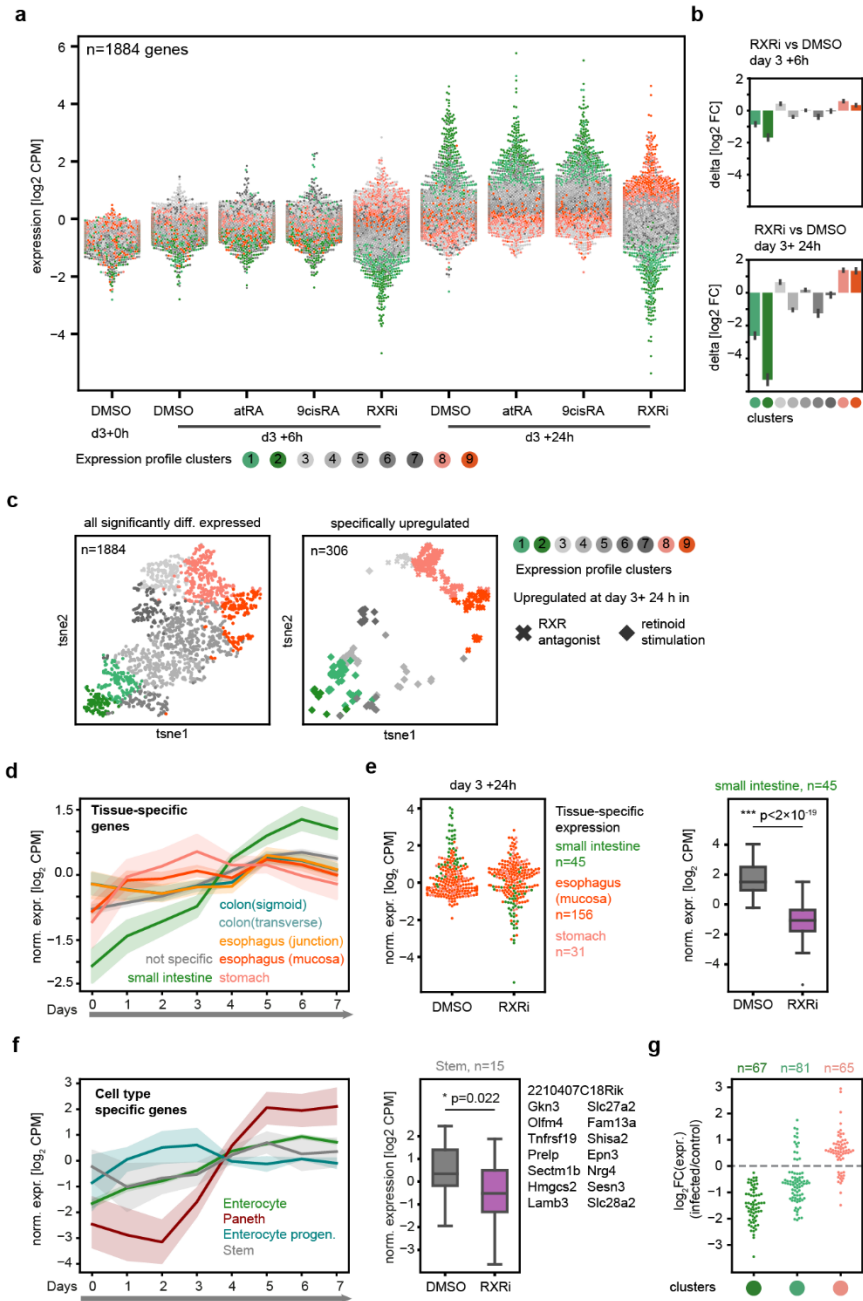
APPENDIX



Extended Data Figure 7 | Transcriptional signature of RXR α -treated organoids

a, Setup of the time course RNA sequencing experiment in wild type organoids. **b**, Motif enrichments in promoters of genes that are higher expressed at a given day compared to the average over all days (top) and corresponding false discovery rate (FDR) values (bottom) throughout the organoid development. **c**, Histogram showing the binning of genes according to their expression change at the transition from day 3 to day 4 time point (top) and enrichment heatmap of transcription factor binding motifs in respective bins (below). **d**, Network of functional annotation terms (KEGG) specifically enriched in genes containing RXR- and RAR-containing transcription factor binding motifs. Nodes are annotation terms, edges show term-term interactions. Node color represents annotation groups (see legend). **e**, Setup of the compound treatment RNA sequencing experiment in wild type organoids (left). atRA, all-trans retinoic acid, 9cisRA, 9-cis retinoic acid. **f**, Principal component analysis of RNA sequencing samples belonging to indicated treatment conditions and time points, scatter plot shows the first two principal components. N=4 (two technical replicates of 2 biological replicates) for all individual conditions. **g**, Scatter plots showing normalized gene expression in indicated contrast. Colors represent response to retinoid stimulation and sizes depict response to RXR antagonist treatment (see legend). Dashed box in left panel shows the selection criteria for genes depicted in the right panel. Color and marker type: see legend. **h**, Network representation of annotation enrichment analysis for 1336 genes differentially regulated at 6 hour time point in indicated treatment conditions. Small nodes show genes, large nodes show functional annotations. Color indicates treatment-specific annotation enrichment (see network legend).

Phenotypic landscape of intestinal organoid development
APPENDIX

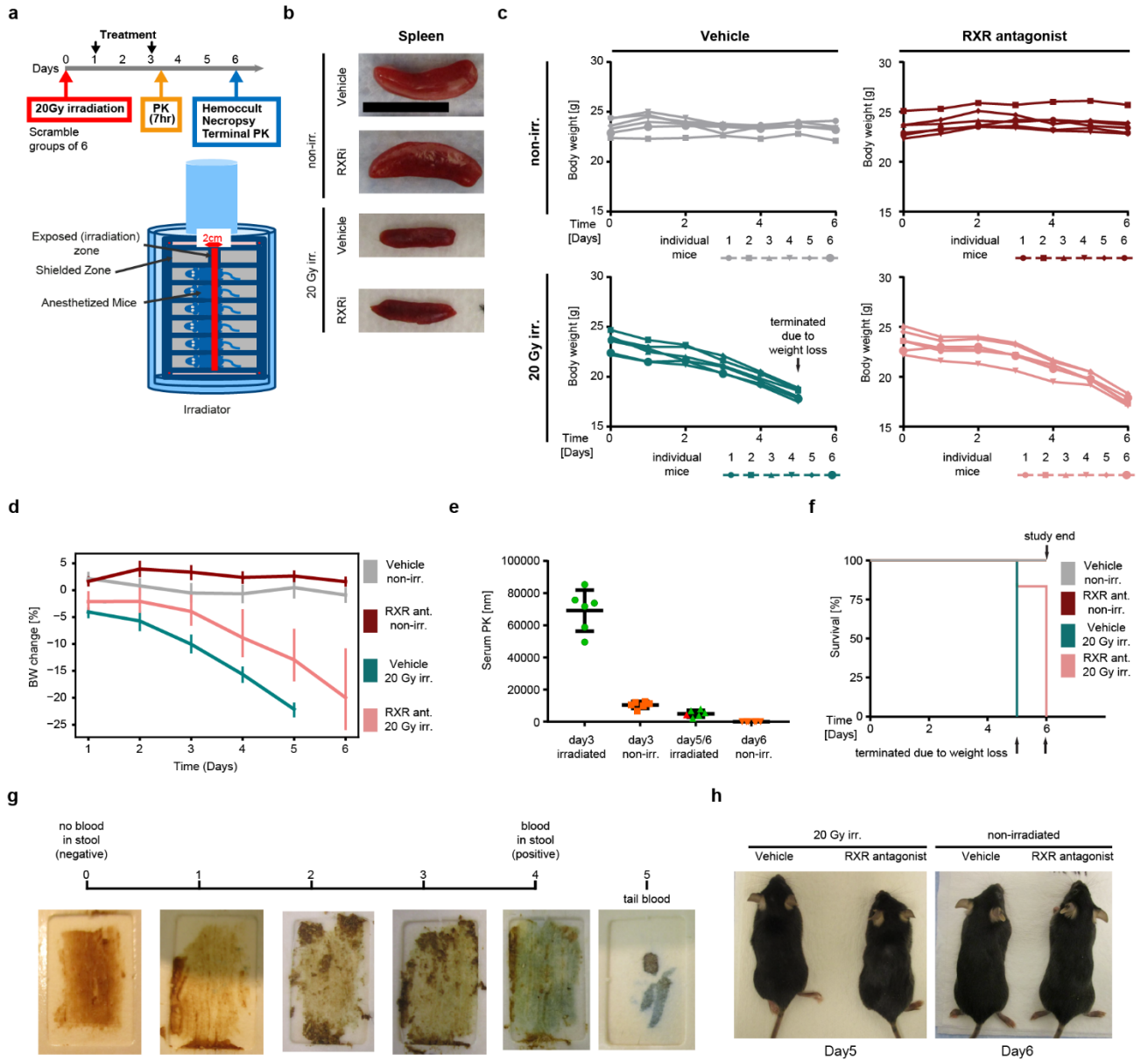


Extended Data Figure 8 | RXRi-treated organoids lose intestinal identity

a, Swarm plot showing expression of genes significantly perturbed in any of the conditions in the RNA sequencing experiment (above 2-fold change with $FDR < 0.1$) color coded for gene expression profile cluster (k-means clustering). DMSO, DMSO control, atRA, 10 μ M all-trans retinoic acid, 9cis, 10 μ M 9-cis retinoic acid, RXRi, 5 μ M RXR antagonist. **b**, Bar plot showing relative gene expression (mean per expression profile cluster) in RXR antagonist treated samples compared to DMSO control at indicated time points (right). Error bars show standard deviation between replicates for indicated contrasts. **c**, tSNE map color coded for assigned cluster label (k-means clustering). tSNE calculated from expression values (log₂-transformed count per million (CPM) values, normalized to mean expression over all samples) (left). Genes showing treatment-specific upregulation and downregulation in orthogonal compound condition (right). Every data point is a gene. **d**, Expression of genes reported to have biased expression in indicated GI tract tissues during intestinal organoid development. Log₂-transformed count per million (CPM) values, normalized to mean expression over all samples. **e**, Swarm plot showing expression of genes reported to have biased expression in indicated GI tract tissues in RXR antagonist-treated organoids and DMSO control after 24h of treatment (left), expression of genes biased for stem cells in RXR antagonist treated organoids (right). **f**, Expression of genes reported to have biased expression in indicated cell types of the small intestine during intestinal organoid development (left), expression of genes biased for stem cells in RXR antagonist treated organoids (right). Log₂-transformed count per million (CPM) values, normalized to mean expression over all samples in respective data sets. **g**, Swarm plot showing relative expression of genes from indicated expression profile clusters (see panel a) in helminthes infection compared to non-infected control, log₂-transformed fold change, dashed line indicates 0 fold change. **d** and **f**: in line plots, solid lines indicate mean values per time points, opaque interval shows standard deviation, in **e** and **f** in box plots boxes show quartile range, whiskers show value interval with excluded outliers, solid lines indicate median values. Asterisks show statistical significance determined with two-sided t-test, p values as indicated. DMSO, DMSO control, RXRi, 5 μ M RXR antagonist.

Phenotypic landscape of intestinal organoid development

APPENDIX



Extended Data Figure 9 | RXR α treatment improves intestinal regeneration in irradiation-induced colitis model

a, Schematic depiction of the irradiation induced colitis model study. PK, pharmacokinetic analysis. **b**, Images of the spleen extracted from mice belonging to indicated treatment cohorts. Scale bar, 1cm. **c**, Line plots showing body weight measurement results for individual mice from indicated treatment cohorts over the time frame of the study. **d**, Line plots showing body weight change in indicated treatment cohorts over the time frame of the study, data shown are mean values for cohorts of $6 \pm$ s.d. **e**, Serum levels of the RXR antagonist compound at 6 hours post-treatment (day3) or at the end of mouse study in irradiated and non-irradiated mice. **f**, Line plot showing the survival rates for indicated treatment cohorts. Arrowheads indicate time points at which mice were sacrificed due to weight loss (see Materials and Methods). **g**, Representative images of the hemocult samples corresponding to the quantitative hemocult scores used in **Fig. 5c**. **h**, Images of the animals from indicated treatment cohorts at day 5 and day 6, as indicated.

Regenerative landscape of intestinal organoids

Ilya Lukonin^{1,2}, Denise Serra^{1,2}, Katrin Volkmann¹, Janine Baaten³, Rui Zhao³, Shelly Meeusen³, Francisca Maurer¹, Michael B. Stadler^{1,4}, Jeremy Jenkins⁵, Prisca Liberali^{1,2}

¹Friedrich Miescher Institute for Biomedical Research (FMI), Maulbeerstrasse 66, 4058 Basel, Switzerland

²University of Basel. Petersplatz 1, 4001 Basel, Switzerland

³Genomics Institute of the Novartis Research Foundation, 10675 John Jay Hopkins Drive, San Diego, CA 92121, USA

⁴Swiss Institute of Bioinformatics, Maulbeerstrasse 66, 4058 Basel, Switzerland

⁵ Novartis Institutes for Biomedical Research Chemical Biology & Therapeutics (CBT), 181 Massachusetts Avenue, Cambridge, MA 02139, USA

Supplementary information

Supplementary Table 1: antibody stocks, dilutions and incubation times used for immunofluorescence staining in this study

Figure S1: Gating strategy for flow cytometry to remove debris, dead cells and cell doublets

Methods

Organoid lines

Experiments using the irradiation-induced injury model were conducted according to Institute of Animal Care and Use Committee guidelines. All other animal experiments were approved by the Basel Cantonal Veterinary Authorities and conducted in accordance with the Guide for Care and Use of Laboratory Animals. Male and female outbred mice between 7 and 15 weeks old were used for all experiments. Mouse lines used: C57BL/6 wild type (Charles River Laboratories and Jackson labs), RARE-LacZ (kind gift from Filippo Rijli, Friedrich Miescher Institute for Biomedical Research, Basel, Switzerland), Fucci2 (kind gift from Jan Skotheim, Stanford University, Stanford, United States).

Organoid culture

Organoids were generated from isolated crypts of the murine small intestine as previously described¹. In brief, the section of the initial part of the small intestine was opened lengthwise, cleaned with cold PBS and, after removal of villi by scraping with a cold glass slide, sliced into small fragments roughly 2 mm in length. The tissue was then incubated in 2.5 mM EDTA/PBS at 4 °C for 30 min with shaking. Supernatant was removed and pieces of intestine were re-suspended in DMEM/F12 with 0.1% BSA. The tissue was then shaken vigorously. To collect the first fraction, the suspension was passed through a 70 µm strainer. The remaining tissue pieces were collected from the strainer and fresh DMEM/F12 with 0.1% BSA was added, followed by vigorous shaking. The crypt fraction was again collected by passing through a 70 µm strainer. In total, 4 fractions were collected. Each fraction was centrifuged at 300g for 5 min at 4 °C. Supernatant was removed and the pellet was re-suspended into Matrigel with medium (1:1 ratio) and plated into 24 well plates. Organoids were kept in IntestiCult Organoid Growth Medium (STEMCELL Technologies) with 100 µg/ml Penicillin-Streptomycin for amplification and maintenance.

Image-based screening assay

Organoids were collected 5-7 days after passaging and digested with TripLE (Invitrogen) for 20 min at 37 °C. Dissociated cells were passed through a cell strainer with a pore size of 30 µm. For the screening assay, number of cells was estimated using Moxi Flow (Orflo Technologies), counting objects between 9 and 20 µm in size. Isolated cells were collected in ENR medium composed of advanced DMEM/F-12 with 15 mM HEPES (STEM CELL Technologies) supplemented with 100 µg/ml Penicillin-Streptomycin, 1xGlutamax (Thermo Scientific), 1xB27 (Thermo Scientific), 1xN2 (Thermo Scientific), 1mM N-acetylcysteine (Sigma), 500ng/ml R-Spondin (kind gift from Novartis), 100 ng/ml Noggin (PeproTech) and 100 ng/ml murine EGF (Thermo Scientific) (ENR medium). Resuspended cells were mixed with Matrigel (Corning) in a medium to Matrigel ratio of 1:1. In each well of a 384 well plate (CellCarrier-384, PerkinElmer cat nr. 6007550), 10µl per well of Matrigel-medium mixture was dispensed using EL406 Combination Washer Dispenser (BioTek Instruments), covering the entire bottom of the well. After 10 min of solidification at RT, 40 µl of medium per well containing 5000 cells was overlaid. Cells were brought into the matrix by gentle centrifugation (300 RCF, 5 minutes at 10°C). Subsequently, plates were left to solidify for 15 min at 37°C. From day 0 to day 3, WENRC medium (ENR was supplemented with 20% Wnt3a-conditioned medium (Wnt3a-CM), 10 µM Y-27632 (ROCK inhibitor, STEMCELL Technologies) and 3 µM of CHIR99021 (GSK3B inhibitor, STEMCELL Technologies, cat # 72054)) was used for organoid culture. Wnt3a-CM was produced in-house by Wnt3a L-cells (kind gift from Novartis). From day 3 to 5, ENR medium was used for organoid culture.

Compound library (kind gift from Novartis) was composed of 2789 compounds (**Table 1**) in form of 1mM DMSO stocks in 384-well diamond-bottom plates. Every library plate contained 12 active controls (6 wells of gamma-secretase inhibitor DAPT and 6 wells of GSK3B inhibitor CHIR99021 (STEMCELL Technologies, cat # 72054) and 12 vehicle controls (DMSO). Compound treatment was performed from day 0 by adding 10µl of 25 µM intermediate compound library dilutions in WENRC medium using SELMA 384 automated pipettor (Analytik Jena AG) to achieve a final

concentration of 5 μ M. Second compound treatment was performed at day 3 using compound library dilutions in ENR, prepared as described above.

Experiments in fixed organoid samples

Organoids were collected 5-7 days after passaging and digested with TripLE (Invitrogen) for 20 min at 37 °C. Dissociated cells were passed through a cell strainer with a pore size of 20 μ m. For indicated experiments, single alive cells were sorted by FACS (Becton Dickinson FACSAria cell sorter). Forward scatter and side scatter properties were used to remove cell doublets and dead cells. Single cells derived from C57BL/6 wild type organoids unless indicated otherwise. Resuspended cells were mixed with Matrigel (Corning) in a medium to Matrigel ratio of 1:1, plated in 96-well plates (Greiner, cat.nr. 655090) in 3.5 μ l droplets and exposed to indicated compound treatments. All compound stocks were prepared in DMSO and DMSO was used as a vehicle control. Organoids were treated and fixed at indicated time points to generate samples for immunofluorescence imaging.

Organoid culture for RNA sequencing experiment

C57BL/6 wild type organoids were collected 5 days after passaging and digested with TripLE (Invitrogen) for 20 min at 37 °C. Experiment was performed in duplicate (technical replicates) for two independent biological samples (organoid cultures produced from two C57BL/6 male littermate mice). Dissociated cells were passed through a cell strainer with a pore size of 20 μ m. Single alive cells were sorted by FACS (Becton Dickinson FACSAria cell sorter). Forward scatter and side scatter properties were used to remove cell doublets and dead cells (**Figure S1**). Resuspended cells were mixed with Matrigel (Corning) in a medium to Matrigel ratio of 1:1 and plated in 24-well plates in 50 μ l droplets. From day 0 to day 3, WENRC medium (ENR was supplemented with 20% Wnt3a-conditioned medium, 10 μ M Y-27632 (ROCK inhibitor, STEMCELL Technologies) and 3 μ M of CHIR99021 (GSK3B inhibitor, STEMCELL Technologies, cat # 72054)) was used for organoid culture. At day 3, organoids were exposed to indicated compound

treatments concomitant with switch to ENR medium. Organoids were lysed at indicated time points and used for RNA extraction and sequencing as described below.

Culture of organoids in vitamin A-free medium

In indicated experiments, organoids were cultured in medium with or without vitamin A. To prepare the medium, B-27 minus vitamin A (Thermo Scientific) was used instead of 1×B27 (Thermo Scientific) to prepare both the ENR and WENRC medium. To allow for proper comparison, in these experiments, B-27 minus vitamin A (Thermo Scientific) was supplemented with retinyl acetate (Merck, cat.nr. 46958) corresponding to the standard B27 supplement in order to produce medium for the control conditions.

Organoid line generation using lentiviral constructs:

For RARE-GFP organoids, C57BL/6 wild type organoids were infected with in-house produced pGreenFire1-RARE viral particles (System Biosciences, Cat. Nr. TR037PA-1) or as control with pEGIP (Addgene plasmid #26777) at 0 hours. In brief, lentiviral particles were produced in HEK293T cells using a 2nd generation lentiviral system (pMDG.2 (Addgene plasmid #12259), psPAX2 (Addgene plasmid #12260) and the lentiviral genome), supernatant from producing cells was concentrated using Amicon Ultra-15, 100 kDa centrifugation columns (Merck Millipore, Cat.Nr. UFC910024) and used for lentiviral infection. Generated organoids were passaged once before selecting with 1µg/ml Puromycin over the course of 2 passages. After selection, organoid culture was performed as described above.

Fixed sample preparation and imaging

To allow imaging of all organoids within a similar z-range, each well plate was centrifuged at 3000 rpm for 10 min in a pre-cooled centrifuge at 10 °C prior to fixation. Organoids were fixed at indicated time points in 4% PFA (Electron Microscopy Sciences) in PBS for 45 min at room temperature.

For the image-based screening assay, organoids were permeabilized with 0.5% Triton X-100 (Sigma-Aldrich) for 1 h and blocked with 3% Fetal Calf Serum (Sigma-Aldrich) in PBS with 0.1% Triton X-100 for 1 h. Primary and secondary antibodies were diluted in blocking buffer and applied as described in **Supplementary Table 3**. Primary and secondary antibodies were diluted in blocking buffer and applied as indicated. Cell nuclei were stained with 0.2 $\mu\text{g}/\text{ml}$ DAPI (4',6-Diamidino-2-Phenylindole, Invitrogen) in PBS for 15 min. Cells were stained with 1 $\text{ng}/\mu\text{l}$ of Alexa Fluor® 647 carboxylic acid succinimidyl ester (CellTrace, Invitrogen) in carbonate buffer (1.95 ml of 0.5 M NaHCO_3 , 50 μl of 0.5 M Na_2CO_3 , both from Sigma-Aldrich, in 8 ml of water for 10 ml of buffer). For the image-based screening assay, all liquid handling steps were performed using EL406 Combination Washer Dispenser (BioTek Instruments).

For time course and compound treatment experiments, organoids were permeabilized with 0.5% Triton X-100 (Sigma-Aldrich) for 1 h and blocked with 3% Donkey Serum (Sigma-Aldrich) in PBS with 0.1% Triton X-100 for 1 h. Primary and secondary antibodies were diluted in blocking buffer and applied at dilutions indicated in the **Supplementary Table 3**. Cell nuclei were stained with 0.2 $\mu\text{g}/\text{ml}$ DAPI (4',6-Diamidino-2-Phenylindole, Invitrogen) in PBS for 15 min.

In all samples, high-throughput imaging was done with an automated spinning disk microscope from Yokogawa (CellVoyager 7000S), with an enhanced CSU-W1 spinning disk (Microlens-enhanced dual Nipkow disk confocal scanner), a 40x (NA = 0.95) Olympus objective, and a Neo sCMOS camera (Andor, 2560 \times 2160 pixels). For imaging, an intelligent imaging approach was used (Search First module of Wako Software Suite). For this, in each well one field was acquired with 2x resolution in order to cover the complete well. This overview was then used to segment individual organoids on the fly with a custom written ImageJ macro which outputs coordinates of individual organoid positions. These coordinates were used to generate map of locations for high resolution re-imaging (40x, NA = 0.95). For each site, z-planes spanning a range up to 60 μm were acquired. 5 μm z-step was used in all experiments unless indicated otherwise.

Primary antibody labeling

Anti-Lysozyme antibody (EC3.2.1.17, Dako) was labeled with CF568 fluorophore using a labeling kit Mix-N-Stain (Biotium) according to manufacturer's instructions.

Compound treatment of intestinal organoids

In indicated experiments, following compounds were used:

Modality	Compound	Supplier
ALDH1A1 inhibitor	A37	Tocris (Cat. Nr. 5802)
RXRA agonist	NRX 194204	Axon Med Chem (Cat. Nr. 2408)
RARA agonist	All-trans retinoic acid	Sigma (Cat. Nr. R2625)
RXRA/RARA agonist	9-cis retinoic acid	Sigma (Cat. Nr. R4643)
RXR antagonist	Cpd2170	Novartis

Histology procedures and beta-Galactosidase staining

Ca. 7 mm longitudinal segments of the small intestine isolated from RARE-LacZ mice were fixed in 2% PFA+1% glutaraldehyde in PBS and used for enzymatic staining. Beta-Galactosidase staining was performed using beta-Galactosidase Reporter Gene Staining Kit (Merck Millipore) according to supplier instructions, samples were incubated in staining solution overnight. Stained samples were embedded in paraffin and used to make 8µm lateral sections. Sections were mounted on glass slides and used for imaging with Axioscan Z1 slide scanner (Zeiss) at 40x resolution.

Image analysis and organoid feature extraction

Organoid segmentation in MIPs. For each acquired confocal z-stack field, maximum intensity projections (MIP) and sum intensity projections (SIP) were generated from all acquired z planes per field. All MIP fields belonging to the same well were stitched together to obtain MIP well overviews for each channel. The high resolution well overviews were used for organoid segmentation and feature extraction. Each individual organoid was automatically segmented

based on either CellTrace (image-based screening assay) or DAPI signal (all other imaging assays). To allow precise segmentation, clumped objects were separated using edge information (Canny edge detection algorithm) and subsequent watershedding with imposed minima.

Features MIP. For each segmented organoid, a total of 34 features describing shape and intensities for each acquired channel were extracted. Further 60 features describing the Zernike polynomials were extracted and used for object filtering as described below. MIPs were used to describe fluorescence distribution and the morphological features of organoids. A subset of features was selected for multivariate feature analysis based on the information content and covariance as described below.

Features SIP. SIPs were used to extract features relating to total intensity per object to allow accurate quantification. In the image-based screen, SIP projections were used to extract all features for the segmented objects.

Feature selection for the quantitative image analysis

Extracted features were analyzed for covariance to exclude highly (anti-) correlated features. Generated covariance matrix was clustered using fuzzy c-means clustering to generate 10 covariance clusters. To exclude features with low information content, we analyzed the principle component loading of first 10 principle components (defined as absolute value of the feature eigenvector multiplied with the eigenvalue of the feature). We have selected a set of 9 features to use for unsupervised clustering with PhenoGraph (<https://omictools.com/phenograph-tool>) (**Extended Data Fig. 1**).

To validate the selected set of features, we performed backwards feature elimination using a naïve Bayesian predictor. In brief, we used the assignments of the PhenoGraph classification generated based on the 9-feature array defined above as the ground truth, 66% of the entire dataset were used to generate a prediction model and remaining data was used for testing the prediction. Initial feature list (34 extracted features) was reduced by one feature per iteration and the prediction accuracy was assessed. Resulting list of nine features contained 6 out of 9 features initially used for the PhenoGraph clustering (**Extended Data Fig. 1**).

Feature normalization

In all imaging experiments, extracted features were normalized using z-score normalization within respective assay plates.

SVM detection of segmentation artifacts

A linear SVM was trained on a dataset 100 randomly picked individual organoids with correct segmentation and 100 organoids with observed segmentation artifacts. Features used for SVM prediction consisted of the 9 features used for PhenoGraph analysis and also included 60 Zernike polynomials.

Filtering of sparse conditions

For the image-based screening assay, conditions with less than 10 organoids detected per well were discarded from the analysis. In other assays the threshold level for sparse conditions was assessed on an assay-to assay basis, generally all conditions with less than 20% of the mean organoid count in the given assay were discarded.

Generation of phenotypic signatures

Phenotypic clustering was done on the entire dataset (402930 organoids) using the feature set defined in **Extended Data Fig. 1** utilizing the software package PhenoGraph (Matlab implementation, <https://github.com/dpeerlab/cyt3>) as described above. Abundance of every phenotypic class was calculated as a fraction of organoids belonging to the class in every individual condition. Abundance was z-score transformed within assay plates to minimize plate effects. Resulting 15-element arrays were used as phenotypic fingerprints for subsequent steps of the analysis.

Hit selection

Individual treatment conditions were ranked by reproducibility between replicates defined as the correlation coefficient for 15-element phenotypic fingerprints of respective conditions. Conditions with a reproducibility score above 0.5 and a z-score value of phenotypic class abundance of above 1.5 or below -1.5 for any of the classes were included in the hit list. Conditions where a z-score value of phenotypic class abundance of above 4 or below -4 for any of the classes was detected were also included in the hit list regardless of the reproducibility score.

Selection of a representative condition per target gene

For the conditions that met the criteria of hit selection, annotated target genes were used. The condition with the best combined score (maximum variance in any of the 15 phenotypic classes normalized by reproducibility score) was used to determine the representative condition per gene.

Target gene enrichment score

To ensure that the hit list was not prone to contain genes targeted by a high number of compounds in the initial library, we calculated a Target gene enrichment score (S_{enr}) as formulated below:

$$S_{enr} = \frac{n(hitlist)^2}{n(library)}$$

Whereby $n(hitlist)$ is the number of compounds with the same modality in the hit list that target a given gene and $n(library)$ is the number of compounds with the same modality that target a given gene in the initial library. S_{enr} was then used to filter out conditions overrepresented in the initial compound library.

Hierarchical interaction score calculation

Hierarchical interaction score was calculated as described in literature² using the 15-element phenotypic fingerprints as input. Resulting interaction matrix was used to infer edges for

generating a network of phenotypic interactions. For further analysis, only genes connected by edges with HIS>0.2 were kept, resulting in a network of 124 genes. Subnetworks were identified using the Cytoscape implementation of the ClusterOne algorithm³. For visualization purposes, only edges with the highest HIS value per node were kept.

STRING validation of the HIS predictive power

According to graph theory, in an undirected simple graph of order n , the maximum degree of each vertex is $n - 1$ and the maximum size of the graph G is

$$G = \frac{n(n - 1)}{2}$$

For protein-protein interaction networks however a modified version of the equation is widely used where each possible edge in the graph on nodes is present with probability p :

$$G = \frac{p(n(n - 1))}{2}$$

For the STRING interaction network generated for the 230 genes that make up the list of hits identified in the screen, the factor p equals 0.04. We used this factor for the prediction model, calculating the predicted number of edges for a set of genes that are retained when a sliding HIS threshold was applied (**Extended Data Fig. 4b**).

Annotation enrichment analysis

Annotation enrichment analysis was performed using ClueGo plugin for Cytoscape⁴. Enrichment of KEGG functional annotations (Homo Sapiens and Mus Musculus KEGG pathways, version of 01.03.2017) was calculated against corresponding background (all detected genes for RNA sequencing experiments and list of unique targets of the compound library (**Supplementary Table 1**) for the image-based screen).

Annotation enrichment analysis in HIS network

For annotation enrichment analysis in the network of HIS interactions (**Fig. 2**), minimal number of genes was adjusted according to subnetwork size in the range from 2 to 4 genes.

Annotation enrichment analysis in compound RNA sequencing dataset

For annotation enrichment analysis in the RNA sequencing dataset (**Figure 4**), minimal number of genes of 3 was used and only annotations with enrichment p-value below 0.05 were included.

Time-course WT Bulk RNA purification

RNA was isolated using Single Cell RNA Purification Kit (Norgen Biotek Corporation, Cat #51800) pooling 3 wells of 24 well plates (C57BL/6 wild type). Organoids were seeded as single cells at 50000 cells per well and cultured as described above. RNA purification was performed in duplicate for two organoid cultures (C57BL/6 wild type, male littermate mice) for all treatment conditions. A step of DNase treatment was included (RNase-Free DNase I Kit, Cat #25710) for all samples.

RNA sequencing and raw data processing

RNA sequencing libraries were prepared using the TruSeq Illumina mRNA Library Prep and sequenced with the Illumina HiSeq2500 platform. Reads were mapped to the UCSC mouse genome mm10 using STAR (version 2.5.2b⁵) using parameters `--outFilterType BySJout --outFilterMultimapNmax 20 --outMultimapperOrder Random --alignSJoverhangMin 8 --alignSJDBoverhangMin 1 --outFilterMismatchNmax 999 --alignIntronMin 20 --alignIntronMax 1000000 --alignMatesGapMax 1000000 --outSAMmultNmax 1`.

Genes expression level were quantified with the QuasR Bioconductor package⁶, using gene annotations from the TxDb.Mmusculus.UCSC.mm10.knownGene Bioconductor package. $\log_2(\text{CountsPerMillion})$ ($\log_2(\text{cpm})$) of uniquely mapped reads were used to describe similarities and differences among the samples.

Differentially expressed genes were determined with the package edgeR (version 3.20.5⁷) by fitting a three-factor model (timepoint + mouse + treatment condition) to the counts of genes that were detected in 2 or more samples with at least one read per million reads. To identify significantly differentially regulated genes, we selected genes with $\log_2\text{FC} < -1$ or > 1 , and $\text{FDR} < 0.1$ for any condition compared to mean of all conditions selecting 1884 out of detected 12065 genes.

Transcription factor binding motif analysis

Transcription Factor Binding Site Analysis was done using HOMER (version 4.8, <http://homer.ucsd.edu/homer/motif/>) similarly as described⁸ Briefly, promoter regions were defined as a windows of 500 bp centered on the transcript start site, only retaining a single region per gene. Transcription factor binding sites (TFBS) for 579 vertebrate motifs from the JASPAR2018 Bioconductor package (version 1.1.1) were predicted by converting the positional frequency matrices to log2-odds matrices (using a pseudocount of 1.0 per position and base and a uniform base frequencies as background), and then scanning the promoter regions with a cut-off score of 90% of the maximal motif score. For each timepoint of organoid development (day 0 to day 7), genes were binned into groups of 400 according to the log2 fold-change of expression at that timepoint compared to the average of all timepoints, keeping genes with absolute log2 fold-changes <1 in a single (non-changed) bin. Enriched motifs in each bin were then identified using findMotifsGenome.pl from HOMER with all other bins as background and parameters -nomotif -size 500. Enrichment scores were calculated as $enr = (obs - exp) / (exp^{0.5})$, where *obs* and *exp* are the observed and expected counts of motif hits in a bin, respectively. The raw P values in the HOMER output for all motifs and bins were adjusted for multiple-testing by calculating false discovery rates (FDR) using the R function p.adjust. For combined visualization of motif enrichments over the whole timecourse (Extended Data Fig. 7b), the enrichment scores and FDR values in the bin with the top up-regulated genes were extracted from each timepoint and combined into a single heatmap.

Correlation with published datasets

For the helminthes infection RNA sequencing data set, raw data was obtained from the GEO repository, GEO accession numbers are indicated in the below. Data was processed from read counts as described above.

GEO accession numbers of external RNA sequencing datasets used in the study

GEO accession number	Description	Reference
GSE97405	Helminthes infection in mouse intestine	⁹
GSE115955	Time course of organoid development	¹⁰

To identify tissue-specific genes we selected all genes from the GTEx repository (<https://gtexportal.org/>), mapping the human genes to their respective mouse orthologues. We then analyzed the tissue type specificity of genes that showed variance in the compound treatment RNA sequencing dataset, selecting genes present in both datasets. Tissue type specificity was assigned as the tissue type with the highest expression level for genes that had at least two-fold expression level of that of the small intestine ($\log_2FC > 1$, $FDR < 0.1$). Genes specific for the intestine were determined as genes with at least four-fold expression ($\log_2FC > 2$, $FDR < 0.1$) in the intestine compared to other GI tract tissues.

Intestinal stem cell specific signature was taken from a published single cell RNA sequencing dataset¹¹.

Transcriptional changes observed in intestine regenerative response¹² were used to select signature genes defining the regenerative response signature.

Irradiation-induced injury model and RXRi dosing regimen

8-week old male C57BL/6J mice (Jackson labs) were weighed and divided into groups on day 0. Mice were exposed to irradiation with 20Gy gamma dose. A lead shielding device restricted the irradiation dose to a 2cm opening along the ventral surface of the mice, and limited exposure to

extremities. In order to immobilize mice during the procedure all mice (except non-irradiated RXR antagonist (Cpd2170)-dosed) were injected with 7mL/kg anesthetic I.P containing 10% ketamine and 1% xylazine in 0.9% sodium chloride (Henry Schein).

On day 1, 2, and 3 only both non-irradiated or irradiated mice were dosed with either 0.5% methylcellulose + 0.1% tween-80 (Sigma) or 30mg/kg Cpd2170 (RXRi) at 5mL/kg twice a day (7h apart) through oral administration.

Hemocult testing was performed before necropsy (day 5 or 6) using the Beckman Coulter Sensa kit. Stool samples were applied to test paper using spatula and smeared, allowed to dry for ca. 5min. 1-2 drops of developer solution was added to each sample, and the result interpreted within 1 minute. A blue coloration indicated blood in the stool. 1-2 drops of tail blood were used as positive control.

Tissue harvest and histology

Mice were euthanized using CO₂ asphyxiation and cervical dislocation. The small intestines were collected and cleaned using cold HBSS (Hyclone) and fixed in a Swiss roll conformation with 10% neutral buffered formalin in PBS (Avantik) for 48hr at room temperature before transfer into 70% ethanol. Small intestine Swiss rolls were embedded in paraffin (Sakura Tissue Tek) and 5 micron longitudinal serial sections were cut using a Leica RM2255. Swiss rolls were stained for Haematoxylin and Eosin, Alcian blue, and Ki67 (Thermo, RM-9106-S, 1:100 dilution) via histochemistry (Ventana discovery ultra). Slides were scanned, and analyzed using the Nanozoomer S360.

Code Availability:

Code used for image analysis in this study was developed in the Liberali lab in Matlab and Python 3. Segmentation for the image-based screen was performed using code developed in Liberali laboratory in Matlab. The code for organoid 2D segmentation and feature extraction in other assays is available under <https://github.com/fmi-basel/glib-nature2018-materials>.

Data availability:

RNA-seq data is available at the Gene Expression Omnibus repository under the accession number GSE134755.

References

- 1 Sato, T. *et al.* Single Lgr5 stem cells build crypt-villus structures in vitro without a mesenchymal niche. *Nature* **459**, 262-265, doi:10.1038/nature07935 (2009).
- 2 Snijder, B., Liberali, P., Frechin, M., Stoeger, T. & Pelkmans, L. Predicting functional gene interactions with the hierarchical interaction score. *Nat Methods* **10**, 1089-1092, doi:10.1038/nmeth.2655 (2013).
- 3 Nepusz, T., Yu, H. & Paccanaro, A. Detecting overlapping protein complexes in protein-protein interaction networks. *Nat Methods* **9**, 471-472, doi:10.1038/nmeth.1938 (2012).
- 4 Bindea, G. *et al.* ClueGO: a Cytoscape plug-in to decipher functionally grouped gene ontology and pathway annotation networks. *Bioinformatics* **25**, 1091-1093, doi:10.1093/bioinformatics/btp101 (2009).
- 5 Dobin, A. *et al.* STAR: ultrafast universal RNA-seq aligner. *Bioinformatics* **29**, 15-21, doi:10.1093/bioinformatics/bts635 (2013).
- 6 Chevrier, S. *et al.* An Immune Atlas of Clear Cell Renal Cell Carcinoma. *Cell* **169**, 736-749 e718, doi:10.1016/j.cell.2017.04.016 (2017).
- 7 McCarthy, D. J., Chen, Y. & Smyth, G. K. Differential expression analysis of multifactor RNA-Seq experiments with respect to biological variation. *Nucleic Acids Res* **40**, 4288-4297, doi:10.1093/nar/gks042 (2012).
- 8 Barisic, D., Stadler, M. B., Iurlaro, M. & Schubeler, D. Mammalian ISWI and SWI/SNF selectively mediate binding of distinct transcription factors. *Nature* **569**, 136-140, doi:10.1038/s41586-019-1115-5 (2019).
- 9 Nusse, Y. M. *et al.* Parasitic helminths induce fetal-like reversion in the intestinal stem cell niche. *Nature* **559**, 109-113, doi:10.1038/s41586-018-0257-1 (2018).
- 10 Serra, D. *et al.* Self-organization and symmetry breaking in intestinal organoid development. *Nature* **569**, 66-72, doi:10.1038/s41586-019-1146-y (2019).
- 11 Haber, A. L. *et al.* A single-cell survey of the small intestinal epithelium. *Nature* **551**, 333-339, doi:10.1038/nature24489 (2017).
- 12 Gregorieff, A., Liu, Y., Inanlou, M. R., Khomchuk, Y. & Wrana, J. L. Yap-dependent reprogramming of Lgr5+ stem cells drives intestinal regeneration and cancer. *Nature*, 1-16, doi:10.1038/nature15382 (2015).

Supplementary Table 1: antibody stocks, dilutions and incubation times used for immunofluorescence staining in this study

Target	Host	Dilution	Duration	Provider
Anti-AldolaseB	Rabbit	1:400	1h at room temp.	Abcam (ab75751)
Anti-ALDH1A1	Rabbit	1:200	1h at room temp.	Abcam (ab52492)
Anti-Yap1	Rabbit	1:100	Overnight at 4 °C	CST (#14074)
Anti-Yap1 AF 488 conjugate	Rabbit	1:100	Overnight at 4 °C	CST (#)
Anti-Yap1 AF 647 conjugate	Rabbit	1:100	Overnight at 4 °C	CST (#38707)
Anti-Lysozyme (EC3.2.1.17)	Rabbit	1:400	1h at room temp.	DAKO (A0099)
Anti-Lysozyme CF568 conjugate	Rabbit	1:400	1h at room temp.	Produced in-house
Anti-Dll1	Sheep	1:100	Overnight at 4 °C	R&D Systems (AF3970)
Anti-Ki67	Rabbit	1:200	1h at room temp.	CST (#11988)
Anti-Ki67	Rabbit	1:100	1h at room temp.	Thermo (RM-9106-S)
Alexa Fluor 488 donkey anti rabbit IgG	Donkey	1:500	1h at room temp.	Abcam (ab5450)
Alexa Fluor 568 donkey anti rabbit IgG	Donkey	1:500	1h at room temp.	CST (#2586)
Alexa Fluor 488 donkey anti mouse IgG	Donkey	1:500	1h at room temp.	Abcam (ab111125)
Alexa Fluor 568 donkey anti mouse IgG	Donkey	1:500	1h at room temp.	CST (#39141)
Alexa Fluor 488 donkey anti sheep IgG	Donkey	1:500	1h at room temp.	Abcam (ab16667)
Alexa Fluor 568 donkey anti sheep IgG	Donkey	1:500	1h at room temp.	Thermo Fisher Scientific (A-21206)
Alexa Fluor 647 donkey anti sheep IgG	Donkey	1:500	1h at room temp.	Thermo Fisher Scientific (A10042)

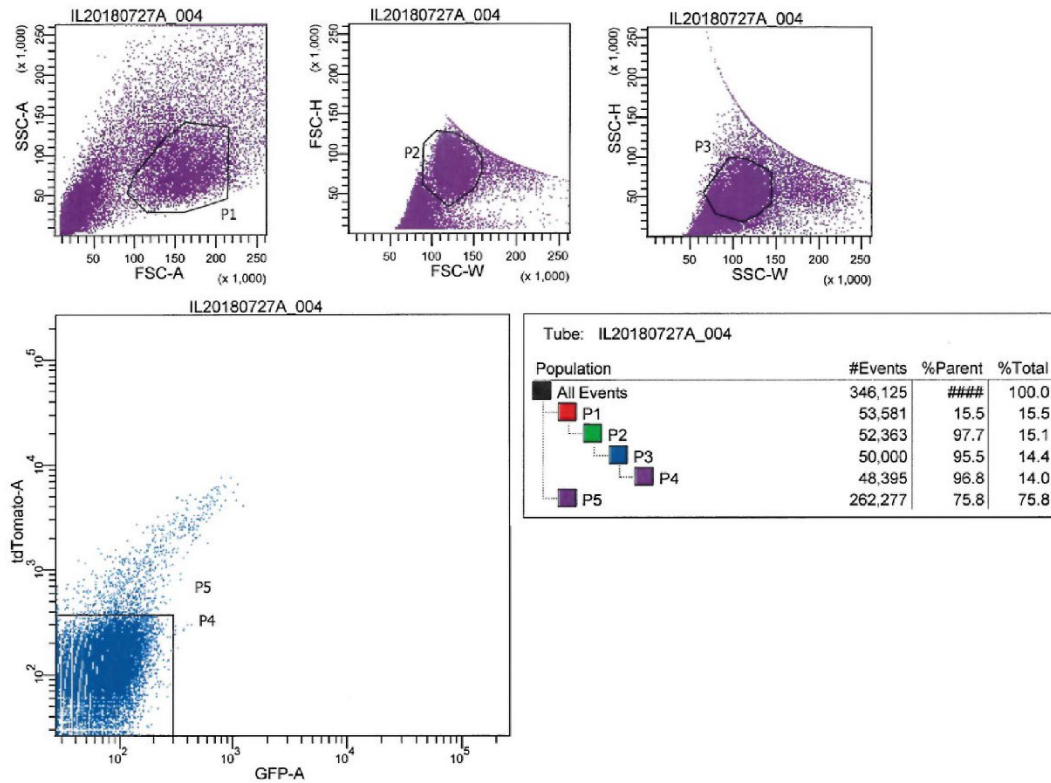


Figure S1: Gating strategy for flow cytometry to remove debris, dead cells and cell doublets

Scatter plots showing the selection in SSC-A/FSC-A gating (P1), FSC-H/FSC-W gating (P2) and SSC-H/SSC-W gating (P3) and additional gating used for fluorescence (P4). Percentage of parent cells in respective gates (bottom right).